Spinel Ferrite Nanoparticles – Solvent Restructuring and Crystal Structure depending on Elemental Composition and Synthesis Route

Dissertation

zur Erlangung des akademischen Grades eines Doktors
der Naturwissenschaften (Dr. rer. nat.)

an der Fakultät für Biologie, Chemie und Geowissenschaften
der Universität Bayreuth

vorgelegt von

Mirco Eckardt

geboren in Münchberg

Bayreuth, 2023

Die vorliegende Arbeit wurde in der Zeit von Juli 2017 bis August 2023 in Bayreuth am Lehrstuhl Anorganische Chemie I – Mesostrukturierte Materialien unter Betreuung von Frau Professorin Dr. Mirijam Zobel angefertigt.

Vollständiger Abdruck der von der Fakultät für Biologie, Chemie und Geowissenschaften der Universität Bayreuth genehmigten Dissertation zur Erlangung des akademischen Grades eines Doktors der Naturwissenschaften (Dr. rer. nat.).

Form der Dissertation:	Monographie
Dissertation eingereicht am:	20.09.2023
Zulassung durch Promotionskommission:	27.09.2023
Wissenschaftliches Kolloquium:	25.07.2024

Amtierender Dekan: Prof. Dr. Cyrus Samimi

Prüfungsausschuss:

Prof. Dr. Mirijam Zobel	(Gutachterin)
Prof. Dr. Josef Breu	(Gutachter)
Prof. Dr. Markus Retsch	(Vorsitz)
Prof. Dr. Seema Agarwal	

Die vorliegende Arbeit ist als Monographie verfasst.

Teile der Arbeit sind bereits in den folgenden Publikationen erschienen:

Long-Term Colloidally Stable Aqueous Dispersions of ≤5 nm Spinel Ferrite Nanoparticles
M. Eckardt, S. L. J. Thomä, M. Dulle, G. Hörner, B. Weber, S. Förster, M. Zobel, *ChemistryOpen* **2020**, *9*, 1214-1220
DOI: 10.1002/open.202000313
Diese Publikation ist in der vorliegenden Arbeit mit der Literaturstelle [7] zitiert.

Magnetic properties and structural analysis on spinel MnFe2O4 nanoparticles prepared via non-aqueous microwave synthesis
C. Simon, A. Blösser, M. Eckardt, H. Kurz, B. Weber, M. Zobel, R. Marschall, *Z. Anorg. Allg. Chem.* **2021**, *647*, 2061-2072
DOI: 10.1002/zaac.202100190
Diese Publikation ist in der vorliegenden Arbeit mit der Literaturstelle [129] zitiert.

“If more of us valued food and cheer and song above hoarded gold, it would be a merrier world.”

J.R.R. Tolkien (1892 - 1973) in *The Hobbit*

Content

Summary

The interaction of small nanoparticles (< 10 nm) with their surrounding medium, such as water, mainly determines their functionality and efficiency in applications such as catalysis or medicine. This interaction depends on material properties like atomic composition, crystal structure, and surface functionalization. However, despite the common usage of nanoparticles, the exact impact of each of these parameters is still largely unknown and requires further investigation. The aim of this thesis is to systematically analyze the crystal structure, surface functionalization, and hydration shell structure, with respect to atomic composition, nature of organic surface stabilizers, synthesis route and nanoparticle shape of spinel ferrite nanoparticles (MFe_2O_4; M = divalent metal cation).

Highly colloidally stable and crystalline spinel ferrite nanoparticles with the general formula MFe_2O_4 (M = Co^{2+}, Mg^{2+}, Ni^{2+}, or Zn^{2+}) and mean diameters of 3 – 5 nm were synthesized using an optimized, simple, and reproducible polyol method in diethylene glycol (DEG). The synthesized spinel ferrite nanoparticles were post-synthetically surface modified with biocompatible molecules such as citrate, betaine, and phosphocholine to ensure their stability. The particle size and particle size distribution were determined using small-angle X-ray scattering (SAXS), transmission electron microscopy (TEM) and dynamic light scattering (DLS). Different shapes of spinel ferrite nanoparticles were realized by the syntheses of cubic and rod-shaped $CoFe_2O_4$ nanoparticles.

The elemental composition of the spherical spinel ferrite nanoparticles was determined by inductively coupled plasma optical emission spectrometry (ICP-OES), confirming a Fe^{3+} to M^{2+} ratio of 2 to 1, except for $ZnFe_2O_4$ nanoparticles, which had a Fe^{3+} to Zn^{2+} ratio of 3 to 1. Crystal structure analysis using pair distribution function (PDF) and X-ray diffraction (XRD) confirmed a monocrystalline structure of the synthesized nanoparticles. The finite size of the spinel ferrite nanoparticles resulted in disorder and vacancies on the octahedral coordinated metal positions in the cubic *Fd-3m* crystal structure. Magnetism analysis of the different spinel ferrite nanoparticles using superconducting quantum interference device (SQUID) measurements revealed superparamagnetic behavior and a dependence of saturation magnetization (M_S) on the incorporated metal ion. For related iron oxide nanoparticles (IONP) synthesized in DEG by Ms. Sabrina Thomä (University of Bayreuth),

the PDF structure analysis revealed difficulty in distinguishing between a tetragonal or cubic space group due to the high disorder of the small nanoparticles. However, the model based on the cubic *Fd-3m* space group best described both spinel ferrite and iron oxide nanoparticles. In contrast, $MnFe_2O_4$ nanoparticles synthesized via a microwave assisted synthesis route by the group of Prof. Marschall (University of Bayreuth) and Co_2FeO_4 nanoparticles synthesized via co-precipitation by the group of Prof. Behrens (formerly at the University of Duisburg-Essen, now at the Christian-Albrechts-Universität zu Kiel) deviated from the crystal structure of the spinel ferrite nanoparticles synthesized in DEG. Both $MnFe_2O_4$ and Co_2FeO_4 nanoparticles underwent temperature-dependent phase transitions between 400 and 900 °C. The spinel structure of $MnFe_2O_4$ nanoparticles converted to α-Mn_2O_3 and α-Fe_2O_3, while Co_2FeO_4 nanoparticles only emerged at calcination temperatures higher than 900 °C. At lower temperatures, the crystal structure was divided in a cobalt-rich Co_3O_4 and an iron-rich $CoFe_2O_4$ phase.

Furthermore, the surface of the spinel ferrite nanoparticles synthesized in DEG was investigated. Due to the surface modification uncovering of the surface chemistry proved to be challenging. By the combination of thermogravimetric analysis (TGA) and elemental analysis (CHN), it was possible to reveal the surface chemistry of the spinel ferrite nanoparticles. Fourier transform infrared (FT-IR) analysis was used to analyze the coordination geometry of the stabilizer molecules on the nanoparticle surface. The surface modification ensured the long-term colloidal stability of aqueous dispersions of the spinel ferrite nanoparticles up to concentrations of 100 g L^{-1} for three months.

In general, this thesis demonstrates that the structure of spinel ferrite nanoparticles can be very similar with different atomic compositions (e.g., $CoFe_2O_4$ and $NiFe_2O_4$) or it can vary in terms of particle size and structure (e.g., $MgFe_2O_4$ and $ZnFe_2O_4$). The synthesis route also significantly influences the final structure of the nanoparticles. Additionally, it proves the capability and versatility of the PDF analysis, enabling the investigation of the short and middle-range order of spinel ferrite nanoparticles. It is shown that the combination of FT-IR, TGA and CHN is a powerful approach for characterizing the surface composition of inorganic nanoparticles. By double-difference PDF (dd-PDF) analysis of spinel ferrite nanoparticles in aqueous dispersions different bonding dintances are extracted for different atomic compositions. Restructured water molecules at the

nanopartilce-water interface possibly contribute to these signals. Thus, a thorough study of the origin of the results of this dd-PDF analysis is requried in future.

These insights may lead to controlled developments of nanoparticlar catalysts, for example. They may be transferred to other types of nanoparticles, as well.

Zusammenfassung

Die Wechselwirkungen von kleinen Nanopartikeln (< 10 nm) mit dem umgebenden Medium, wie z.B. Wasser, bestimmt hauptsächlich die Funktionalität und Effektivität in den unterschiedlichen Anwendungsgebieten wie der Katalyse oder Medizin. Diese Wechselwirkungen sind abhängig von den Materialeigenschaften wie Elementzusammensetzung, Kristallstruktur und Oberflächenfunktionalisierung. Trotz der häufigen Verwendung von Nanopartikeln ist der genaue Einfluss dieser Parameter auf die Funktionalität kaum untersucht. Das Ziel dieser Dissertation ist daher, die systematische Analyse der Kristallstruktur, der Oberflächenfunktionalisierung und der Struktur der Wasserhülle in Abhängigkeit von der Elementzusammensetzung, der Art der Oberflächenmodifikatoren, der Syntheseroute und der Nanopartikelform von Spinellferritnanopartikeln (MFe_2O_4; M = zweiwertiges Metallkation).

Kolloidal sehr stabile und hochkristalline Spinellferritnanopartikel mit der Summenformel MFe_2O_4 (M = Co^{2+}, Mg^{2+}, Ni^{2+}, oder Zn^{2+}) und Durchmessern von 3 – 5 nm wurden mittels einer optimierten, einfachen und reproduzierbaren Polyolsynthese in Diethylenglykol (DEG) hergestellt. Die direkt nach der Synthese stattgefundene Oberflächenmodifizierung mit den umweltverträglichen Molekülen Citrat, Betain und Phosphocholin garantiert die Stabilität der Spinellferritnanopartikel. Die Größe und Größenverteilung der Nanopartikel wurden mittels SAXS, Transmissionselektronenmikroskopie (TEM) und dynamischer Lichtstreuung (DLS) bestimmt. Unterschiedliche Formen von Spinellferritnanopartikeln wurden durch die Synthese von stäbchenförmigen und kubischen $CoFe_2O_4$ Nanopartikeln realisiert. Die Größe dieser Nanopartikel wurde mittels TEM und SAXS bestimmt.

Die Analyse der Elementzusammensetzung der sphärischen Spinellferritnanopartikel erfolgte mittels optischer Emissionsspektrometrie mit induktiv gekoppeltem Plasma (ICP-OES). Diese Analyse bestätigte das Verhältnis von Fe^{3+} zu M^{2+} von 2 zu 1 mit Ausnahme der $ZnFe_2O_4$ Nanopartikel, die ein Verhältnis von Fe^{3+} zu Zn^{2+} von 3 zu 1 haben. Die Analyse der Kristallstruktur mit der Paarverteilungsfunktion (PDF) und der Röntgendiffraktion (XRD) bewies die Einkristallinität der sphärischen Spinellferritnanopartikel. Die Unordnung, die durch die begrenzte Größe der Nanopartikeln hervorgerufen wird, führt dazu, dass Leerstellen auf den

Oktaederpositionen im kubischen Kristallsystem *Fd-3m* entstehen. Magnetmessungen mit einem supraleitenden Quanteninterferenzgerät (SQUID) zeigten das superparamagnetische Verhalten der Spinellferritnanopartikel. Die Sättigungsmagnetisierung (M_S) ist dabei abhängig von der Art des zweiwertigen Kations. Der Transfer dieser Erkenntnisse auf die PDF Analyse von 3 – 5 nm großen Eisenoxidnanopartikeln (IONP) hergestellt von Fr. Sabrina Thomä (Universität Bayreuth) zeigte, dass eine klare Unterscheidung zwischen einer kubischen und tetragonalen Raumgruppe bei kleinen Nanopartikeln nur schwer möglich ist. Letztendlich ergab die Strukturanalyse, dass für die IONP wie auch für die Spinellferritnanopartikel das Modell, welches auf der kubischen *Fd-3m* Raumgruppe basierte, am besten passte. Im Kontrast dazu weicht die Kristallstruktur von $MnFe_2O_4$ Nanopartikeln, die über eine Mikrowellensynthese von der Arbeitsgruppe um Prof. Marschall (Universität Bayreuth) hergestellt wurden, und von Co_2FeO_4 Nanopartikeln, die über eine Ausfällungsreaktion von der Arbeitsgruppe um Prof. Behrens (früher: Universität Duisburg-Essen; jetzt: Christian-Albrechts-Universität zu Kiel) hergestellt wurden, von den Spinellferritnanopartikeln, die in DEG synthetisiert wurden, ab. Beide, $MnFe_2O_4$ und Co_2FeO_4 Nanopartikel erfahren eine temperaturabhängige Phasenumwandlung in einem Temperaturbereich von 400 – 900 °C. Zwischen 400 und 600 °C wandelt sich die Spinellstruktur der $MnFe_2O_4$ Nanopartikel in α-Mn_2O_3 und α-Fe_2O_3 um. Reine Co_2FeO_4 Nanopartikel hingegen entstehen erst bei Kalzinierungstemperaturen oberhalb von 900 °C. Bei niedrigeren Temperaturen liegt ein Phasengemisch von kobalthaltigem Co_3O_4 und eisenhaltigem $CoFe_2O_4$ vor.

Außerdem wurde die Oberfläche der sphärischen Spinellferritnanopartikel, die in DEG synthetisiert wurden, näher untersucht. Durch die Oberflächenmodifizierung ist die Analyse der Oberflächenzusammensetzung herausfordernd, da viele organische Molekülspezies nebeneinander existieren können. Durch eine Kombination aus thermogravimetrischer Analyse (TGA) und Elementaranalyse (CHN) war es möglich, diese Oberflächenzusammensetzung der Spinellferritnanopartikel aufzudecken. Mithilfe von Fourier-transformierten Infrarotspektroskopiemessungen (FT-IR) war es außerdem möglich, die Koordinationsgeometrie der Stabilisatormoleküle an der Nanopartikeloberfläche zu untersuchen. Diese Oberflächenmodifikation garantiert die

Langzeitstabilität kolloidaler Dispersionen selbst bei hohen Konzentrationen bis zu 100 g L^{-1} für mindestens drei Monate.

Im Allgemeinen zeigt diese Arbeit, dass die Struktur von Spinellferritnanopartikeln bei unterschiedlichen atomaren Zusammensetzungen sehr ähnlich sein kann (z.B. $CoFe_2O_4$ and $NiFe_2O_4$) oder sich hinsichtlich Partikelgröße und Struktur unterscheidet (e.g., $MgFe_2O_4$ and $ZnFe_2O_4$). Auch die Syntheseroute beeinflusst die endgültige Struktur der Nanopartikel signifikant. Darüber hinaus belegt sie die Fähigkeit und Vielseitigkeit der PDF-Analyse, die die Untersuchung der kurz- und mittelreichweitigen Ordnung von Spinellferritnanopartikeln ermöglicht. Ferner wird gezeigt, dass die Kombination von FT-IR, TGA und CHN ein leistungsfähiger Ansatz zur Charakterisierung der Oberflächenzusammensetzung anorganischer Nanopartikel ist. Durch die Analyse von Spinellferritnanopartikeln in wässrigen Dispersionen mittels doppelter Differenz-PDF (dd-PDF)-Analyse werden unterschiedliche Bindungsabstände für verschiedene atomare Zusammensetzungen ermittelt. Restrukturierte Wassermoleküle an der Grenzfläche zwischen Nanopartikeln und Wasser könnten möglicherweise zu diesen Signalen beitragen. Daher ist in Zukunft eine gründliche Untersuchung der Herkunft der Ergebnisse dieser dd-PDF-Analyse erforderlich.

Übertragen auf weitere Nanopartikelsysteme können diese Erkenntnisse in Zukunft zur kontrollierten Synthese von einer Vielzahl von exakt angepassten Nanopartikel-Katalysatoren führen, da durch geringe Änderungen der Synthese bzw. der Zusammensetzung die Oberflächeneigenschaften eingestellt werden können.

1 Motivation

Spinel-type ferrite nanoparticles with the chemical formula MFe_2O_4, where M is a divalent metallic cation such as Co^{2+}, Mg^{2+}, Ni^{2+}, or Zn^{2+} are in particular promising for applications ranging from biomedicine,[8-10] ferrofluids[11-12] to photocatalytic applications like the degradation of environmental pollutants or water splitting[13-15] and heterogeneous catalysis.[16-18] This interest arises due to their unique properties like finite size and surface effects, their high saturation magnetization as well as their superparamagnetism.[19] Particularly, the adjustability of these properties by readily changing the metal ion composition or the occupancy of the tetrahedral and octahedral sites in the spinel *Fd-3m* crystal structure provides a highly tunable and thus, thoroughly studied and investigated class of material,[6, 20-23] which is highlighted in the increased total number of publications in this field in the last 20 years (Figure 1). Especially cobalt, zinc, magnesium and nickel ferrites, attract the attention of many researchers. In contrast to mixed ferrites, which also gain a lot of attraction in these days, they are perfectly suited to study the interplay of the trivalent iron ions and the respective bivalent metal ions and, concomitant, onto the

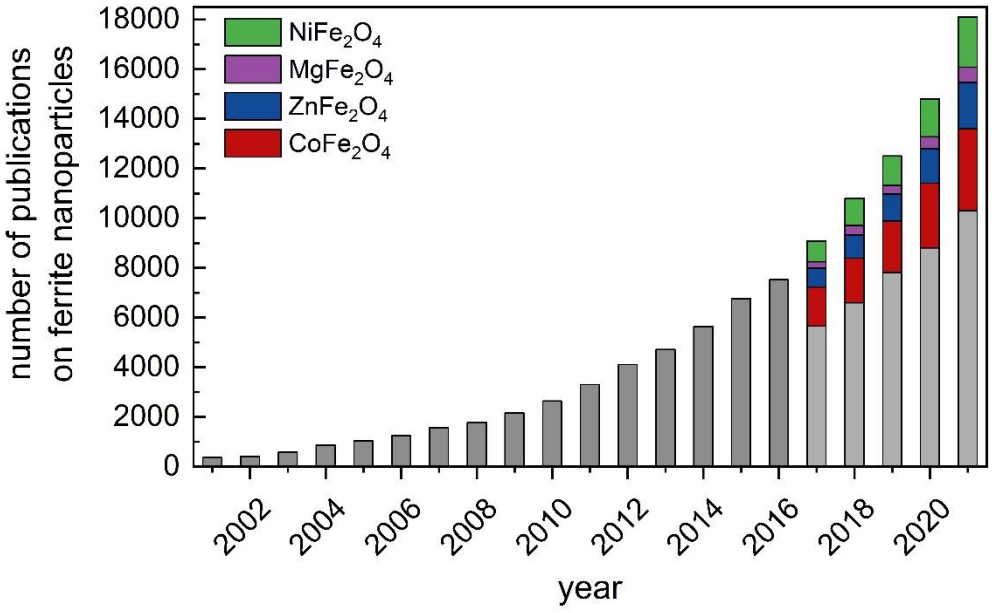

Figure 1: Progress of publication numbers on ferrite nanoparticles in the last 20 years. *Until 2016 the total number of publications is shown in grey. From 2017 on, the column is split in fractions of publications on cobalt (red), zinc (blue), magnesium (purple) and nickel (green) ferrites. All publications of other ferrites are displayed in bright grey. Statistics were evaluated by Google scholar on 21.02.2022.*

structure and chemistry of the ferrite nanoparticles. In biomedicine and ferrofluids throughout, the ferrite nanoparticles are used in dispersed state, which requires a very high colloidal stability (over months) at high concentrations (100 g L^{-1}) while being biocompatible. Thus, a thoroughly examination of the crystal structure as well as the surface composition of cobalt, zinc, magnesium and nickel ferrite nanoparticles is presented in this thesis.

Since dispersion of nanoparticles forces them to interact with the surrounding solvent, the solvent molecules undergo a restructuring process close to the nanoparticle surfaces. Just recently, atomistic insight into the molecular and dissociative adsorption of water molecules on facetted hematite nanoparticles was achieved theoretically by molecular dynamics (MD) simulations.[24-25] Experimentally, the restructuring of organic solvents and water at ZnO nanoparticles was proven by pair distribution function (PDF) analyses.[26-27] By means of PDF analysis in combination with X-ray absorption spectroscopy at 7 and 15 nm citrate-stabilized iron oxide nanoparticles (IONP) it was shown, that it is not possible to identify hydration shells around those nanoparticles. Instead, short-range ordered motifs of ethanol-water molecules form within the dispersion which are different from ethanol motifs in bulk ethanol.[28] The crystalline nature and shape of the nanoparticles determines the characteristic restructuring of water at such metal oxide nanoparticle surfaces.[24, 29] This opens multiple questions regarding the influence of particle size, atomic composition and surface functionalization of nanoparticles, which are targeted in this thesis.

2 State of the Art

In recent years, much progress was made in the synthesis of spinel ferrite nanoparticles to control the size, the shape and the structure as well as in the characterization of these type of material. In comparison to their bulk state, nanoparticles are less ordered due to their finite size and commonly used methods for the structure analysis of bulk materials, like XRD, are limited. First, the class of spinel ferrite nanoparticles is introduced and recent research summarized and, second, the benefits of the pair distribution function (PDF) for the characterization of materials which only have a short range order, like e.g. nanoparticles, glasses or liquids, is demonstrated. Finally, the procedure of the restructuring effect of solvent molecules around metal oxide nanoparticles and its elucidation by means of PDF analysis is presented.

2.1 Spinel Ferrite Nanoparticles

The structure of spinel ferrite nanoparticles with the sum formula MFe_2O_4, where M stands for a bivalent transition or post-transition cation like Mg^{2+},[30] Zn^{2+},[31] Ni^{2+},[32] Mn^{2+},[33] Cu^{2+},[34] Ca^{2+} or Co^{2+},[35-36] is related to the iron oxides magnetite and maghemite, where M in the formula would represent Fe^{2+} or a combination of Fe^{3+} and vacancies. The oxygen ions form a face-centered cubic crystal structure, where the metal ions occupy $\frac{1}{2}$ of the octahedral and $\frac{1}{8}$ of the tetrahedral sites. More exactly, one unit cell consists of 32 oxygen ions, which create 32 octahedral and 64 tetrahedral sites, where 16 and 8 are occupied by metal ions, respectively (see Figure 2).[37-38] In bulk materials, the probability which metal ions occupy tetrahedral or octahedral sites is defined by the ligand field theory (LFT), the cation radii and the electrostatic contribution to the lattice energy.[39] This results in three different occupation states which are classified in normal, inverse and mixed spinel structure and can be illustrated by the sum formula

$$(\mathrm{M}^{2+}_{1-\mathrm{x}}\mathrm{Fe}^{3+}_{\mathrm{x}})_{\mathrm{T}}[\mathrm{M}^{2+}_{\mathrm{x}}\mathrm{Fe}^{3+}_{2-\mathrm{x}}]_{\mathrm{O}}\mathrm{O}_4.$$

Parentheses marked with “T” represent tetrahedral and square brackets indexed with “O” represent octahedral sites. If $x = 0$, the normal spinel structure is present, e.g. $ZnFe_2O_4$,[40]

and the M^{2+} ions are located at the tetrahedral sites and Fe^{3+} ions only at the octahedral sites. In the inverse spinel structure (x = 1), M^{2+} ions occupy half of the octahedral sites and Fe^{3+} ions are located at residual half of the octahedral and all tetrahedral sites. Inverse spinels are e.g. $CoFe_2O_4$, $NiFe_2O_4$ and also Fe_3O_4.[41-43] For 0 < x < 1, e.g. in $MgFe_2O_4$,[44] the mixed spinel structure is present. However, when it comes to nanomaterials it is known that the inversion degree doesn't stick to the predefined state from their bulk materials and mostly crystallize in a mixed spinel structure.[45]

The present superexchange interactions between metal ions at the tetrahedral sites (T-T), between two octahedral sites (O-O) and between tetrahedral and octahedral sites (T-O) is accountable for variable properties of the spinel ferrites.[46] Most spinel ferrites show ferromagnetic ordering in the direction of the octahedral magnetic moment, as the T-O

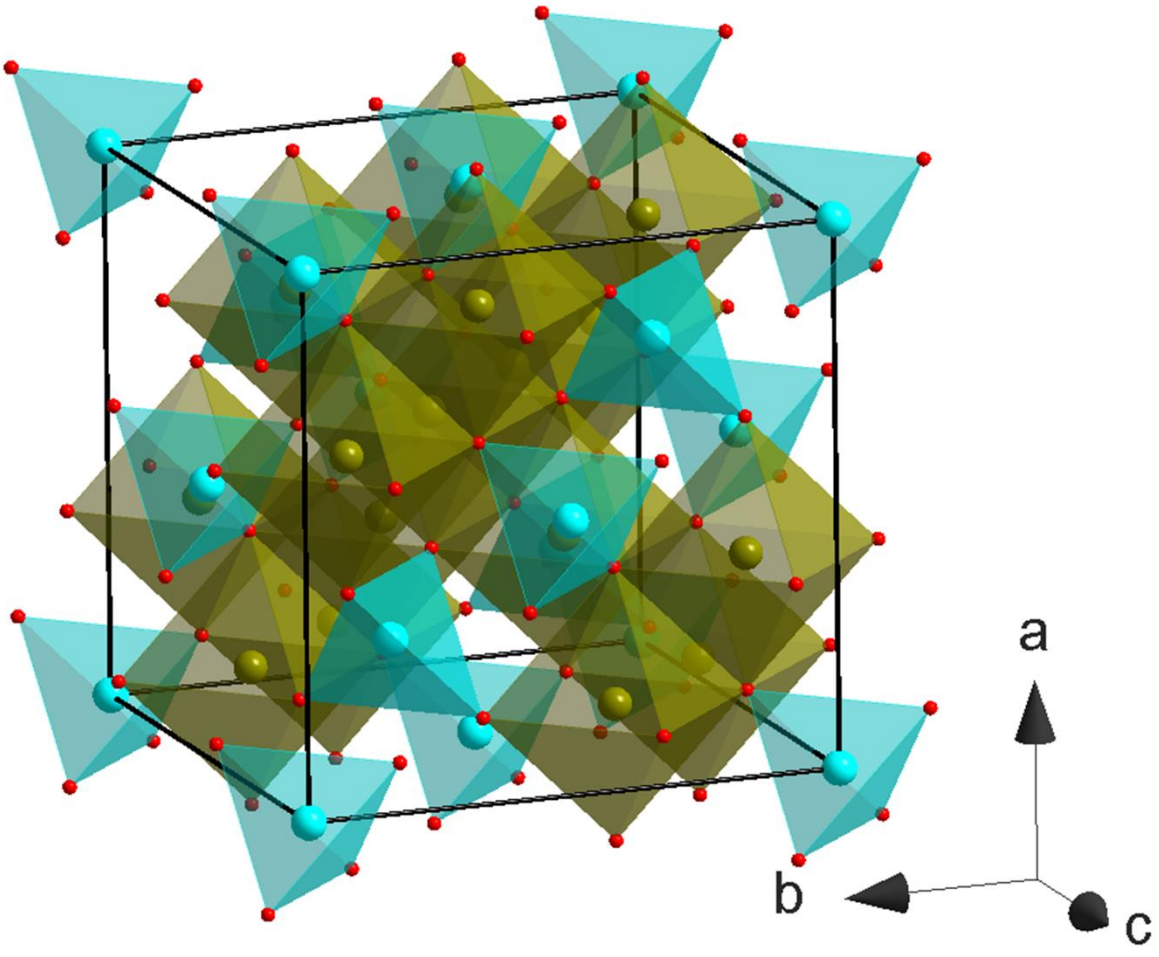

Figure 2: Schematic illustration of one unit cell of the cubic spinel structure Fd-3m. *Tetrahedral and octahedral cation sites are displayed in light blue and green, respectively. The red dots at the edges of the polyhedra mark the position of the oxygen ions.*

superexchange leads to antiparallel alignment of the magnetic moment on T and O sites and the fact that there are double the amount of O sites occupied by metal ions.[37, 45] Not only the size and shape of the nanomaterial and the kind of bivalent metal ion but also the distribution onto the different vacancies defines the magnetic, electric and chemical nature of this material. As in nanoparticles synthesis many parameters can be varied which influence the final product properties, a highly reproducible and controllable synthesis pathway is required for the synthesis of spinel ferrite nanoparticles.

2.1.1 Polyol Synthesis of Spinel Ferrite Nanoparticles

According to literature, much progress was made in the synthesis of nanoparticles in polyol media, esp. spinel ferrites and relative oxides, recently.[5, 47-48] The properties which make polyols highly suitable for such a synthesis are their

- high bowling point,
- high permittivity, and
- complexing ability.

The high bowling point enables reaction temperatures > 200 °C, which leads to highly crystalline particles and therefore higher M_S.[49-50] Their high permittivity in comparison to other organic solvents with a high bowling point permits access to ionic inorganic precursors like nitrates, acetates or chlorides.[51] Because of the existence of neighboring functional groups like alcohols or ethers like in e.g. 1,2-diols or etherglycols (Figure 3), polyols form complexes with precursor species and also stabilize the surface of the growing nanoparticle. This prevents Ostwald ripening and particle aggregation during the synthesis and, thus, leads to small particle size polydispersity.[51]

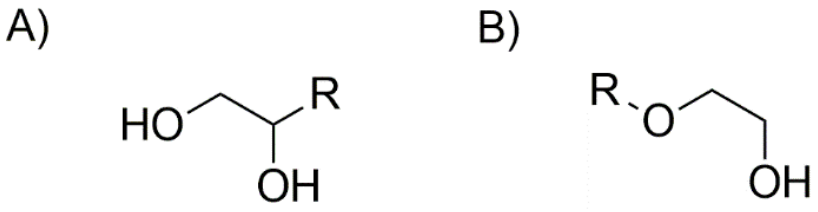

Figure 3: Valence formula of A) 1,2-diols and B) etherglycols. *R may be any organic structure.*

The benefits of the polyol synthesis route for nanoparticles were first observed in the 1990's in the synthesis of small copper, silver and gold particles.[52-54] The use of ethylene

glycol led to the development of highly controllable synthesis route for different shapes of silver nanomaterials.[55-56] Then, Feldmann et al. transferred the knowledge from metal and noble metal nanoparticles to metal oxides. They realized that for metal oxides the hydrolysis and not the reduction, as it is for noble metal nanoparticles, is the key step in the synthesis. Thus, a certain amount of water is needed in the reaction.[57] Inspired by those studies, Ammar and Caruntu et al. started to design a synthesis route for spinel ferrite nanoparticles in 1,2-propanediol and diethylene glycol, respectively. Those nanoparticles show a very low polydispersity in combination with a very high degree of crystallinity, which could be referred to the affinity of 1,2-diols or etherglycols (Figure 3) to form complexes and coordinate to the freshly emerged spinel ferrite nucleus and the high achievable reaction temperature.[5, 48] Despite this considerably high affinity of the polyol molecules to the ferrite nanoparticle, the interaction is weak enough for stronger stabilizers to replace the polyols. Such stabilizer involve long-chain fatty acids or carboxylic acids, for instance.[47] A post-synthetic ligand-exchange provides the opportunity to easily functionalize the particle surface to control dispersibility in polar or non-polar solvents or direct reaction pathways in catalysis.[58]

2.1.2 Colloidal Stability of Nanoparticles

In many applications where nanoparticles are used in dispersion, e.g. ferrofluids and biomedicine,[19, 59] a high colloidal stability is required to prevent coalescence and Ostwald ripening and thus, the growth of the nanoparticles which is inevitable followed by precipitation of the particles. To provide this colloidal stability three different methods can be applied, which are schematically visualized in Figure 4. The nanoparticles can be stabilized by an electrostatic layer, which contains counter-ions of the surface charge, e.g. Cl^- ions at a positive surface, or sterically by bulky molecules, e.g. oleic acid.[60] Also a combination of both methods, the electrosteric stabilization is possible by using smaller and charged molecules like citrate. When bulky or charged molecules are used, they need to possess a moiety which shows attractive interactions with the nanoparticles surface. This required kind of moiety may change due to the existing nanoparticle. For noble metals, π-backbonding capable groups like thiols (-SH) or phosphines ($-PH_3$) show a high attraction to the nanoparticle surface. In case of metal oxides and spinel ferrite nanoparticles, carboxyl, hydroxyl, amine and phosphoryl containing molecules are

favored. Due to the nature of transition metals, they act as Lewis acids. In aqueous solutions this will automatically lead to the dissociation of the water molecules close to the surface and to hydroxylation of the metal surface species. Depending on the pH of the solution a negative or positive charge of the adsorbed water molecule will contribute electrostatically to the stability of the nanoparticle.[61]

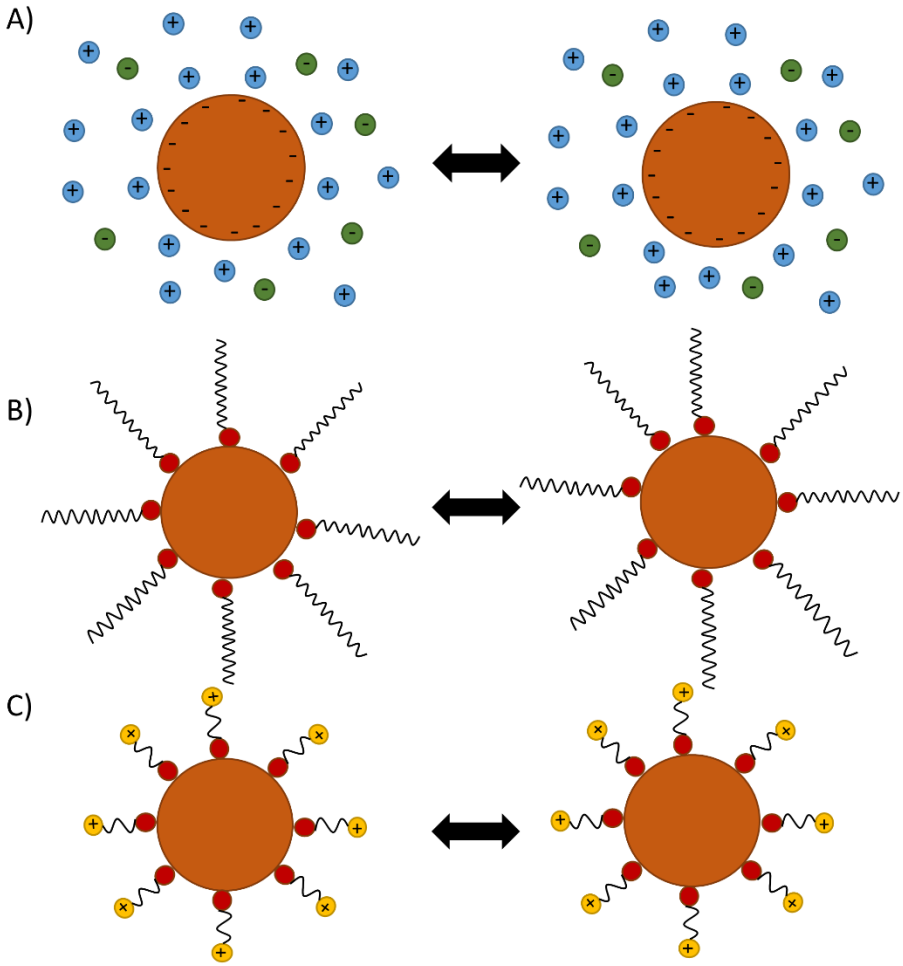

Figure 4: Schematic illustration of the A) electrostatic, B) steric and C) electrosteric stabilization of nanoparticles. *In the electrostatic stabilization, counter-ions of the nanoparticle surface charge are increased in the Debye layer, which causes electrostatic repulsion. Steric stabilization is achieved by bulky molecules possessing an anchor group to coordinate to the nanoparticle surface. The combination of both is the electrosteric stabilization, where smaller but charged molecules are used.*

Experimentally, the stabilization of nanoparticles is mostly done by a post-synthetic surface functionalization step. This could be straightforward with a one-pot strategy, where directly after the nanoparticle synthesis the desired stabilizer molecule is added to the reaction mixture and displaces the present surface species, which remains from the reaction.[61] Also, strategies with solvent mixtures or multistep “click-on” reactions are

applied to change the dispersibility of the nanoparticles from polar to non-polar solvents or to add additional functional moieties. In general, any desired functionality can be created, if the capping agent possesses a moiety with binding affinity to the nanoparticle surface. For iron oxide nanoparticles, Qu et al. identified various stabilizers, which in turn were accessible for further bioconjugation chemistry to load the nanoparticles with e.g. drugs, antibodies or cancer cells.[47] The surface modification of ferrite nanoparticles published by Shaikh et al. highlights the important role of the modifier species in catalytic reactions, as different surface modifiers lead to different selectivity and yield in solvent-free synthesis of 5-hydroxymethylfurfural.[58]

A high colloidal stability of nanoparticles in aqueous dispersion is in evitable to realize high concentrations of such dispersions. In case of magnetic nanoparticles, the magnetic response of such dispersion can be adjusted via the concentration.[12, 62-63] However, in many publications, which highlight the colloidal stability of their synthesized nanoparticles, the proof of the stability at high concentrations or for longer time periods is missing.[10, 62, 64-67] There, mostly dynamic light scattering (DLS) is used to demonstrate the colloidal stability, which, however, can only be performed at quite low concentrations (~ 5 g L^{-1}), as partial transmission of the light through the sample needs to be guaranteed. Examples can be found in literature. The stability of dispersions of phosphonic acid-stabilized cobalt ferrite nanoparticles was shown with DLS, but the measurements parameters, like concentration, were not given.[65] Dispersions of Polyethylene glycol (PEG) stabilized iron oxide nanoparticles (IONP) were tested for their colloidal stability at c = 1.0 g L^{-1} over time and temperature with DLS. At RT, they are stable for a minimum of 4 months. The temperature can be increased until 90 °C before their diameter increases. They even state the dispersibility of the freeze-dried powder. However, no proof was given and also no measurements at higher concentrations were made. The strong bond between the oxygen of the catechol groups with the surface metal ions of the nanoparticle and the overall high density of stabilizer molecules at the nanoparticles surface are responsible for the colloidal stability.[10] The fact that colloidal stability is also depending on pH and stabilizer concentration is also shown by Hajdu et al. on polyanion stabilized magnetite nanoparticles. The proof was given at a low concentration of 0.1 g L^{-1} and a long-term study is missing.[67] Particle concentrations of 300 g L^{-1} were achieved by Fan et al. They used viologene to stabilize their nanoparticles, impeding their use in biological

applications due to the toxicity of viologene. However, an analytical proof of the colloidal stability was not addressed at all.[66]

The surface characterization after the functionalization step is another critical point in colloidally stable nanoparticles. The quantity, identity and arrangement of the molecules on the nanoparticle surface highly affects the nanoparticle chemistry.[68] Stabilizer molecules, solvent molecules, reaction byproducts or precursor residues can be located at the surface. This diversity makes the quantitative and qualitative surface analysis challenging. The estimation of the surface coverage of inorganic nanoparticles is mostly done by thermogravimetric analysis (TGA). The mass loss is then attributed to the organic molecules and converted into molecule quantity per nm² nanoparticle surface. However, the decomposition products are not further analyzed, with e.g. gas chromatography or mass spectroscopy, and thus, the organic species remains unknown. Another approach, which is widely used, is the assumption that only the deployed amount of stabilizer molecules is entirely coordinated to the nanoparticle surface.[47] In fact, it is well known, that there is an equilibrium between stabilizer, solvent and other molecules, which leads to remaining uncoordinated stabilizer molecules in the solution as well as solvent molecules, esp. polyols, coordinating to the nanoparticle surface.[62, 69] The most promising strategy is the combination of different methods like nuclear magnetic resonance, elemental analysis, optical spectroscopy and X-ray photoelectron spectroscopy. However, as not all nanoparticle cores and stabilizer molecules are suitable for a certain method, the experimental constraints need to be evaluated.

2.1.3 Anisotropic Spinel Ferrite Nanoparticle

Alongside size and structure, the shape of nanomaterials highly affects their physical and chemical properties. Especially ferroelectricity, piezoelectricity, optical behavior and magnetism are dependent on the symmetry of the nanomaterial. However, as symmetry and the minimization of the surface energy is commonly thermodynamically favored, smart synthesis routes need to be designed to obtain stable anisotropic nanoparticles.[70] When talking about the shape of nanomaterials, four different main classes are defined. They include spherical (0D), elongated rod- or wire-like (1D), plate-like (2D) and complex 3D shapes like hexagons, cubes, stars, octahedra, etc.

Experimentally, the shape of the nanomaterials can be controlled by various physical, biological or chemical methods. In this thesis, the focus will be on the chemical driven shape control. To direct the shape of nanostructures during wet-chemical synthesis according to the LaMer mechanism,[3] the control of the growth step (**III** in Figure 5) is crucial. While at high concentrations the growth step is limited by the diffusion of the monomers which supports the formation of spherical nanoparticles, at low concentrations the surface reaction is kinetically directing, which supports the growth of certain crystal lattices, depending on the existing crystal structure.[70] Another approach is the use of surface coordinating solvent or ligand molecules, which favor specific lattice planes of the desired crystal structure. By the coordination the crystal growth at this lattice plane is hindered or at least slowed down, which results in an anisotropic growth as the crystal growth in the other direction is favored.[71] Nowadays however, it is well known, that the nanoparticle growth is a competition of different mechanisms including diffusion growth, Ostwald and digestive ripening, Finke-Watzky mechanism and coalescence. Considering all the thermodynamic and kinetic effects directing the growth mechanism during

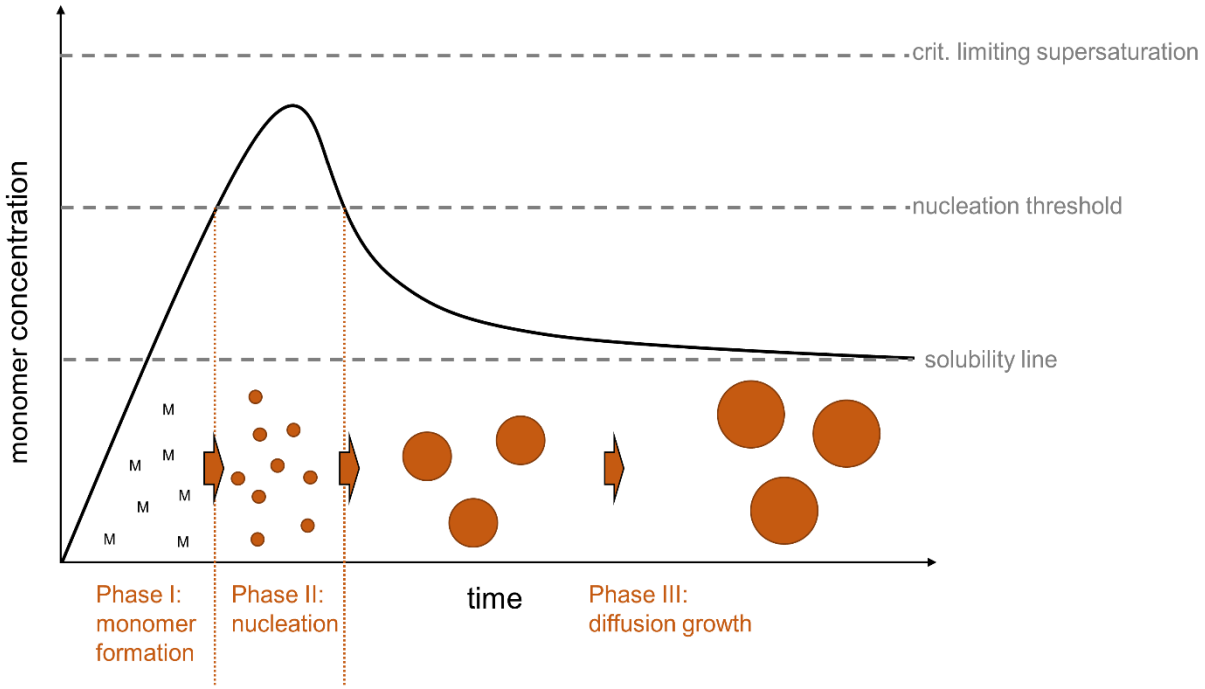

***Figure 5: Illustration of the classical LaMer mechanism.**[3] The concentration of monomers depending on reaction time is shown. Referred to spinel ferrite nanoparticles, the monomers are oxides and hydroxides of iron(III) the respective bivalent metal ion. First, their concentration increases by hydrolysis and reaches the critical oversaturation (**I**). There, spontaneous nucleation takes place at leads to a decrease of the monomer concentration (**II**). Once the monomer concentration drops under the critical nucleation concentration, no further nuclei are formed and the existing nuclei undergo diffusion controlled growth until the monomer concentration drops to the saturation concentration (**III**).*

nanoparticle synthesis, shape controlled nanoparticle synthesis is a very challenging task and the final shape is hard to predict. Yet, a full understanding of the general mechanism is still missing.[72-73]

Most shape-selective synthesis for metal oxides owing a spinel structure are applied for magnetite or related iron oxides. In the field of spinel ferrites, $CoFe_2O_4$ and $MnFe_2O_4$ are the most studied materials in recent years. Zeng et al. reported a seeded growth synthesis of $MnFe_2O_4$ polyhedra using a mixture of 1,2-hexadecandiol, oleic acid and oleylamine in benzyl ether as shape controlling ligands. In contrast, they were able to control the shape from spherical to cubic in a one pot synthesis. They used the same ligands but varied the precursor to ligand ratio. Increasing the amount of ligand leads to cubic nanoparticles, whereas a decrease results in spherical nanoparticles.[74] A similar approach was published by Song et al. on $CoFe_2O_4$. However, they obtained a cubic shape of their nanoparticles despite very similar parameters.[75] Lalwani et al. and Ji et al. synthesized $CoFe_2O_4$ nanorods by the use of oleic acid and cetyltrimethylammonium bromide as surface active ligand, respectively.[76-77] Both ligands bind preferably to specific crystal facets leading to a 1D crystal growth. Those practical examples indicate that, despite the various theoretical possibilities, the most common and predictable way to control the shape of spinel ferrite nanoparticles is the manipulation of the surface energy during particle growth by the incorporation of surface active ligands. As shown above, mixtures of ligands with different functional groups like diols, amines and carboxyls may favor a defined anisotropic particle growth.

2.1.4 Structure of Iron Oxide Nanoparticle

Iron oxides and especially iron oxide nanoparticles (IONP) attract a lot of interest in these days. Due to their biocompatibility, magnetic properties and low costs they are versatilely applied in biomedicine as e.g. drug carriers,[78] contrast agents in magnetic hyperthermia imaging[79] or hyperthermia cancer therapy.[80] The iron oxides maghemite (γ-Fe_2O_3) and magnetite (Fe_3O_4) are related to spinel ferrite nanoparticles, as they are based on the similar cubic crystal structure. As already mentioned in chapter 2.1, maghemite and magnetite differ in the oxidation state and the number of the iron ions in the unit cell, which consequently leads to vacancies in the maghemite structure in comparison to magnetite.

Those vacancies and their distribution in bulk maghemite were topic in many studies and were researched intensively. Four possible structures for maghemite were reported in the last decades. The most straightforward approach is based on the cubic magnetite crystal structure (*Fd-3m*) with a statistical distribution of the vacancies on the octahedral sites (Figure 6 B).[81] Secondly, Shmakov et al. proposed a related cubic crystal structure ($P4_332$) with a vacancy on exactly one of two possible octahedral sides.[82] According to Greaves, the vacancies are on one of three possible sites in a tetragonal $P4_32_12$ crystal structure (Figure 6 A).[83] Finally, Shmakov et al. and Jorgensen et al. proposed a $P4_12_12$ space group with a more complex vacancy ordering, which is a superstructure of three of the before mentioned $P4_32_12$ unit cells.[82, 84]

Due to the rather different structure solutions of even bulk maghemite, the task to elucidate the structure of a maghemite nanomaterial is even more challenging. Due to additional disorder, finite size and surface effects the significance of commonly used crystallographic characterization methods like XRD are limited. Additionally, in case of XRD, the occurring fluorescence by the use of the most common Cu Kα X-ray source and the nearly identical scattering power of Fe^{2+} and Fe^{3+} makes a structure solution on a nanometer scale hardly

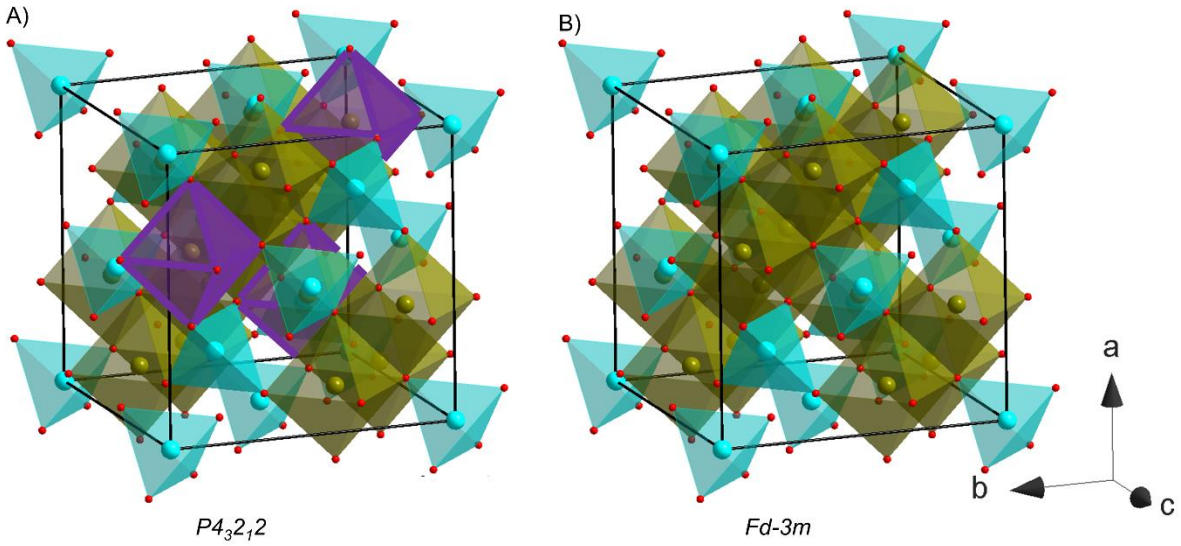

Figure 6: Schematic illustration of A) a $P4_32_12$ and B) Fd-3m unit cell of maghemite.[6] *Octahedral sites are green and purple and tetrahedral sites are light blue. Red balls represent oxygen ions. In A), the one vacancy can occur randomly on exact one of the purple highlighted octahedral sites. In structure B), the vacancies are distributed completely randomly on all octahedral sites. Mercury was used as software for the visualization of the crystal structures.*

possible. Thus, in most studies a clear structure solution is mostly missing and the nanomaterials are classified simply as IONP.[85] Recently, by the use of the pair distribution function (PDF) milestones in the characterization of IONPs were achieved. Cooper et al. reported that in 3 - 10 nm IONP, synthesized by continuous growth synthesis, vacancies not only occur at octahedral sites but as well on tetrahedral sites. Their nanoparticles are a mixture between maghemite and magnetite. This ratio shifts towards the oxidized maghemite structure depending on the storage time in air at room temperature. This oxidized structure likely exists preferential at the nanoparticle surface leading to a gradient of oxidation in the nanoparticles from the surface to the core.[6] Andersen et al. reported a combination of neutron scattering, synchrotron X-ray scattering and PDF analysis of IONP synthesized by a solvothermal flow synthesis. As a two-phase modelling of a magnetite (*Fd-3m*) and a maghemite ($P4_32_12$) phase to the experimental data did not yield in a satisfying structure solution, they assume a compositional gradient from a Fe-rich core to a more oxidized surface region.[85] Those studies are just two examples for the capabilities of PDF analysis.

2.2 The Pair Distribution Function

The PDF analysis is a powerful tool for the study of the structure of semi-crystalline or disordered materials like glasses, liquids or nanoparticles. Despite it is known and applied for many decades, the rise of the PDF analysis just started in the 2000's with pioneering works from the workgroups of Billinge, Petkov and Neder to name some examples.[86-88] As the PDF will be the most intensively used characterization method in this thesis, the theoretical principles, experimental implementation and final data evaluation will be presented in this chapter.

2.2.1 Theoretical Background

The PDF corresponds to a histogram of all interatomic distances in a sample as a function of the distance *r* in real space. Figure 7 shows this exemplarily on a simplified section of the $CoFe_2O_4$ (*Fd-3m)* crystal structure. The distances from each single atom to all other

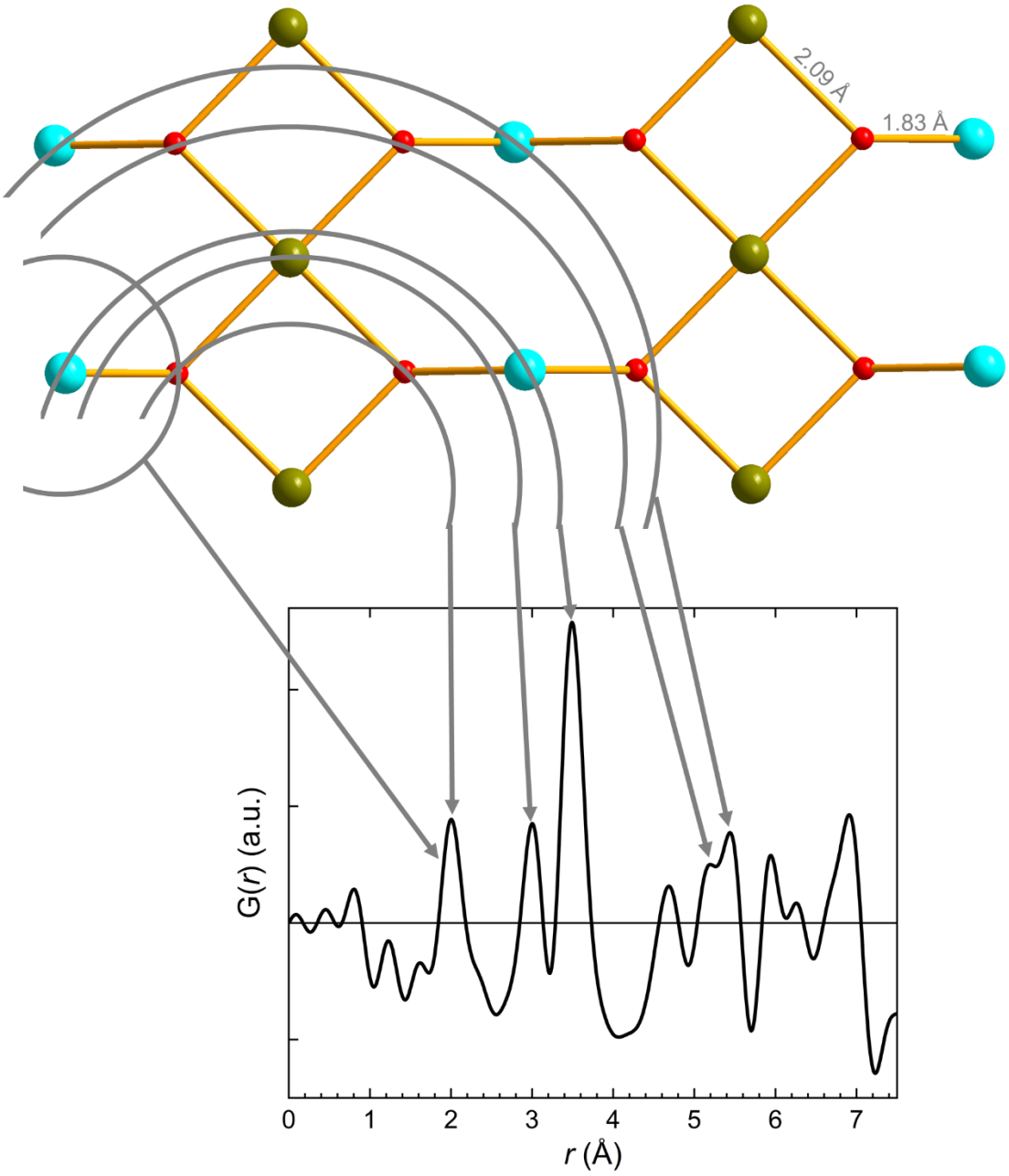

Figure 7: Schematic illustration of the content of a PDF on the example of a simplified section of the $CoFe_2O_4$ crystal structure. *Light blue and green balls stand for tetrahedral and octahedral sites, respectively. Red balls represent oxygen atoms. The tetrahedral sites are out of plain. G(r) describes the possibility of the existence of an atom pair with a certain distance r. If G(r) = 0, this possibility is equal to a completely amorphous structure. Maxima and minima correspond to an increased and decreased possibility, respectively.*

atoms are summed up and displayed as $G(r)$, which gives the possibility of the existence of a certain interatomic distance r in the sample. The theoretical calculation of $G(r)$ is given in Equation 1.[88]

$$G(r) = \frac{1}{r}\sum_{n}\sum_{m}\left[\frac{f_n f_m}{\langle f\rangle^2}\delta(r - r_{nm})\right] - 4\pi\rho_0 r \qquad \text{Eq. 1}$$

The sum of all interatomic distances r_{nm} between the atoms n and m is weighted by the atomic form factors f. The factor r^{-1} is a normalization and stems from the convolution of $G(r)$ with the termination function $\sin(Q_{max}\Delta r)/\Delta r$, which accounts for the limited range in Q. It corresponds to an additional broadening function.[89] With the subtraction of the term $4\pi\rho_0 r$, with ρ_0 as the average number density of all atoms in the sample, a r-depending baseline is introduced. This leads to an oscillation of the final PDF around 0.[90]

For $G(r) = 0$ this probability corresponds to a complete randomly organized statistical structure. Thus, peaks and minima give a higher and lower possibility of a certain interatomic distance, respectively. In this specific example of the $CoFe_2O_4$ structure, the peak at 2.0 Å corresponds to the Co/Fe-O distance. The next peaks at ca. 3.0 and 3.5 Å display the two closest interatomic distance between metal atoms divided in the O-O and O-T distance, respectively. In between, no pair of atoms exists, resulting in a negative $G(r)$. As the PDF is normalized to the atomic form factors, the peaks for the distance between metal atoms have a higher intensity than the peak of an atom pair which contains an atom of a lower order, e.g. oxygen.

2.2.2 Experimental Implementation

Experimentally, the PDF is gained by the sine Fourier transform of the normalized scattering intensity $S(Q)$ by Equation 2.

$$G(r) = \frac{2}{\pi}\int_{Q_{min}}^{Q_{max}} Q[S(Q) - 1]\, sin(Qr)\, dQ \qquad \text{Eq. 2}$$

$S(Q)$, also called total structure function, is experimentally accessible through X-ray, electron or neutron diffraction and includes not only the information from the Bragg peaks but also the diffuse scattering signal, which arises especially from non-crystalline and

amorphous structures. Because of this, PDF analysis is also called a total scattering method. *Q* is the wave vector and depending on the wave length λ and the scattering angle θ (Equation 3).[86]

$$Q = \frac{4\pi sin\theta}{\lambda} \quad \text{Eq. 3}$$

Equation 2 implies that the best resolution of the final PDF data would be given for $Q = \infty$. However, as this is experimentally not possible, the *Q* space is cutoff at a certain point. This leads to a decrease in the real space resolution and also causes the so called termination ripples, which are visible in Figure 7 between $Q = 0 – 1.6$ Å. They are residues from the Fourier transformation, which can be dampened by different approaches to avoid misinterpretation of the data.[91]

As mentioned above, a high *Q* – range is necessary for achieving a high resolution in *r*. According to Equation 3, this is possible by the use of a shorter wavelength and thus, a higher energy of the incoming X-ray or neutron beam. At a laboratory X-ray device, this can be achieved by the use of Mo (ca. 17 keV) or Ag (ca. 22 keV) X-ray sources. Even more suitable are high energy synchrotron beamlines, where energies up to 100 keV can be achieved. However, only high energy does not satisfy the needs for an optimal PDF quality. Due to technical limitations in detector pixel size, the resolution of *Q* decreases with increasing energy of the incident beam and leads to a *r*-dependent dampening of the PDF peaks. Consequently, before every PDF measurement a compromise between the best possible resolution, a sufficient peak intensity and sufficient Q_{max} must be evaluated.[92]

2.3 Restructuring of Solvents at Nanoparticle Surfaces

In recent years, the experimental proof of the restructuring of polar and non-polar solvent molecules around metal oxide nanoparticles in dispersions was given by means of PDF analysis. In detail, primary alcohols, water and hexane tend to form up to three distinct shells of solvent molecules, which reach up to ca. 2 nm from the nanoparticle surface.[26-27] Transferred to IONPs in aqueous dispersions, molecular dynamics (MD) simulations at

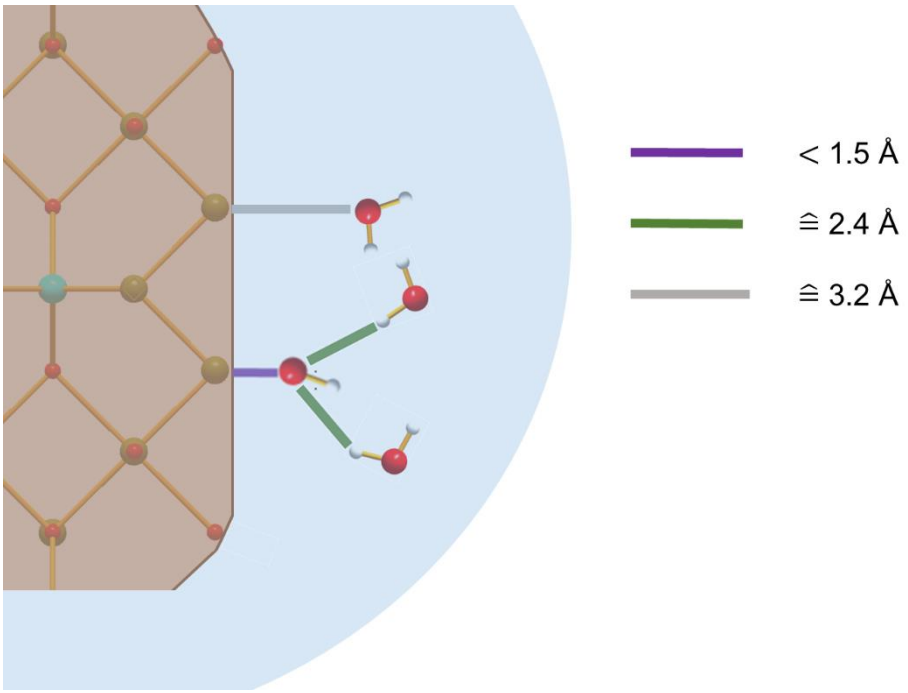

Figure 8: Scheme of the assignment of interatomic distances extracted by MD simulations to three different binding modes in the adsorbed water layer at hematite nanoparticles.[4] *The three distances are highlighted by three different colors and assigned to the hematite surface with the same color.*

the *001* surface of hematite nanoparticles predict 3 distinct hydration layers up to 3 Å from the surface, which can be assigned to hydroxyl groups bound to surface iron ions, molecular water interacting with adsorbed hydroxyls, and molecular water interacting with surface iron ions (Figure 8). Between 4 and 20 Å, three to five loosely bound hydration layers exist.[4, 24] For 7 and 15 nm IONP stabilized with different organic molecules, such distinct hydration layers couldn't be revealed.[28]

For iron oxide related nanoparticles like spinel ferrite nanoparticles, the influence onto the nature of the hydration shell caused by the substitution of Fe^{2+} ions by other bivalent metal ions like Mg^{2+}, Co^{2+} or Ni^{2+} is still unknown. Only Kumar et al. reported a theoretical study based on the density functional theory with on-site correction that the incorporation of nickel ions favors the dissociation of water molecules at the (111) surface of $NiFe_2O_4$ surfaces in comparison to the (111) Fe_3O_4 surface.[50]

For gaining the insight into the hydration shell experimentally, it is necessary to measure at least one complete dataset composed of the nanoparticle dispersion, the pure solvent and the dry nanoparticle powder. It is very important that the instrumental measurement parameters are equal to eliminate the instrumental impact. To extract the hydration shell

signal, first the signal from the pure solvent is subtracted from the signal of the nanoparticle dispersion. This results in the difference-PDF (d-PDF), which now contains the signal of the nanoparticle powder and the hydration shell. Second, the PDF from the dry nanoparticle powder is normalized to the d-PDF at large distances at $Q \approx 20$ Å. At this distance, no signal of the hydration shell is expected. The normalized nanoparticle PDF is then subtracted from the d-PDF, resulting in the double-difference PDF (dd-PDF), which now only contains the signal of the hydration shell.[26] Thus, the majority of the overall intensity is subtracted in this approach, as the hydration shell signal is less than 1 % of the initial signal of the dispersion. Thus, high accuracy and diligence is needed to perform this kind of measurement.

3 Experimental

3.1 Instruments and Software

TEM measurements were performed with a JEOL JEM-2200FS field emission energy filtering transmission electron microscope (FE-EFTEM) operated at an acceleration voltage of 200 kV. Zero-loss filtered micrographs (ΔE ~ 0 eV) were recorded with a bottom-mounted CMOS camera system (OneView, Gatan) and processed with DM 3.3 image processing software (Gatan). For each sample, 4 µL of very diluted nanoparticle dispersion was drop-casted on a carbon-coated meshed copper grid and dried in air. Particle sizes were obtained by counting 100 particles from at least three images.

Evaluation of the **hydrodynamic diameters** and **zeta potential** of the nanoparticles was performed with a Particle Analyzer Litesizer 500 (Anton Paar, Germany) at 25 °C in the automatic mode with a wavelength of 660 nm. The concentration of the nanoparticles was adapted so that the intensity was at least 300 kcounts sec^{-1}, which was ca. 0.5 wt%. Calculation of the number-weighted hydrodynamic radii was based on refractive indices and absorption coefficients from [93]. The zeta potential was calculated via the Smoluchowski approximation.

Small angle X-ray scattering patterns were recorded with the laboratory SAXS system “Ganesha-Air” from (SAXSLAB, Xenocs) by Dr. Martin Dulle at Forschungszentrum Jülich GmbH. The X-ray source is a D2-MetalJet (Excillum) operating at 70 kV and 3.57 mA with Ga-Kα radiation (λ = 0.1341 nm) providing a very brilliant and a very small beam (< 100 µm). The beam was focused with a focal length of 55 cm using a specially made X-ray optic (Xenocs). Measurements were done in 2.1 mm borosilicate glass capillaries (Hilgenberg), code 1409364, Germany) at room temperature, and the transmitted intensity data were recorded by a position-sensitive detector (PILATUS 300 K, Dectris). To cover the range of scattering vectors between 0.026 and 3.0 nm^{-1}, different detector positions were used. The circularly averaged data were normalized to incident beam, sample thickness, and measurement time before subtraction of the solvent. All measurements were put on an absolute scale by standard-less absolute intensity calibration. Dispersions for SAXS measurements had typical concentrations of 5 g L^{-1} and high concentration

measurements were performed at 50 and 100 g L^{-1}. Fitting of the data was performed using SASView 4.2.2[94] and JScatter[95].

Powder X-ray diffraction was carried out at room temperature with a STOE STADI P Mythen2 4K diffractometer (Ge(111) monochromator; Ag Kα1 radiation, λ = 0.5594 Å) using four Dectris MYTHEN2 R 1K detectors in Debye–Scherrer geometry in moving mode. The Q-range was 0.4 to 20.4 $Å^{-1}$ with a step size of 0.015 $Å^{-1}$. Samples were measured in 0.5 mm diameter glass capillaries purchased from Hilgenberg (special purpose glass number 10). For more information on this dedicated diffractometer for pair distribution function analysis, see [96].

PDF data were collected at the above mentioned laboratory diffractometer. Measurements times were between 14 and 24 h to achieve a satisfying signal to noise ratio for the Fourier transformation. PDF data were also collected at dedicated PDF beamlines at synchrotrons in Hamburg (PETRA III, beamline P21.1, E = 101 keV) and Grenoble (ESRF, beamline ID31, E = 65 keV). Samples were measured in 1.0 mm diameter Kapton® capillaries (wall thickness 50 µm) purchased from Goodfellow. For data collection a Pilatus2M CdTe area detector from Dectris was used. The detector and beamstop alignment was done to achieve a minimum Q-range of 0.5 to 20 $Å^{-1}$. Measurement times are sample dependent and were chosen to get a sufficient signal-to-noise ratio. At PETRA III, powder samples were measured up to 200 s and liquid samples up to 1200 s. At ID31, powder samples were measured for 10 s and liquid samples for total times of 30 to 60 s.

PDF data processing was carried out with xPDFsuite[97]. The applied Q_{max} is sample dependent and ranges from 12.6 to 24.2 $Å^{-1}$ in this thesis. Fitting was done with DiffPy-CMI[98] and PDFgui[99]. For the lab instrument data, NIST LaB_6 standard measurements and for synchrotron data NIST Ni or Si (PETRA III) and CeO_2 (ESRF) standard measurements were used to calibrate geometrical parameters (Table A 1). Instrumental resolution parameters q_{damp} and q_{broad} for each beamtime, resp. instrument were determined by a refinement of the standard sample (Table A 2).

Thermogravimetric analysis measurements were performed from 30 – 1000 °C on a STA PT16000 (Linseis, Germany) with a heating ramp of 10 °C min^{-1} under argon atmosphere.

Elemental analysis of the nanoparticle powders was conducted with a Elementar vario EL III. 2 mg of dry nanoparticle powder was used per sample run.

Samples for **ICP-OES** were prepared by dissolving 0.1 g L^{-1} of the synthesized nanoparticles in an aqueous solution of 37 % HCl. The measurements were performed with a Varian Vista-Pro equipped with an ASX-510 autosampler.

Infrared spectra were collected with a JASCO FT/IR-6100 Fourier transform infrared (FT-IR) spectrometer with attenuated total reflectance (ATR) unit. Before the measurement, the instrument was flushed with nitrogen for 30 min. The spectra of an aliquot of dry nanoparticle powder were collected from 4000 – 400 cm^{-1} (0.25 cm^{-1} step size) and normalized to the transmittance at 4000 cm^{-1}.

Magnetic measurements were collected using a superconducting quantum interference device (SQUID) MPMS-XL5 instrument from Quantum Design. The field measurements at 300 K were performed in the hysteresis mode, in steps of 500 Oe from 100 Oe to 30 000 Oe and then down to -30 000 Oe. The samples were prepared in gelatin capsules held in a plastic straw. The raw data were corrected for the diamagnetism of the sample holder.

3.2 Synthesis of Spherical Spinel Ferrite Nanoparticles

3.2.1 Standard Synthesis in Polyol Solvents

Spherical, water-dispersible ferrite nanoparticles (MFe_2O_4; M^{2+} = Co^{2+}, Fe^{2+}, Mg^{2+}, Mn^{2+}, Ni^{2+}, Zn^{2+}) with diameters ranging from 3 – 5 nm were synthesized, their structure and surface analyzed and the interaction with surrounding water molecules in colloidally stable aqueous dispersions investigated.

Chemicals for the nanoparticle synthesis were purchased and used without further purification: ethanol absolute (VWR), diethylene glycol (99 %, Alfa Aesar), sodium hydroxide pellets (Merck), hydrochloric acid solution (in water 1 M, Grüssing GmbH), acetone and ethyl acetate (analytical grade, Fisher Scientific), cobalt(II) chloride hexahydrate (ACS reagent, ≥98 %, Merck), nickel(II) chloride hexahydrate (≥98 %, abcr), iron(II) chloride tetrahydrate (Glentham Life Sciences), magnesium hexahydrate (BioXtra, ≥98 %), zinc(II) chloride (puriss., ≥98 %) and iron(III) chloride hexahydrate (puriss. p.a. reag., ≥99 %, all Sigma Aldrich). Ligands for the nanoparticle surface modification were obtained as follows: phosphocholine chloride calcium salt tetrahydrate (98 %) from abcr, betaine anhydrous (98 %) from Alfa Aesar and trisodium citrate dihydrate (99 %) from Grüssing GmbH. Milli-Q water was used for the preparation of all dispersions.

Water-dispersible spinel ferrite nanoparticles with diameters of 3 to 5 nm were obtained via hydrolysis of diethylene glycol (DEG) chelate complexes of Fe^{3+} and M^{2+} (M^{2+} = Mg^{2+}, Co^{2+}, Ni^{2+}, Fe^{2+} or Zn^{2+}) according to Caruntu et al.[5] In a standard synthesis, $MCl_2 \cdot n\ H_2O$ (1 mmol) and $FeCl_3\ 6\ H_2O$ (2 mmol) were dissolved in DEG (20 g). A solution of NaOH (8 mmol) in DEG (40 g) was added. The reaction solution was then degassed with argon for 2 hours and subsequently heated to 220 °C with a heating rate of 2.17 K min^{-1}. The temperature was kept constant for 1 hour and then cooled to about 100 °C. Solutions of 3 mmol capping agent in DEG/H_2O mixtures were prepared (Table 1) and added to the reaction.

Table 1: DEG and H_2O volume for capping agent solutions.

capping agent	V_{DEG} (mL)	V_{H2O} (mL)
citrate	1.5	1.5
betaine	3	1
phosphocholine	3	4

It was stirred for another hour while cooling to room temperature. The nanoparticle powder was precipitated by addition of acetone and isolated with a permanent magnet. For purification, the powder was washed with acetone and absolute ethanol three to five times and dried at room temperature. All nanoparticle powders are redispersible in water or HCl solution (see Table A 3) up to a concentration of 100 g L^{-1}, at least.

The content of the organic stabilizer molecules for citrate- and phosphocholine-stabilized samples was reduced by dialysis against H_2O. Therefore, a nanoparticle dispersion (c = 10 g L^{-1}) was placed in a dialysis hose (Nadir®, cellulose hydrate; Roth) and sealed. For each 10 mL of nanoparticle dispersion, a beaker was filled with 1.0 L H_2O and the dialysis tube was placed in the beaker under gentle stirring for 16 h. The nanoparticle dispersion was filtered by a syringe filter (Chromafil® Xtra; PA, 0.2 µm pore size) and freeze dried.

3.2.2 Synthesis Variations for Larger $CoFe_2O_4$ Nanoparticles

Different approaches for obtaining larger 8 – 10 nm spinel ferrite nanoparticles were realized to investigate nanoparticle properties as function of the size. As the synthesis route mainly impacts the structure of the resulting nanoparticles,[31] the presented polyol route using DEG as solvent was altered step-by-step. All results are summarized in Table 5.

Alteration of the temperature, heating ramp and holding time was done according to Table 2. All other parameters were set constant.

Table 2: Variation of temperature, heating ramp and holding time.

sample	heating ramp (K min^{-1})	T_{max} (°C)	holding time (h)
t1	2.17	220	16
T1	2.17	240	1
T2	2.17	180	1
R1	1.08	220	1
R2	4.34	220	1

At first, the ageing time at T_{max} was elongated from 1 to 16 h to further enhance ageing of the nanoparticles (sample **t1**). This resulted in only slightly larger particles with d_{DLS} = 6.5 nm (PDI: 0.26). Variation of T_{max} to higher (240 °C, **T1**) and lower (180 °C, **T2**) temperatures lead in both cases not to the formation of $CoFe_2O_4$ nanoparticles likely to side reactions due to decomposition of DEG and insufficient nucleation rate, respectively. Lowering the heating ramp should lead to a lower concentration when nucleation of the

nanoparticles starts and thus, according to LaMer et al.[3], less nuclei should be formed but the growing of those nuclei should be increased. This should overall result in larger nanoparticles. On the opposite, enhancement of the heating ramp should lead to a higher concentration of precursor ions and, according to LaMer et al., to more nuclei, which grow less. This should result in overall smaller nanoparticles. Both was experimentally tested and the lowering of the heating ramp to 1.08 K min^{-1} (**R1**) resulted in $CoFe_2O_4$ nanoparticles but with a diameter equal to the standard synthesis (d_{DLS} = 4.3 nm (PDI: 0.21)). As expected, the enhancement of the heating ramp to 4.34 K min^{-1} (**R1**) resulted in very small amorphous nanoparticles (d_{DLS} = 1.8 nm (PDI: 0.23)).

The theory by LaMer was also tested by the variation of the initial precursor concentration. As already discussed above, lower concentrations should result in larger and higher concentrations in smaller nanoparticles. For all four syntheses (**C1 - C4**), the resulting nanoparticles diameter didn't differ from the nanoparticles obtained by the standard experiment. No correlation between the starting precursor concentration and the final nanoparticle diameter could be made. This could be an indication that this hydrolysis controlled synthesis didn't follow the LaMer theory. For all obtained diameters see Table 5. For testing different precursor concentrations, the volume of DEG was set constant and different amounts of precursor, which is shown in Table 3, are used.

Table 3: Precursor amount used for studying the impact of the precursor concentration on the nanoparticles size.

sample	n_{CoCl2} (mmol)	n_{FeCl3} (mmol)	n_{NaOH} (mmol)
C1	0.4	0.8	3.2
C2	0.6	1.2	4.8
C3	0.8	1.6	6.4
C4	1.2	2.4	9.6

Another possibility to vary the final nanoparticle diameter is to control the hydrolysis, which is the main reaction step in this nanoparticles synthesis (Scheme 1), by the addition of water to the reaction mixture (Table 4). As shown in Table 4, the addition of water lead to a decrease in the reachable T_{max}, as the addition of H_2O lowers the boiling point of the

DEG/H_2O mixture. For **W3** and **W4**, this yielded in larger nanoparticles according to DLS measurements (d_{DLS} = 7.1 and 8.9 nm). Despite the maximum reaction temperature was not reached, the nanoparticles clearly consisted of crystalline $CoFe_2O_4$ (Figure 9). For **W3**, reflections from a residual crystalline citrate phase, which was used as stabilizer, was present.

Table 4: Amount of H_2O added to the standard synthesis and the corresponding T_{max} for this synthesis.

sample	V_{H2O} (mL)	T_{max} (°C)
W1	0.5	220
W2	1.0	219
W3	2.0	209
W4	5.0	176

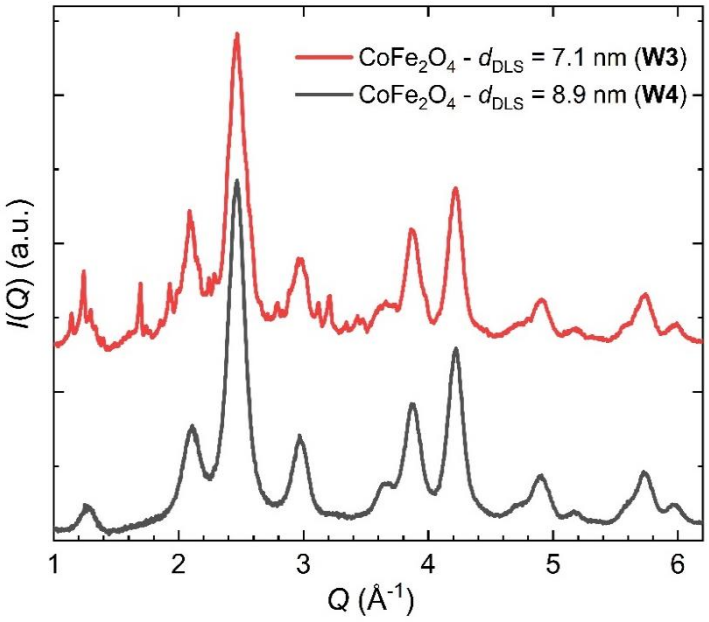

Figure 9: Background-corrected XRD patterns of dry powders of 7.1 (red, W3) and 8.9 nm (black, W4) citrate-stabilized $CoFe_2O_4$ nanoparticles according to DLS measurements (background = empty capillary; patterns stacked for clarity). *The nanopowders are crystalline and can be indexed with the cubic spinel structure Fd-3m. In the red pattern for sample **W3**, small sharp peaks stem from residual citrate. Data were collected STOE STADI P.*

PDF analysis (Figure A 1 and Table A 4) of sample **W4** revealed an average crystallite size of 4.5 nm, which is distinctly smaller than the diameter obtained from DLS measurements. As DLS shows the hydrodynamic particle diameter including a bound hydration layer, a larger diameter of ca. + 1 nm was expected. However, the difference

between PDF and DLS diameter of the $CoFe_2O_4$ nanoparticles shown here is 4.4 nm and far too large for a bound hydration layer. This shows that the addition of water and hence, the increase of the hydrolysis rate lead to coalescence of the nanoparticles, as the average nanoparticle likely wasn't single crystalline but consists of 2 to 3 coherent crystallites. The XRD pattern of the cobalt ferrite phase in **W3 and W4** are very similar and both *311* reflections at $Q = 2.67$ Å^{-1} have a FWHM of 0.148 Å^{-1}. Therefore, coalescence was also expected for sample **W3**.

The hydrolysis step can also be influenced by the variation of the complexing agent of the metal ions, which in this case was also the solvent. Partial and full replacement of DEG by NMDEA was suggested by Caruntu et al. to control the size of IONP, as their physical properties are similar but their complexing properties are different.[64] Due to the higher electron donor ability of NMDEA, hydrolysis should occur at higher temperatures and at a slower rate. This leads to less oversaturation, thus less nuclei and larger particles. Both approaches were tested twice with NMDEA from different supplier in the cobalt ferrite nanoparticles synthesis and none of them yielded nanoparticles. It has to be noted that T_{max} of 220 °C wasn't reach in either of the two approaches. Experimentally, for the DEG/NMDEA mixture (**S1**), the metal precursors were dissolved in a mixture of 10 g DEG and 10 g NMDEA and the NaOH was dissolved in 20 g DEG and 20 g NMDEA. Holding time at T_{max} was 3 h. For pure NMDEA (**S2**), precursors were dissolved in 20 g NMDEA and NaOH in 40 g NMDEA and the holding time at T_{max} was 4 h. In the DEG/NMDEA mixture (**S1**) 205 °C and in pure NMDEA (**S2**) 195 °C were achieved. Likely, both batches of NMDEA had a certain amount of impurity with a lower boiling or degradation temperature, which hindered the reaction temperature to rise until 220 °C.

Table 5: Summary of different approaches to obtain larger $CoFe_2O_4$ nanoparticles via the polyol synthesis route.

sample	varied parameter	result
t1	ageing time at T_{max} = 16 h	slightly larger crystalline $CoFe_2O_4$ NPs d_{DLS} = 6.5 (PDI: 0.26)
T1	T_{max} = 240 °C	no formation of $CoFe_2O_4$ NPs
T2	T_{max} = 180 °C	no formation of $CoFe_2O_4$ NPs
R1	decreased heating rate (1.08 K min^{-1})	crystalline $CoFe_2O_4$ NPs d_{DLS} = 4.3 (PDI: 0.21)
R2	increased heating rate (4.34 K min^{-1})	amorphous smaller $CoFe_2O_4$ NPs d_{DLS} = 1.8 (PDI: 0.23)
C1	decreased precursor concentration (factor: 0.4)	crystalline $CoFe_2O_4$ NPs d_{DLS} = 5.5 (PDI: 0.26)
C2	decreased precursor concentration (factor: 0.6)	crystalline $CoFe_2O_4$ NPs d_{DLS} = 4.6 (PDI: 0.23)
C3	decreased precursor concentration (factor: 0.8)	crystalline $CoFe_2O_4$ NPs d_{DLS} = 5.5 (PDI: 0.24)
C4	increased precursor concentration (factor: 1.2)	crystalline $CoFe_2O_4$ NPs d_{DLS} = 4.5 (PDI: 0.21)
W1	addition of 0.5 mL H_2O	crystalline $CoFe_2O_4$ NPs d_{DLS} = 4.7 (PDI: 0.28)
W2	addition of 1.0 mL H_2O	crystalline $CoFe_2O_4$ NPs d_{DLS} = 4.9 (PDI: 0.28)
W3*	addition of 2.0 mL H_2O	crystalline $CoFe_2O_4$ NPs d_{DLS} = 7.1 (PDI: 0.32)
W4*	addition of 5.0 mL H_2O	crystalline $CoFe_2O_4$ NPs d_{DLS} = 8.9 (PDI: 0.25)
S1	DEG/NMDEA mixture	no formation of $CoFe_2O_4$ NPs
S2	pure NMDEA	no formation of $CoFe_2O_4$ NPs

* T_{max} was not achieved.

Another approach tested is the seeding growth method, which was published by Cheah et al. for IONP.[100] In this thesis, cobalt ferrite nanoparticles obtained from the standard synthesis without ligand exchange were used as initial seeds and added to three different growth solutions containing $CoCl_2$ and $FeCl_3$ in DEG (**G1** - **G3**). They were heated according to the standard reaction protocol. Experimental details and the final particle diameters and distributions are summarized in Table 6 and Table 7, respectively. Instead of nucleation, the additional precursor should crystallize on the surface of the seeds and end up in larger, size-adjustable nanoparticles. However, the diameter of the nanoparticles obtained didn't differ much from the standard synthesis according to DLS analysis. Additionally, no correlation between the precursor concentration and the final nanoparticle diameters could be made.

Table 6: Amount of precursors and solvent for the preparation of the initial seeds and the growth solutions for seeding growth experiments. *The mass given for DEG is divided in the amount used for the NaOH and the precursor solution, respectively.*

	n_{CoCl2} (mmol)	n_{FeCl3} (mmol)	n_{NaOH} (mmol)	m_{DEG} (g)
initial seeds	0.5	1.0	4.0	20 + 10
growth solution				
G1	0.5	1.0	4.0	20 + 10
G2	0.75	1.5	6.0	20 + 10
G3	1.0	2.0	8.0	20 + 10

Table 7: Summary of seeding growth approaches to obtain larger $CoFe_2O_4$ nanoparticles via the polyol synthesis route.

sample	result
G1	crystalline $CoFe_2O_4$ NPs ; d_{DLS} = 6.3 (PDI: 0.13)
G2	crystalline $CoFe_2O_4$ NPs ; d_{DLS} = 5.3 (PDI: 0.20)
G3	crystalline $CoFe_2O_4$ NPs ; d_{DLS} = 5.7 (PDI: 0.20)

In summary, despite there are some published synthesis routes to control the size of IONPs, like the substitution of the complexing agent or the seeding growth method, those synthesis routes didn't work for $CoFe_2O_4$ nanoparticles. The variation of the parameters like heating ramp, aging time, T_{max} and the precursor concentration couldn't be correlated with the final overall nanoparticles diameter. It can be suggested that the polyol synthesis of spinel ferrite nanoparticles didn't follow the LaMer theory and was driven by other forces.[101] In fact, the only synthesis route shown here which lead to an increased nanoparticle diameter is the addition of H_2O to enhance the hydrolysis reaction. However, as the addition of water decreased the achievable T_{max} this synthesis was limited at approximately 5 mL of additional water. Otherwise crystalline side phases could occur.

3.3 Synthesis of Anisotropic $CoFe_2O_4$ Nanoparticles

Cubic and rod-like $CoFe_2O_4$ nanoparticles were prepared by Ms. Denise Schweser (University of Bayreuth) during her bachelor thesis.

Chemicals for the nanoparticle synthesis were purchased and used without further purification: cobalt(II) acetylacetonate (>99 %) and iron(III) chloride hexahydrate (puriss. p.a. reag., ≥99 %, Sigma Aldrich), iron(III) acetylacetonate (>97 %, Fluka), diphenyl ether (99 %), dibenzylether (>98 %), 1-octadecen (tech., 90 %), 1-octadecandiole (97 %), oleic acid (tech., 90 %, all Alfa Aesar), 1,2-hexadecandiol (>98 %) and sodium oleate (>97 %, TCI), oleylamine (80 – 90 %, Acros), ethanol absolute and n-hexane (analytical grade, VWR), cobalt(II) chloride hexahydrate (ACS reagent, ≥98 %) and sodium hydroxide pellets (Merck), acetone (analytical grade, Fisher Scientific). Ligands for the nanoparticle surface modification were obtained as follows: phosphocholine chloride calcium salt tetrahydrate (98 %, abcr), trisodium citrate dihydrate (99 %, Grüssing GmbH) and polyethylene glycol (MW 20000, Alfa Aesar). Milli-Q water was used for when the use of water is mentioned.

3.3.1 $CoFe_2O_4$ Nanocubes

$Co(acac)_2$, $Fe(acac)_3$, dibenzyl ether, 1,2-hexadecanediol, oleic acid and oleylamine were heated (8 K min^{-1}) to 110 °C and degassed with Argon for 1 h. After heating up to 210 °C (8 K min^{-1}) for 2 h, the temperature was raised to 295 °C (4 K min^{-1}) and kept constant for 2 h. A severe reaction takes places due to emerging gas during the reaction. The mixture was allowed to cool to RT and the nanocubes were precipitated and washed three times with EtOH with assistance of a permanent magnet.

Table 8: Reactant quantity for the synthesis of $CoFe_2O_4$ nanocubes.

reagent	***n* (mmol)**	***m* (g)**	***V* (mL)**
$Co(acac)_2$	1.0	0.257	
$Fe(acac)_2$	2.0	0.706	
dibenzyl ether			20.0 (**c1**) 25.0 (**c2**)
1,2-hexadecanediol	10.0	2.584	
oleic acid	6.0	1.690	
oleylamine	6.0	1.606	

3.3.2 $CoFe_2O_4$ Nanorods

$CoFe_2O_4$ nanorods were synthesized by the co-precipitation route according to the synthesis of $ZnFe_2O_4$ nanorods from Kmita et al.[102] Two solutions were prepared, a precursor solution containing $CoCl_2 \cdot 6\ H_2O$ and $FeCl_3 \cdot 6\ H_2O$ in 6.25 mL H_2O and a 1.5 M NaOH solution in 6.25 mL H_2O. Simultaneously, both solutions were added dropwise (1 - 2 drops min^{-1}) to 60 mL H_2O, preheated to 50 °C under vigorous stirring. The mixture was allowed to stir at 50 °C for 6 h. 4 mL of an aqueous solution of the desired capping agent (citrate or phosphocholine) was prepared and added to the reaction mixture. After 60 min, the particles were precipitated, separated and washed with acetone in assistance of a permanent magnet.

Table 9: Reactant quantity for the synthesis of $CoFe_2O_4$ nanorods.

reagent	***n* (mmol)**	***m* (g)**
$CoCl_2 \cdot 6\ H_2O$	4.125	0.981
$FeCl_3 \cdot 6\ H_2O$	8.375	2.263
NaOH	9.4	0.374
$Na_3(cit) \cdot 2\ H_2O$ *	12.5	2.584
$Ca(phos)Cl \cdot 4\ H_2O$ *	12.5	1.690

* citrate or phosphocholine was used.

3.4 Characterization

3.4.1 SAXS Analysis

For SAXS analysis in SASView 4.2.2[103] and JScatter[95], a spherical hard sphere shape model was applied for the modelling of the nanoparticles. The standard fit range was Q = 0.2 to 5 nm^{-1}, if not mentioned. Q is the wave vector transfer, calculated as $Q = 4\pi \sin(\theta)/\lambda$, with the wavelength λ and the scattering angle 2θ. Where a bimodal size distribution is observed, two hard sphere shape models were applied. Scaling and background factor, particle radius and the polydispersity index of a lognormal size distribution were refined. Scattering length densities were set constant.

3.4.2 PDF Analysis

For the PDF refinements the scale, cell parameters, crystallite size, correlated atomic motion, oxygen positions according to symmetry constrains, occupancy of octahedral sites and thermal displacement parameters were allowed to refine. Values for the degree of inversion of spinel ferrites were obtained from crystallographic information files and were fixed for the refinement. The following crystal information files were used:

- $CoFe_2O_4$: ICSD 109044
- $MgFe_2O_4$: ICSD 155275
- $NiFe_2O_4$: AMCSD 001511
- $ZnFe_2O_4$: AMCSD 0002576
- $IONP_{Fd\text{-}3m}$: ICSD 26410
- $IONP_{P43212}$: AMCSD 0013508

The quality of each refinement is given by the goodness-of-fit value (R_W). It was calculated as follows.

$$R_w = \sqrt{\frac{\sum_{i=1}^{N} w(r_i)[G_{obs}(r_i) - G_{calc}(r_i)]^2}{\sum_{i=1}^{N} w(r_i) G_{obs}(r_i)^2}} \qquad \text{Eq. 4}$$

G_{calc} and G_{obs} are the calculated and observed PDF, respectively. $w(r_i)$ gives the weight of each data point. R_w stands for the weighted *R*-value.

4 Synthesis of Spinel Ferrite Nanoparticles

This chapter focuses on the primary step of any nanoparticle study, the synthesis. First, the polyol route for the standard synthesis of spherical spinel ferrite nanoparticles with the sum formula MFe_2O_4 (M = Co^{2+}, Mg^{2+}, Ni^{2+}, Zn^{2+}) and their final diameters are presented. A detailed discussion of their crystal structure, surface characterization and colloidal long-term stability follows in chapter 5. This synthesis and study was published in M. Eckardt, S. L. J. Thomä, M. Dulle, G. Hörner, B. Weber, S. Förster, M. Zobel, *ChemistryOpen* **2020**, *9*, 1214-1220. Then, different experimental approaches to control the size of the spherical nanoparticles and the shape are shown.

4.1 Spherical Spinel Ferrite Nanoparticles synthesized in Diethylene Glycol

The challenging tasks in wet-chemical nanoparticle synthesis are the control of the final size, polydispersity, and crystallinity. On the other hand, it is necessary to avoid Ostwald ripening and coalescence while providing stability for the produced nanoparticles. Additionally, an adjustable surface chemistry is desired for various applications. The polyol route for the synthesis of iron oxide and spinel ferrite nanoparticles enables high reaction temperatures > 200 °C due to the high boiling point of the polyols whereby highly crystalline nanoparticles can be achieved. Because of the electron donor properties of the hydroxyl groups, polyols act as both, complexing agents for the metal precursors and stabilizer for the as-built nanoparticles during the synthesis. This provides control over the reaction rate and stabilization of the nanoparticles, simultaneously. As a result, very

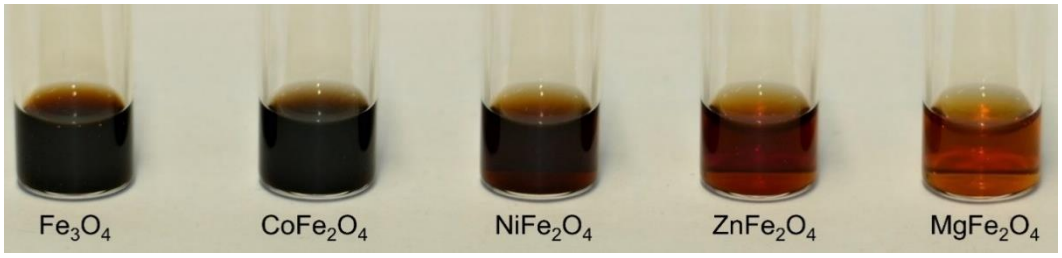

Figure 10: Picture of long-term stable citrate-stabilized spinel ferrite and iron oxide nanoparticle dispersions. *Concentration is 5 g L^{-1} in MilliQ water. IONP were synthesized by Ms. Sabrina Thomä.[7]*

uniform particle sizes and thus a low polydispersity can be achieved.[36, 104] Nevertheless, the polyol molecules only show electrostatic interactions with the nanoparticle surface and can easily be replaced by stabilizers containing more attracted moieties, e.g. carbonyls, which form a coordinative bond to the particle surface, to enhance the colloidal stability and to tailor the surface functionalization for desired applications.[69] Furthermore, the protic and polar nature of polyols allows the usage of ionic reactants, e.g. metal chlorides, to avoid contamination with other organics, e.g. acetylacetonate, which usually have a lower boiling and decomposition point. In all studies presented in this thesis, DEG (Figure 11 a) was used in the nanoparticle synthesis via the polyol route as suggested by literature.[5, 32, 47-48, 100, 105-106]

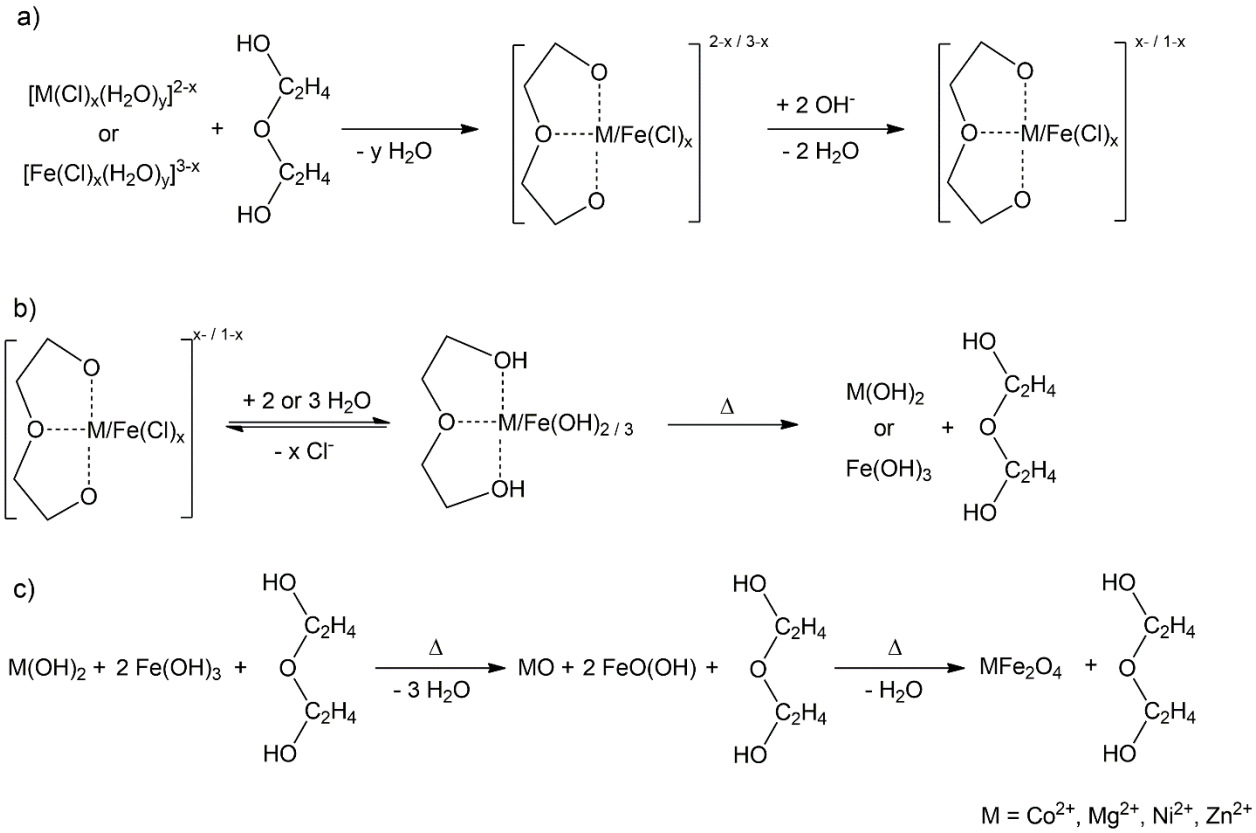

Scheme 1: Proposed mechanism of the complex formation (a), hydrolysis (b) and dehydration (c) to obtain uniform and highly crystalline nanoparticles via the polyol route in DEG. *M = Co^{2+}, Mg^{2+}, Ni^{2+} or Zn^{2+}. Modified from [5].*

According to the reaction mechanism suggested by Caruntu et al.[5], in the first step, the $[M(DEG)Cl_x]^{2-x/3-x}$ complex is formed by dissolving the metal chlorides in an alkaline DEG solution (Scheme 1 a). By raising the temperature with a constant heating rate, metal hydroxides are formed via controlled hydrolysis of the DEG complex (Scheme 1 b). Followed by dehydration of the hydroxides the MFe_2O_4 spinel ferrite structure is formed

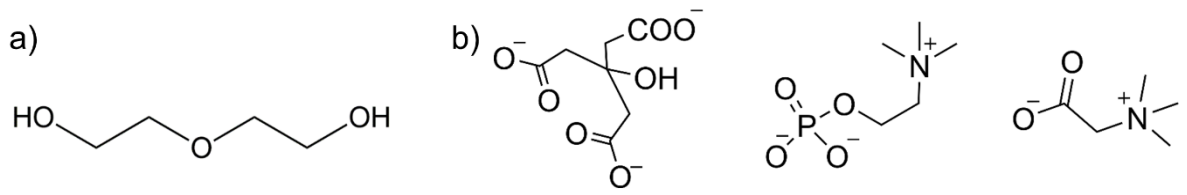

Figure 11: Valence structural formula of surface stabilizers. *a) DEG, which is used as solvent and stabilizer during the synthesis, and b) the nanoparticle stabilizer molecules, citrate (left), phosphocholine (middle) and betaine (right), used in this thesis.*

(Scheme 1 c). However, the hydration and dehydration steps are usually fast reactions. Due to the stability of the M-DEG complex and the presence of the coordinating DEG in all reaction steps, the reaction is slowed down and uniform nanoparticles can be achieved.

Dispersibility in aqueous media and high stability against Ostwald ripening and agglomeration or coalescence was then provided by an exchange of the intermediate stabilizer DEG by small, bifunctional organic acid salts like citrate, phosphocholine and betaine (Figure 10 and Figure 11). All incorporated stabilizers are bio-compatible enabling biomedical applications.

Table 10: Nanoparticle diameters obtained by DLS, TEM, and SAXS. *DLS diameter is based on number-weighted particle size distribution (converted from intensity distribution) and the PDI is calculated via cumulative frequency analysis. PDI values obtained from SAXS represent the lognormal particle size distribution. TEM and DLS particle diameters give the mean of at least two independent syntheses.*

Composition	stabilizer	d_{DLS} (nm) (PDI)	d_{TEM} (nm) (PDI)	d_{SAXS} (nm) (PDI)
$CoFe_2O_4$	citrate	4.4 (0.2)	4.6 (0.2)	3.5 (0.3)[a]
	betaine	4.1 (0.2)	3.8 (0.2)	3.5 (0.2)
	phos	4.5 (0.2)	3.8 (0.2)	4.0 (0.2)
$MgFe_2O_4$	citrate	4.7 (0.2)	3.6 (0.2)	2.8 (0.3)[b]
	betaine	5.0 (0.2)	3.0 (0.2)	2.7 (0.3)
	phos	5.6 (0.3)	3.6 (0.2)	3.5 (0.2)
$NiFe_2O_4$	citrate	4.6 (0.2)	3.6 (0.3)	2.7 (0.6)
	betaine	5.8 (0.2)	4.5 (0.2)	3.8 (0.3)
	phos	5.2 (0.2)	4.9 (0.2)	3.8 (0.3)
$ZnFe_2O_4$	citrate	5.8 (0.2)	4.8 (0.2)	5.0 (0.2)
	betaine	5.1 (0.2)	4.4 (0.2)	3.6 (0.3)
	phos	5.6 (0.3)	5.3 (0.2)	4.8 (0.2)

[a] minor second size fraction with a diameter of 6.4 (0.5) nm exists; [b] minor second size fraction with a diameter of 5.7 (0.5) nm exists.

Diameters of the freshly synthesized spinel ferrite nanoparticles were determined by DLS, SAXS and TEM. The values are summarized in Table 10. The diameters observed with the different techniques deviate slightly, due to their measurement principle. Size determination via SAXS is volume-weighted and DLS is based on intensity-weighted raw data. Both are bulk methods, where all particles contribute to the analysis. In contrast, TEM is a spot check method and equally sensitive to differently sized particles and results in a number-weighted size distribution.

TEM Analysis

TEM images are shown in Figure 12, Figure A 2 and Figure A 3 and reveal nanoparticle diameters in a range of 1 – 8 nm. The mean diameters increase for different metal ion compositions in the order M = Mg^{2+} < Co^{2+} < Ni^{2+} < Zn^{2+}. The images also indicate a highly crystalline structure as the lattice planes are clearly visible. Due to the crystallinity, the surface is facetted what results in a more ellipsoidal than spherical shape, what is highlighted in Figure 12 A by orange circles.

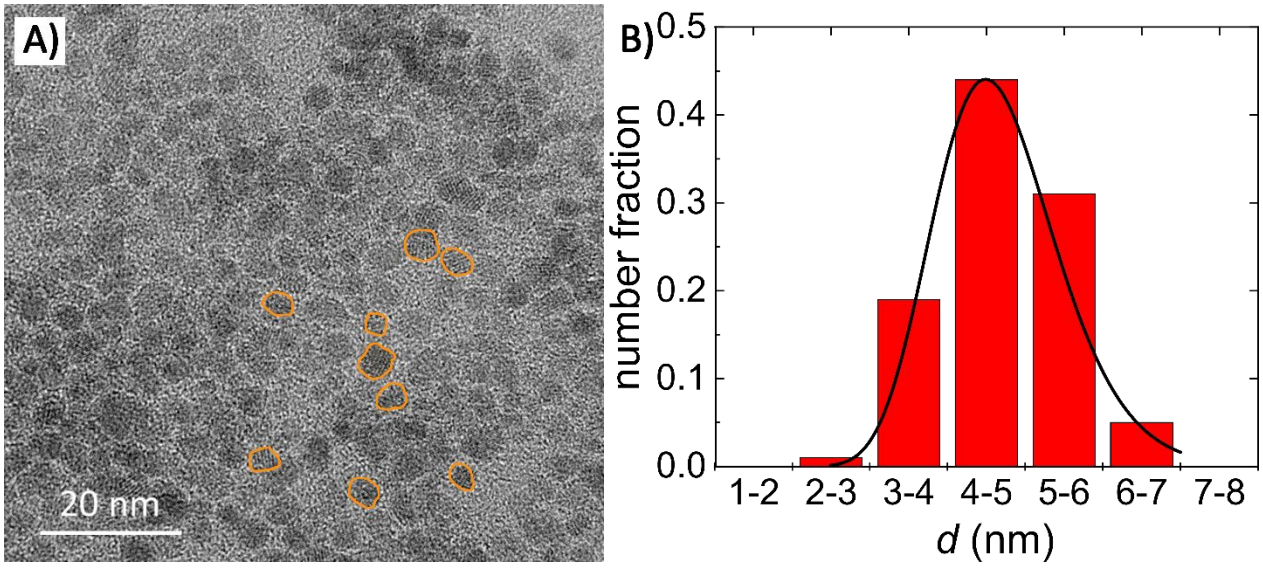

Figure 12: TEM analysis of betaine-stabilized zinc ferrite nanoparticles. *A) Representative TEM image with the nearly spherical shape highlighted in orange. B) The histogram of the size distribution with implemented lognormal fit.*

DLS Analysis

DLS yields the hydrodynamic particle diameter including a bound hydration layer, hence resulting in slightly larger particle diameters than all other techniques. The scattered intensities of the DLS raw data increase with r_{NP}^6 (r_{NP} = particle radius) making the

intensity-weighted size distribution sensitive to few large particles or agglomerates. However, the calculation of the number-weighted size distribution accounts for that dependency. The increase in particle diameter is most obvious for $MgFe_2O_4$ nanoparticles as d_{DLS} is in average 1.7 nm larger than d_{TEM}. In contrast, $CoFe_2O_4$ nanoparticles show the smallest hydration shell with an average hydration shell size of 0.3 nm. The order of mean diameters for the different metal compositions according to DLS changes to $M = Co^{2+} < Mg^{2+} < Ni^{2+} < Zn^{2+}$. The hydrodynamic diameter seems to be unaffected by the different stabilizing molecules as no linear relationship is observable. A full discussion of the hydration shells around these spinel ferrite nanoparticles follows in chapter 6.

SAXS Analysis

The SAXS signal is based on the X-ray scattering contrast of solvent and solid particle, describing the inorganic solid diameter. As it is for DLS, the scattered intensities of SAXS increase with r_{NP}^6 and the raw data is strongly affected by the existence of few larger particles or agglomerates and a number-weighted size distribution had to be calculated. Particle diameters retrieved from SAXS are significantly smaller than the ones from TEM, but indicate narrow particle size distributions with low polydispersity indices (PDI) (Figure 13). This deviation between TEM and SAXS stems from the spherical shape model used in SAXS data analysis. Yet, the shape of the spinel ferrite nanoparticles is slightly non-spherical as can be seen in the TEM image in Figure 12 A. Hence, in the SAXS refinements a higher polydispersity index in combination with a smaller average particle diameter is applied. SAXS data of citrate-functionalized magnesium and cobalt ferrite nanoparticles show an additional intensity increase for $Q < 0.4$ nm^{-1} (Figure 13 A, red and purple). As outlined above the raw data is depending on r_{NP}^6, thus, this can be ascribed to a very small fraction of agglomerates.

In conclusion, the spinel ferrite nanoparticles, stabilized by betaine, phosphocholine and citrate, show a narrow, almost monodisperse (defined as 5 % standard deviation) size distribution as conclusively evidenced by all employed techniques for almost all samples. These syntheses are highly reproducible, as each of the diameters obtained from TEM and DLS is the mean of two independent syntheses.

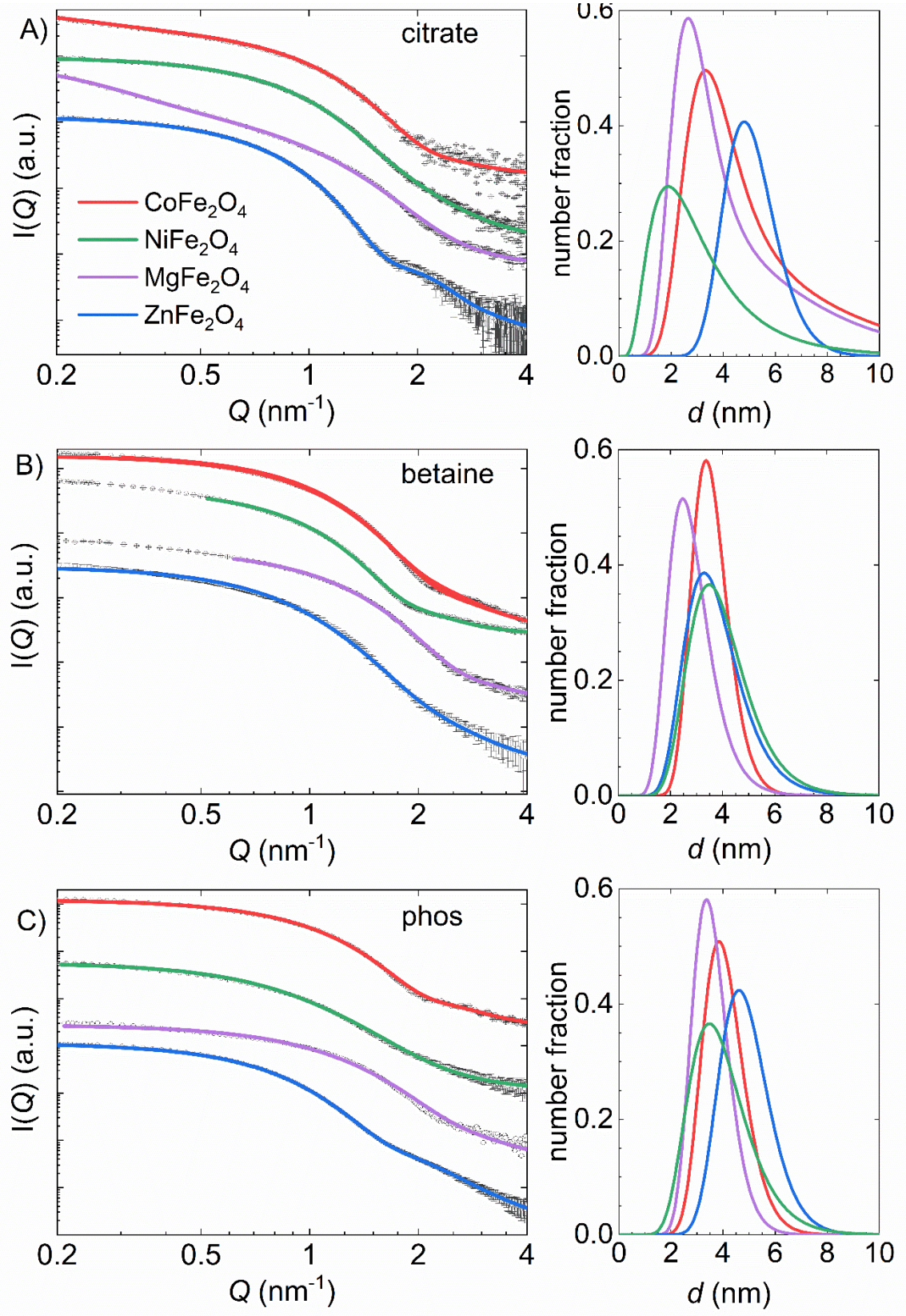

Figure 13: SAXS analysis. *Raw data and the fits of freshly synthesized A) citrate, B) betaine and c) phosphocholine stabilized spinel ferrite nanoparticle dispersions at a concentration of 5 g L^{-1} and the resulting lognormal particle size distribution in the right panel. SAXS patterns are offset for clarity. Refined particle diameters and standard deviations are given in Table 10. Calculation and values of χ^2 are shown in equation A5 and Table A 6.*

4.2 Anisotropic Cobalt Ferrite Nanoparticles

In order to study the behavior of hydration shells in dependency of the shape of nanomaterials, different published synthesis routes for obtaining rod-like and cubic spinel ferrite nanostructures were tested and analyzed. This was the main part of the bachelor thesis of Ms. Denise Schweser (University of Bayreuth).

Due to the different shapes of nanorods and nanocubes, different crystal facets in a different ratio contribute to the surface structure in comparison to spherical nanoparticles and hence affect the physicochemical properties, e.g. surface chemistry or magnetism. The control over size and shape of nanomaterials would then lead to a precise tunability of those materials for many applications.[107-109]

Through the modification of the surface chemistry, the surface structure and the interaction with the surrounding molecules, esp. in liquid dispersions, should change. The implementation of a reproducible synthesis route to obtain anisotropic nanomaterials in a similar size regime, surface stabilization and colloidal stability like the spinel ferrite nanoparticles discussed in chapter 4 and 6 will enable the direct comparison of the restructured solvent molecules at the nanoparticle surface.

4.2.1 Cubic $CoFe_2O_4$ Nanoparticles

Cubic $CoFe_2O_4$ nanoparticles were synthesized in a decomposition reaction of cobalt(II) and iron(III) acetylacetonates, oleic acid, oleylamine and 1,2-hexadecanediol in dibenzyl ether according to a modified synthesis of Zeng et al.[74] Like in the protocol of Caruntu et al.[5], the nucleation and particle growth happens at high temperature. Thus, despite the 75 °C higher end temperature of this synthesis, a similar, highly crystalline structure of the nanoparticles can be expected. In the proposed mechanism, amine, alkoxide or carboxylate Co(II) or Fe(III) complexes, are formed at 110 °C in the first reaction step. In this synthesis, these complexes are the precursor molecules. The following increase of the temperature to 295 °C is necessary for the ester and amide elimination of the precursors to the corresponding metal oxides and byproducts like acid anhydrides, esters, dialkyl ketones and the amine derivate, as well as CO_2. The metal oxides act as a monomer for the final crystal structure of $CoFe_2O_4$ and can either form new nuclei or

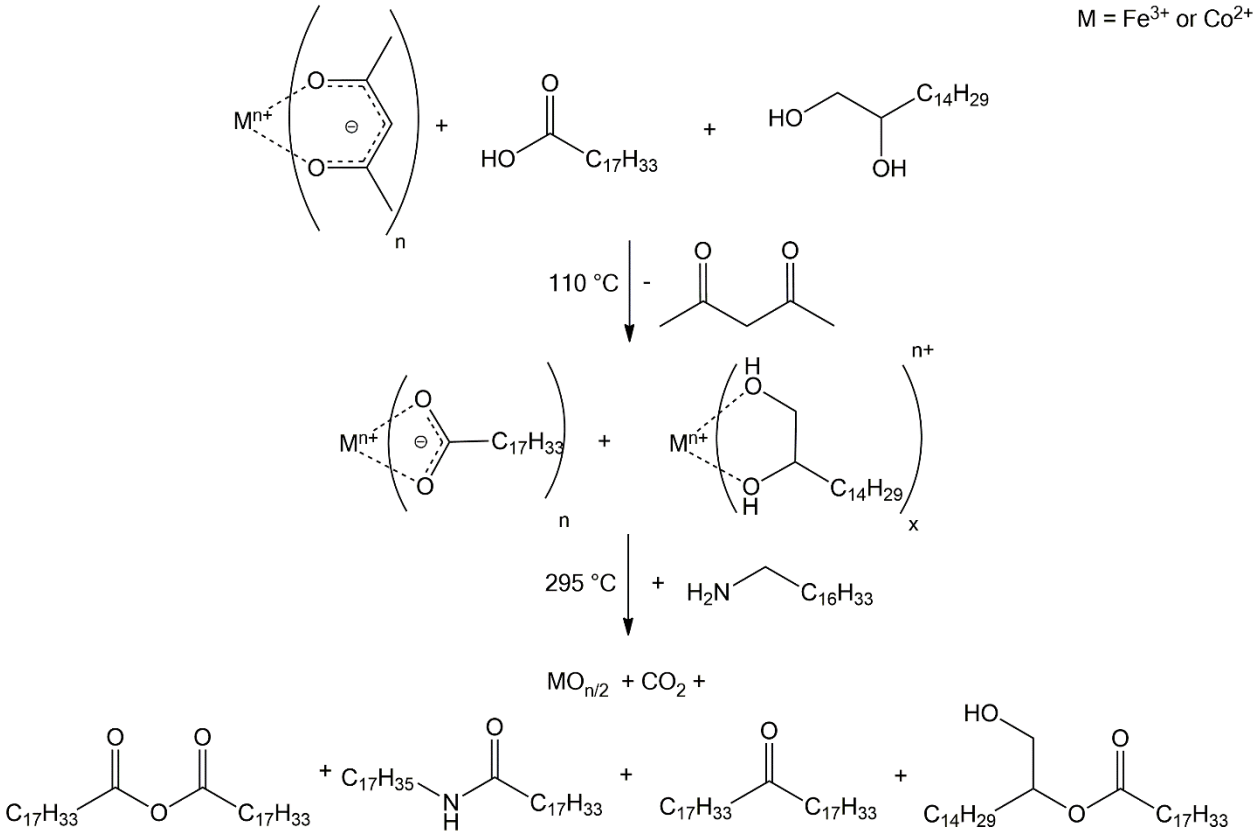

Scheme 2: Suggested mechanism of the heat up reaction to obtain cubic $CoFe_2O_4$ nanoparticles according to literature.[1-2] *M stands for Co^{2+} or Fe^{3+}. The byproducts are shown exemplarily for a wide range of possible organic compounds.*

contribute to the particle growth by the diffusion to existing nuclei (Scheme 2).[1-2] In the presented synthesis, the size of the resulting nanoparticles is controlled by the initial precursor concentration and the shape of the nanoparticles is controlled by the initial ratio of the complexing agents resp. surfactants.[74] In the following, two syntheses with different precursor concentrations (**c1**: *c* = 0.15 mM; **c2**: *c* = 0.12 mM) are shown and discussed.

Both syntheses result in highly crystalline $CoFe_2O_4$ nanoparticles without any visible crystalline side phase according to XRD analysis (Figure 14). With decreasing precursor concentration, the FWHM of the *311* reflex decreases from 0.100 to 0.086 $Å^{-1}$ for **c1** and **c2**, respectively. This indicates an increase of the overall diameter or of the degree of crystallinity.

For the analysis of particle size and shape, TEM is the characterization method of choice. Figure 15 shows selected TEM images of the samples **c1** and **c2** and the mean edge length distribution. Contrary to the literature,[74] where it is stated that uniform particle

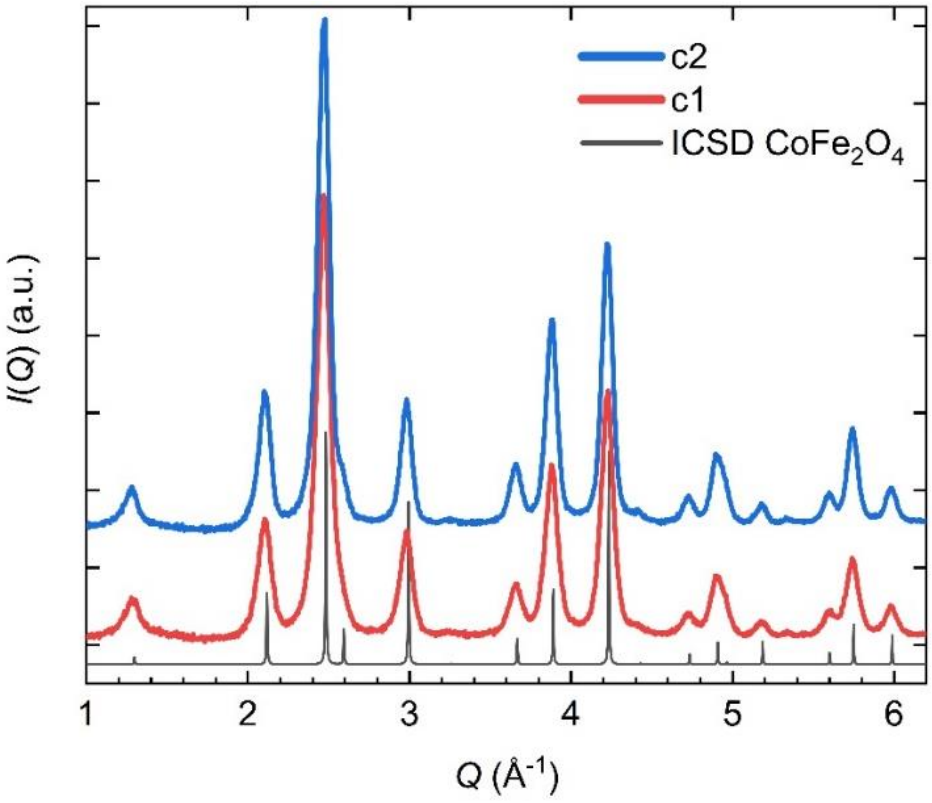

Figure 14: Background-corrected XRD patterns of dry powders of sample c1 (red, c = 0.15 mM) and c2 (blue, c = 0.12 mM) (background = empty capillary; patterns stacked for clarity). *The nanopowders are crystalline and can be indexed with the cubic spinel structure of $CoFe_2O_4$. For clarity, the theoretical XRD pattern of $CoFe_2O_4$ is shown (black).*

shapes yield from this synthesis, it is clearly visible that there are not only cubic nanoparticles but a big variety of different nanoparticle morphologies like spheres, rhombs or polyhedra. By counting the amount of cubes in a defined image area in comparison to all other shapes, the ratio of cubes to all other shapes is calculated. To extract the average edge length, only nanoparticles with a cubic shape are taken into account.

SAXS analysis (Figure 16) of sample **c2** in THF reveals that the nanoparticle dispersion is colloidally stable. The average nanoparticle diameter is 7.2 nm with a PDI of 0.24 retrieved from a lognormal size distribution. However, this refinement is based on a spherical model of the nanoparticles. Likely, this shape differences lead to the deviations of the refinement from the experimental data between Q = 1.0 – 2.0 Å^{-1}. Additional, the resulting particle diameter possesses a high uncertainty and needs to be confirmed. All values from SAXS and TEM analysis are summarized in Table 11.

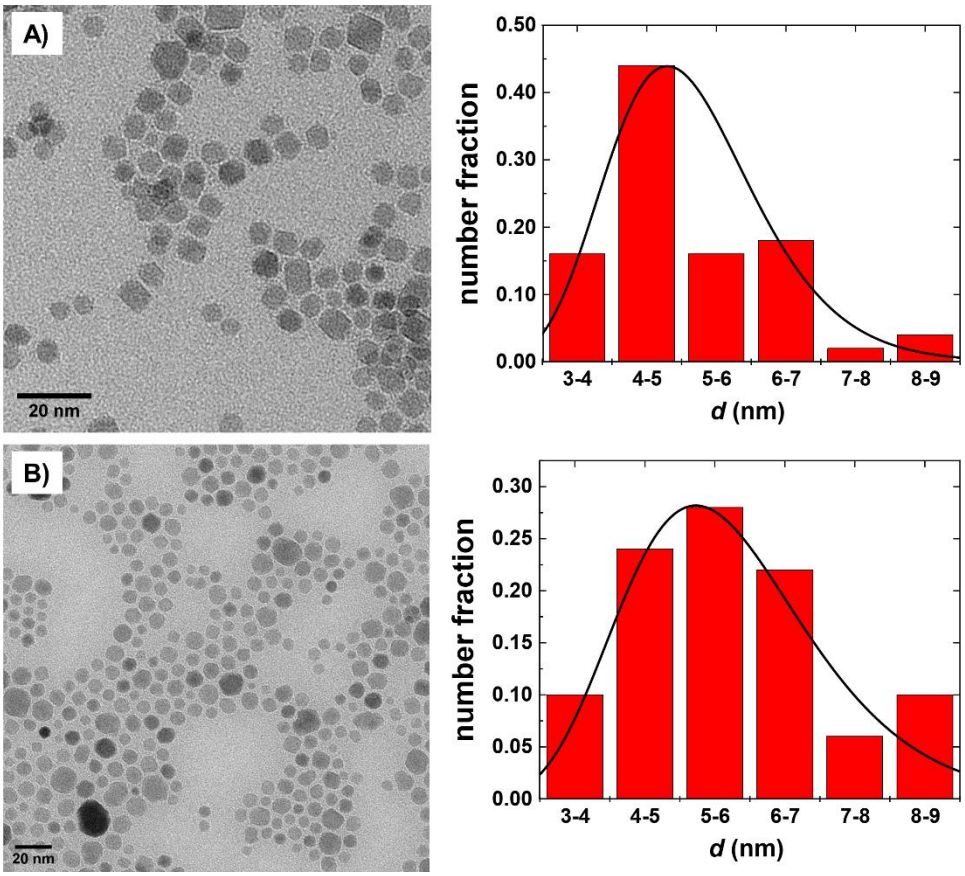

Figure 15: Selected TEM images of A) sample c1 (c = 0.15 mM) and B) sample c2 (c = 0.12 mM) and the corresponding edge length distribution of the yielded nanocubes on the right. *Mean edge lengths and the corresponding PDI were obtained by a refinement based on a lognormal size distribution*

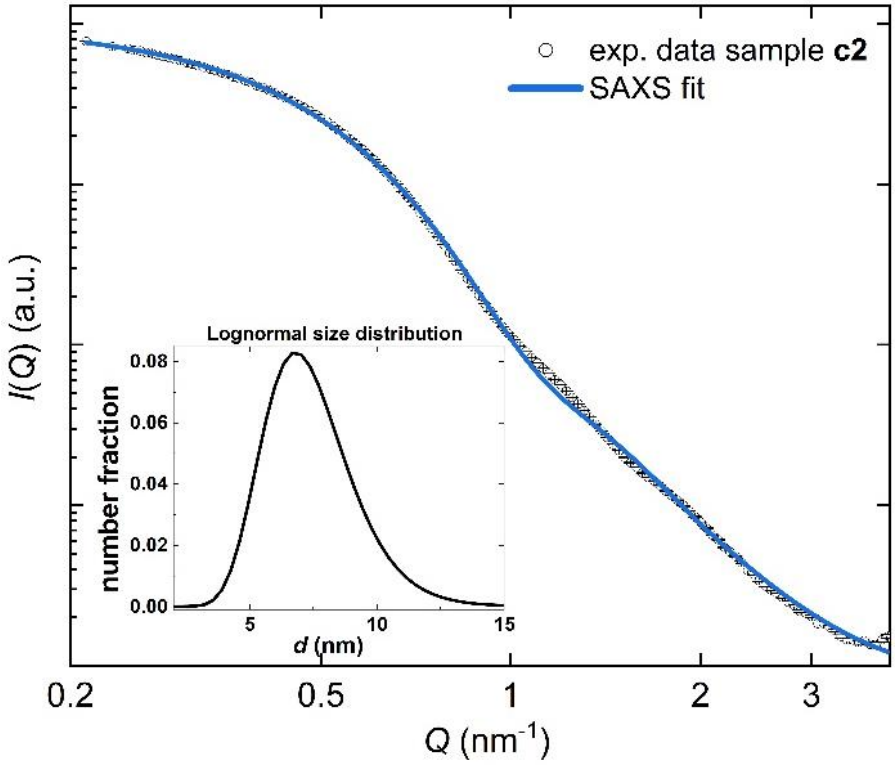

Figure 16: SAXS analysis. *Raw data and the corresponding fit of sample c2 in THF. In the inset the refined lognormal size distribution is shown.*

A maximum cube ratio to all other nanoparticle shapes of 56 % in **c1** is revealed and for the lower precursor concentration in **c2**, the ratio even decreases to 29 %. The SAXS diameter is slightly larger than the one obtained from TEM, as the TEM analysis is limited to a 2-dimensional image and only the edge length of the cubes is achievable. Whereas in SAXS, the diagonal diameter of all particles, not only the cubes, is measured and given by the refinement. According to the literature,[74] the resulting size of the nanocubes should decrease with decreasing precursor concentration and should be 12 and 8 nm for sample **c1** and **c2**, respectively. Here, both samples result in a similar value of 5.0 and 5.6 nm for the edge length.

Table 11: Summary of the edge lengths and the nanocube ratio of the samples c1 and c2 obtained from the analysis of TEM images and the size distribution of sample c2 determined by SAXS. *For the edge length, only cubic nanostructures are measured. The cube ratio is determined by counting the number of nanocubes devided by the total number of particles in a defined area.*

sample	edge length$_{TEM}$ (nm)	d_{SAXS} (nm)	nanocube ratio (%)
c1	5.0 (PDI: 0.22)		56
c2	5.6 (PDI: 0.24)	7.2 (PDI: 0.24)	29

In summary, the synthesis of cubic nanoparticles was partly successful, as only maximum 56 % of all synthesized particles in one synthesis show a cube like shape. Nevertheless, the yielded nanoparticles are highly stable as colloidal dispersions in different organic solvents, e.g. THF, toluene or hexane, and consist of crystalline $CoFe_2O_4$ without any side phase. To correlate the impact of the shape of nanoparticles onto the surrounding solvation shell in dispersions, a cube ratio of 56 % is likely not meaningful and has to be further increased. A thoroughly study of the influence of all incorporated ligands and, especially, their ratio would shed light into the process of the formation of anisotropic $CoFe_2O_4$ nanoparticles. Oleylamine should be in the focus here, as it delays the nucleation towards higher temperatures because the iron-oleylamine complex is stable at higher temperatures than the related oleic acid complex. Hence, the smaller nuclei change the kinetics of the particle growth, which is the critical step in this process. Another approach can be the use of different surfactants, like e.g. decanoic acid or potassium oleate. Also a further study including the variation of the heating rate and temperature steps will help to elucidate the growth process.[109]

4.2.2 Rod-like $CoFe_2O_4$ Nanoparticles

Other than for the cubic spinel ferrite nanoparticles, where the high temperature synthesis was successful, several published high temperature synthesis routes for rod-like nanoparticles didn't result in the desired shape. For example, the high temperature synthesis at 320 °C in 1-octadecene according to Bao et al. results in spherical $CoFe_2O_4$ nanoparticles.[110] Via the high temperature route it is intended to stick as close as possible to the synthesis parameters used for the synthesis of the spherical spinel ferrite nanoparticles, as already different surfactants and for their solubility also non-polyolic solvents are used. However, this deviation from the synthesis needs to be accepted, as the added surfactants are intended to ensure the rod-like shape. Thus, a synthesis at low temperature and in aqueous medium published by Kmita et al. led to rod-like $CoFe_2O_4$ nanoparticles.[102]

These nanorods were synthesized in a co-precipitation synthesis starting with $CoCl_2$ and $FeCl_3$. Through the addition of an aqueous NaOH solution the precipitation of $Co(OH)_2$ and $Fe(OH)_3$ is caused, which are further decomposed to the corresponding oxides CoO and Fe_2O_3. These oxides act as monomers for the final crystallization to $CoFe_2O_4$ nanorods (Scheme 3). Due to their non-functionalized surface, the resulting nanorods are not redispersible after the precipitation with acetone. Thus, in contrast to the postulated synthesis route, a post-synthetic surface modification step with citrate or phosphocholine is introduced. Like for the spherical spinel ferrite nanoparticles, they are the stabilizer of

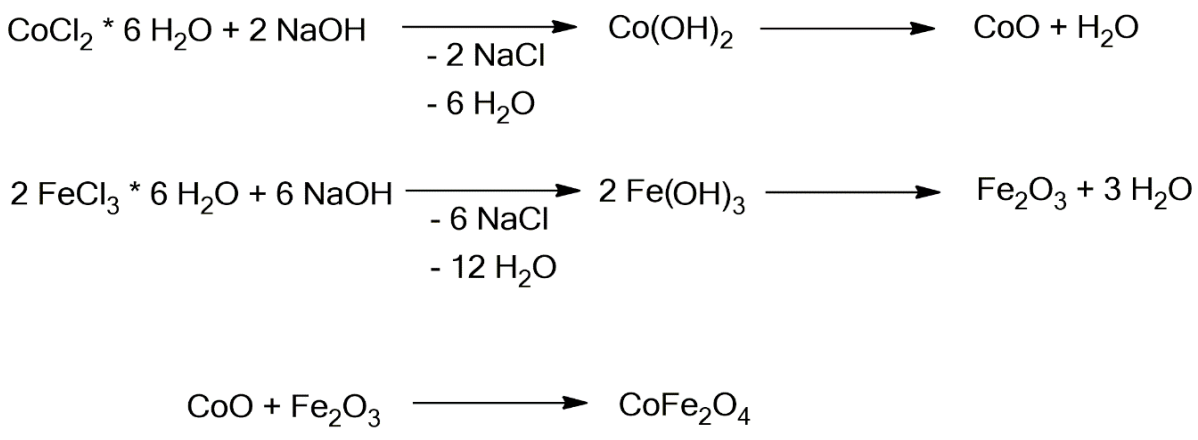

Scheme 3: Proposed mechanism of the synthesis of $CoFe_2O_4$ nanorods via the alkaline co-precipitation of Co^{2+} and Fe^{3+}.

the nanostructure against Ostwald ripening, coalescence and agglomeration. Additionally, they ensure the dispersibility of the nanorods in aqueous media due to their polarity. The resulting functionalized nanostructures are redispersible and colloidally stable. After purification, 56.3 and 111.5 mg of citrate and phosphocholine stabilized nanorods are obtained, respectively. The unstabilized nanorods weren't purified by dialysis.

The final shape of the $CoFe_2O_4$ nanostructures is analyzed by TEM analysis, first. It proofs the rod-like shape for the unstabilized (**r1**) as well as for the citrate (**r2**) and phosphocholine-stabilized (**r3**) nanorods (Table 12 and Figure 17). According to the Gaussian fits to the size distributions of the length and the diameter, the rods in **r1** are ca. 5 nm longer with a similar diameter in comparison to the nanorods in **r2** and **r3**.

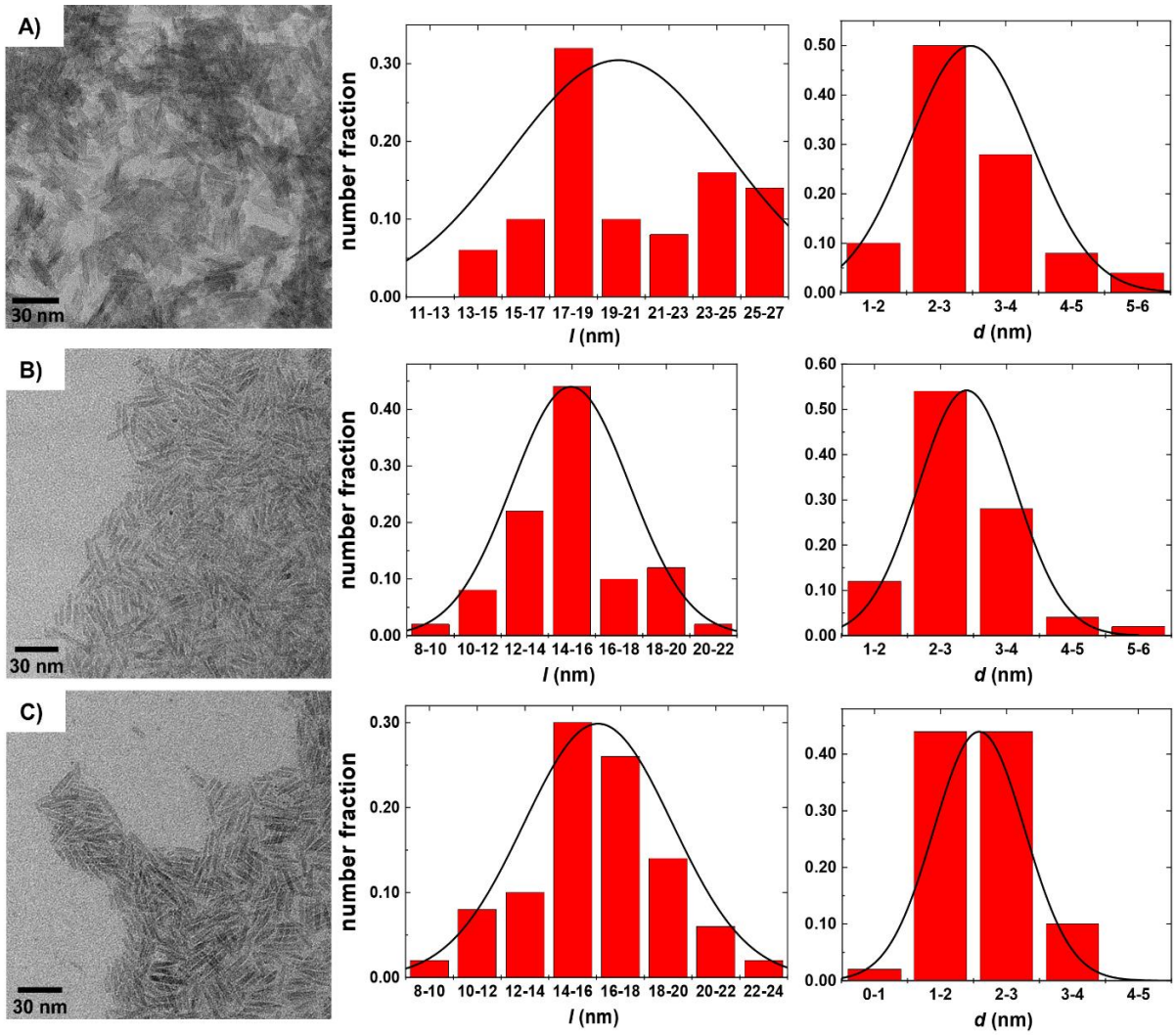

Figure 17: Selected TEM images. *A) sample r1 (unstabilized), B) sample r2 (citrate-stabilized) and C) sample c3 (phosphocholine-stabilized) and the corresponding distribution of the rod-length (l) and rod-diameter (d) of the yielded nanorods in the middle and on the right, respectively. Mean lengths, diameters and the corresponding PDI were obtained by a refinement based on a lognormal size distribution.*

Table 12: Summarized values for length (l) and diameter (d) of synthesized nanorods without the addition of stabilizing agents (r1) and with the addition of citrate (r2) and phosphocholine (r3) obtained from analysis of TEM images and SAXS refinements. *Mean diameters of length and diameter from both, TEM and SAXS analysis are obtained from a Gaussian size distribution. χ^2 values were calculated according equation 3. They are given in Table A 7.*

sample	l_{TEM} (nm) (PDI)	d_{TEM} (nm) (PDI)	l_{SAXS} (nm) (PDI)	d_{SAXS} (nm) (PDI)
r1	20.4 (0.22)	3.0 (0.31)		
r2	15.0 (0.17)	2.9 (0.26)	17.1 (0.99)	3.1 (0.62)
r3	16.1 (0.19)	2.2 (0.31)	22.0 (0.99)	1.6 (0.91)

However, as it is visible in Figure 17 A, the Gaussian fit for **r1** describes the obtained distribution barely. This may be caused by a higher tendency to agglomerate of the unstabilized nanorods. This leads to clusters during the sample preparation for TEM analysis and thus, to an increase of the error in the manually performed size analysis of the TEM images. The difference of **r1** to the samples **r2** and **r3** is clearly visible in the respective TEM images (Figure 17). While the rod structure in **r2** and **r3** is well defined, it is more difficult to obtain it visually in the **r1** TEM image.

SAXS experiments of aqueous dispersions of the citrate (**r2**) and phosphocholine (**r3**)-stabilized nanorods reveal the colloidal stability and a cylinder-like shape (Figure 18). As the unstabilized nanorods (**r1**) are not redispersible, no reliable SAXS data were achieved. As revealed by TEM analysis, a cylindrical model based on a Gaussian size distribution was applied. The refined values for length (*l*) and diameter (*d*) are given in Table 12 and graphically shown in the insets in Figure 18. For more information about the size distribution and PDI calculation refer to Table A 5, Equations A1 – A4.

For both, *l* and *d*, the resulting PDI is close to 1, indicating a very broad size distribution or also the appearance of other shapes like spheres or polyhedra. A PDI > 0.7 stands for a very broad size distribution.[111] For the citrate-stabilized nanorods (**r2**), the obtained mean value for length is slightly shorter and the diameter is slightly larger than for the phosphocholine-stabilized nanorods (**r3**). However, the quality of even the best SAXS fit for the **r2** nanorods doesn't match the experimental data points as good as the fit for **r3** (Figure 18). That suggests either a deviation of the nanorods' shape from the applied cylindrical model or the appearance of other structures like e.g. spheres.

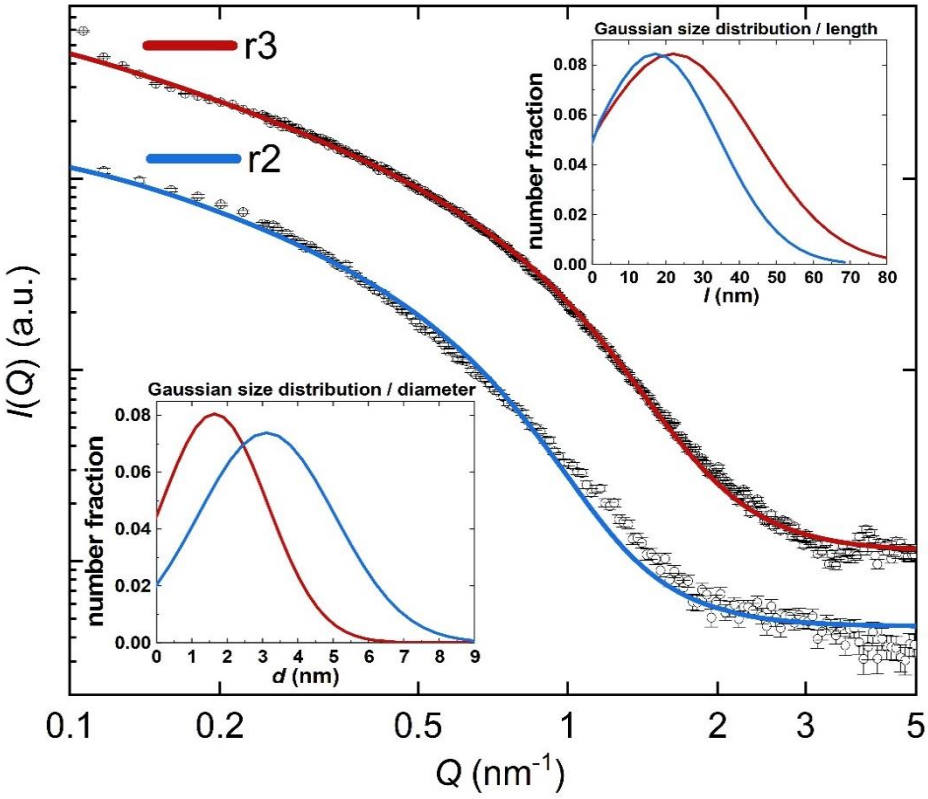

Figure 18: SAXS analysis. *Raw data and the corresponding fit of samples r2 and r3 in H_2O. In the inset the refined Gaussian size distribution is shown. As negative values for length and diameter, the size distribution is shown for d or l > 0 nm. χ^2 values were calculated according equation 3. They are given in Table A 7.*

This in combination with the very high PDI of both samples shows that the size and shape of nanostructures in the bulk may vary from the TEM result, as it is only a spot check method.

The structure of the synthesized nanorods is proved by XRD measurements (Figure 19). However, no indication for the existence of the desired cubic $CoFe_2O_4$ crystal structure is given in the XRD pattern. Instead, it can be roughly indexed by the β-phase of FeO(OH) where the Fe^{3+} ions are likely partially substituted by Co^{2+}. Also no indication for other oxide or hydroxide phases of iron or cobalt, like $Co(OH)_2$, $Fe(OH)_3$ or Fe_2O_3, are visible, although at similar conditions, α- and β-$Co(OH)_2$ can be synthesized.[112] Probably, the peaks at 0.78, 1.87, 2.45, 2.72 and 3.19 $Å^{-1}$ can also be attributed to the *00l* series of a kind of cobalt and iron layered double hydroxide (LDH) as the *Q*-position is similar to Co-LDH with intercalated CO_3^{2-} ions.[113]

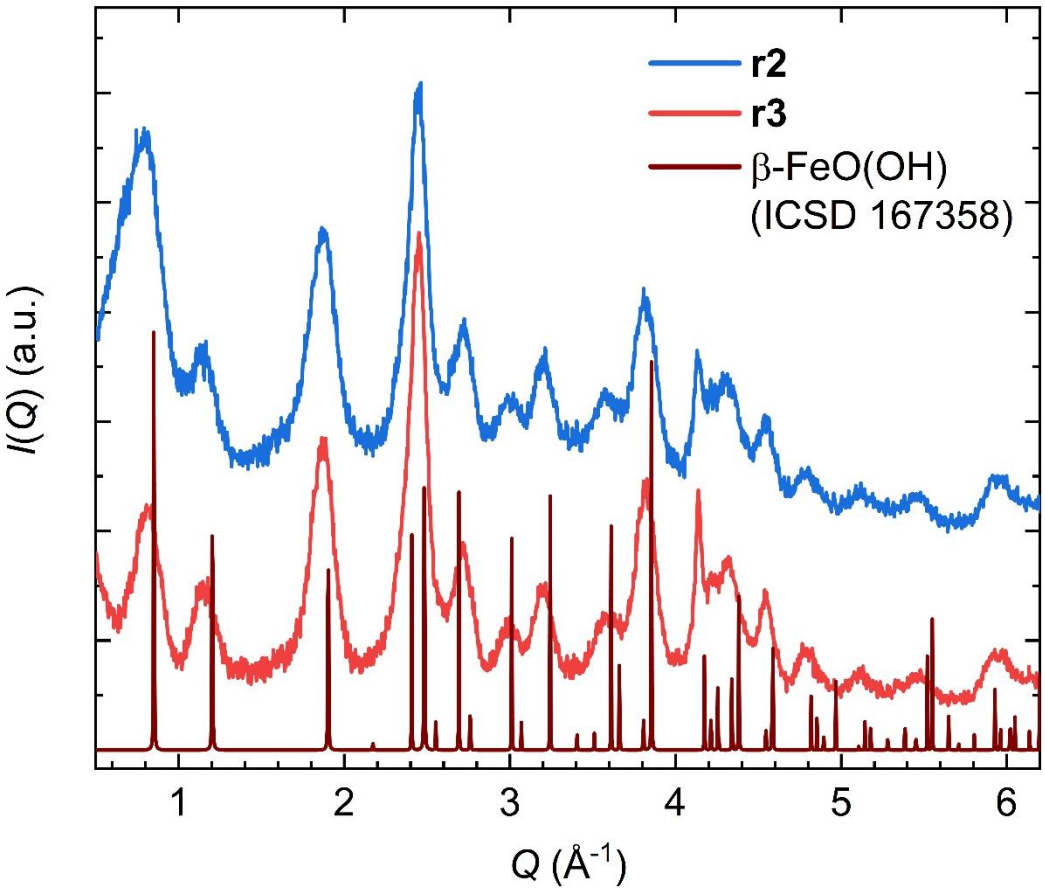

Figure 19: Background-corrected XRD patterns of dry powders of sample r2 (blue, citrate-stabilized) and r3 (red, phosphocholine-stabilized) (background = empty capillary; patterns stacked for clarity). *The nanopowders are crystalline and can be indexed roughly with the crystal structure of β-FeO(OH). Likely, Fe^{3+} is substituted by Co^{2+}, as no evidence for the existence of any other cobalt containing phase, e.g. $Co(OH)_2$, $CoFe_2O_4$ or CoO, is given. For clarity, the theoretical XRD pattern of β-FeO(OH) is shown (brown).*

A PDF refinement based on the β-FeO(OH) (Figure A 4) structure clearly reveals that the overall structure deviates from the model, as the best achieved R_W value for a single-phase refinement was 0.62 and, especially in the short-range order, pronounced peaks in the difference curve are visible at ca. 2.0, 3.5, 5.5 and 6.4 Å (Figure A 5, Table A 8). As the peaks at 2.0 and 3.5 Å and the shoulder at 3.0 Å are specific for the cubic *Fd-3m* structure of Fe_3O_4 or $CoFe_2O_4$, the addition of a second phase of $CoFe_2O_4$ with a small diameter of ca. 5 Å leads to an improvement of the fit in the short range order (Figure 20, Table A 9). However, the intensity of the distinct peaks is not reliable because the PDF model is based on a spherical shape of the nanostructures. A more complex fitting of the PDF data with a defined rod shape function would probably reduce the high R_w value (0.52).[114] Also the existence of different side phases cannot be excluded.

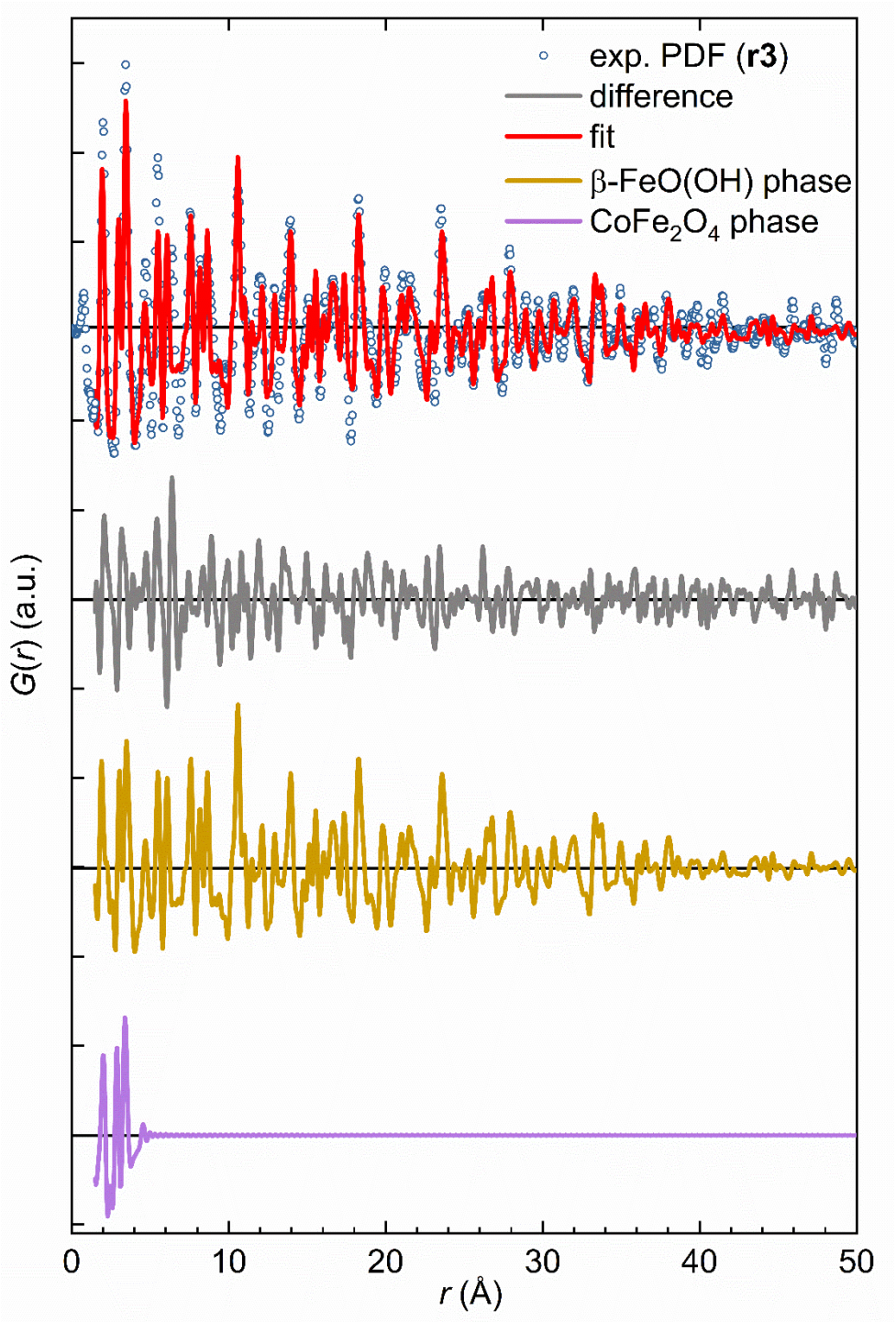

Figure 20: PDF refinement of the phosphocholine stabilized nanorods (r3) in the r-range from 1.5 to 50 Å. *Blue open circles and the red solid line correspond to measured and simulated PDFs. The grey solid line is the difference. Ochre and purple solid lines represent the contribution of the β-FeO(OH) and $CoFe_2O_4$ phases to the refinement, respectively. A summary of the refined parameters is given in Table A 9.*

In summary, it was possible to synthesize nanorods with ca. 2.5 nm in diameter and 15.0 nm in length. The colloidal stability is achieved by a post-synthetic surface functionalization with citrate or phosphocholine. However, the synthesized nanorods doesn't consist of $CoFe_2O_4$ but mainly of β-FeO(OH) and likely other hydroxide or oxide-hydroxide species. This might be caused by the low reaction temperature of 50 °C. To finally confirm the elemental composition of the nanorods, a complementary ICP-OES measurement would help. The phase transition to $CoFe_2O_4$ could be completed by an additional thermal treatment or a higher reaction temperature. However, change of the size and shape of the nanorods needs to be avoided during these steps, which makes the process rather difficult to improve. Following another strategy already implemented for iron oxide nanoparticles like the decomposition of $Fe(CO)_5$ and related cobalt carbonyls with trioctylphosphine or trioctylphosphine oxide should lead directly to $CoFe_2O_4$ nanorods.[109]

5 Structure Analysis of Spinel Ferrite Nanoparticles

The content of this chapter focuses on the structure elucidation of the spinel ferrite nanoparticles synthesized in chapter 4.1 as well as of related IONP, synthesized via the same polyol route. Finally, the phase composition of $MnFe_2O_4$ and $CoFe_2O_4$ nanoparticles synthesized via microwave-assisted and co-precipitation synthesis, respectively, are analyzed and compared to the spinel ferrite nanoparticles with respect to the different synthesis routes.

5.1 Structure and Composition of Spinel Ferrite Nanoparticles synthesized in Diethylene Glycol

For the following study, a combination of ICP-OES (inductively coupled plasma atomic emission spectroscopy), field-dependent SQUID (superconducting quantum interference device) magnetometry, X-Ray diffraction (XRD) and pair distribution function (PDF) are used and published in M. Eckardt, S. L. J. Thomä, M. Dulle, G. Hörner, B. Weber, S. Förster, M. Zobel, *ChemistryOpen* **2020**, *9*, 1214-1220.

ICP-OES

Beforehand it should be noted that the surface functionalization was achieved after nanoparticle nucleation and growth, and does not impact the particle composition. The composition of the spinel ferrite nanoparticles was investigated by ICP-OES to proof if the final Fe^{3+}/M^{2+} ratio is in accordance with the initial 2/1 ratio of the precursors. Table 13 shows that this is true for M^{2+} = Mg^{2+} and Co^{2+} nanoparticles. Their Fe^{3+}/M^{2+} ratio is between 2.0 and 2.1, except for one sample of magnesium ferrite, for which it is 2.7. For M^{2+} = Ni^{2+}, the ion composition fluctuates for all three samples between 1.7 and 2.4, resulting in an average value of 2.0. The metal ion ratio of the final zinc ferrite nanoparticles however, range between 2.9 and 3.2 and deviate strongly from the targeted 2/1 ratio. This implies a stoichiometry of $Zn_{0.73}Fe_{2.18}O_4$ and that the incorporation of the

Table 13: Molar ratios of Fe/M according to ICP-OES measurements.

nominal composition	stabilizer	molar ratio (Fe^{3+}/M^{2+})
$CoFe_2O_4$	citrate	2.1
	betaine	2.1
	phos	2.0
$ZnFe_2O_4$	citrate	2.9
	betaine	3.2
	phos	2.9
$MgFe_2O_4$	citrate	2.0
	betaine	2.7
	phos	2.1
$NiFe_2O_4$	citrate	2.4
	betaine	1.7
	phos	2.0

Zn^{2+} cation into the spinel crystal structure isn't preferential in comparison to Co^{2+}, Mg^{2+} and Ni^{2+}. The fact that the molar amount of oxygen is not accessible by ICP-OES the calculated stoichiometry may not be correct and vacancies exist in the crystal structure. This would completely coincide with investigations by Kodama et al. on the incorporation of Zn^{2+} ions into the spinel ferrite crystal structure: even a 12-fold excess of Zn^{2+} to Fe^{3+} ions in the precursor solution results in a high number of Zn^{2+} vacancies and thus yields 27 % maghemite.[115] As mentioned in chapter 2.1, LFT and the ion radii define the incorporation as well as the ion occupation on the respective sites. LFT doesn't give a hint here. Neither the high-spin d^5 of Fe^{3+} nor the d^{10} electron configuration of Zn^{2+} is favored in comparison to the other on both, OL and TL sites. The ion radii of six-fold coordinated Zn^{2+} ions is 74 pm,[116] which is 9 pm more than for the six-fold coordinated high-spin Fe^{3+}.[117] This is equivalent to a difference of 14 % with respect to the Fe^{3+}. According to the literature, ions with an ion radius difference lower than 18 % with respect to six-fold

coordinated high-spin Fe^{3+} should be tolerated in the spinel structure.[117-118] However, for nanoparticles and their less ordered crystal structure this boundary may be softened.

SQUID

Exemplarily for all synthesized nanoparticles, the magnetic behavior of the citrate stabilized spinel ferrite nanoparticles are characterized via field-dependent SQUID magnetometry. Data acquisition and fitting was performed by Mr. Gerald Hörner (University of Bayreuth). Regardless of the divalent metal ion, Figure 21 proofs superparamagnetism for all nanoparticle compositions, as no hysteresis around $|H| = 0$ at $T = 300$ K is visible. The slope of all curves is still positive for $|H| > 30.000$ Oe indicating that the final value of the saturation magnetization (M_S) is not reached at this magnetic field strength. However, M_S can be calculated by fitting the data with the Langevin equation[119]

$$M / M_S = \coth(\alpha) - 1 / \alpha; \text{ with } \alpha = \mu_{part} \times H / k_B \times T \qquad \text{Eq. 5}$$

with the Boltzmann constant k_B and magnetizing field H. μ_{part} denotes the (formal) magnetic moment of a single nanoparticle. The data and fits are shown in Figure 21 and the obtained values for M_S are summarized in Table 14. The saturation magnetization

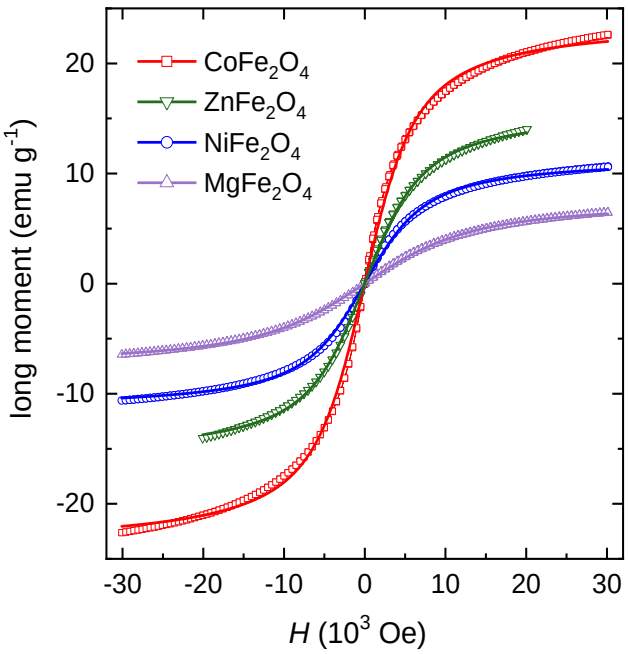

Figure 21: Field-dependent SQUID magnetometry measurements of citrate stabilized spinel ferrite nanoparticles (symbols) and the corresponding Langevin fit (lines).

decreases along the series Co^{2+} > Ni^{2+} > Zn^{2+} > Mg^{2+}. This is contrary to M_S values published for bulk spinel ferrite materials (see Table 14). The expected series would have been Co^{2+} > Zn^{2+} > Ni^{2+} > Mg^{2+}. So, the lowest (Mg^{2+}) and the highest (Co^{2+}) values for M_S match the expectations from literature. Only the order of Zn^{2+} and Ni^{2+} is changed. As M_S increases with increasing particle diameter,[49] the lower M_S for $ZnFe_2O_4$ nanoparticles is even more unexpected as they have the largest diameter of the analyzed nanoparticles, here. This may be caused by the deviation of the Fe/Zn ratio from the nominal composition revealed by ICP-OES, which may lead to a decrease of M_S due to unoccupied metal sites in the crystal structure. The detailed evaluation of the magnetic structure and the influence of the composition and inversion onto M_S will lead to a deeper understanding but is beyond the scope of this study.

Table 14: Fitted values of M_S for citrate stabilized spinel ferrite nanoparticles and references for bulk materials.

nominal composition	**stabilizer**	**M_S (emu g^{-1})**	**M_S^{bulk} (emu g^{-1})**
$CoFe_2O_4$	citrate	24.0	80.8[120]
$ZnFe_2O_4$	citrate	11.5	52.4[121]
$MgFe_2O_4$	citrate	7.7	33.4[122]
$NiFe_2O_4$	citrate	16.0	47.5[123]

XRD

XRD measurements performed on all synthesized spinel ferrite nanoparticles with the STOE STADI P are shown in Figure 22 and confirm the high crystallinity of all spinel ferrite nanoparticles, which results from the high temperatures maintained during synthesis. The grade of crystallinity varies for the different compositions of the spinel ferrite nanoparticles. This is shown by the different values for the full-width-at-half-maximum (FWHM, see Table A 10). $MgFe_2O_4$ nanoparticles have the largest and $ZnFe_2O_4$ nanoparticles the lowest broadening, which is also proportional to the particle diameter (Table 10). The peak positions in Q vary very slightly for the different spinel compositions accounting for the slightly different lattice parameter, which is $ZnFe_2O_4$ > $MgFe_2O_4$ ≈ $CoFe_2O_4$ > $NiFe_2O_4$.

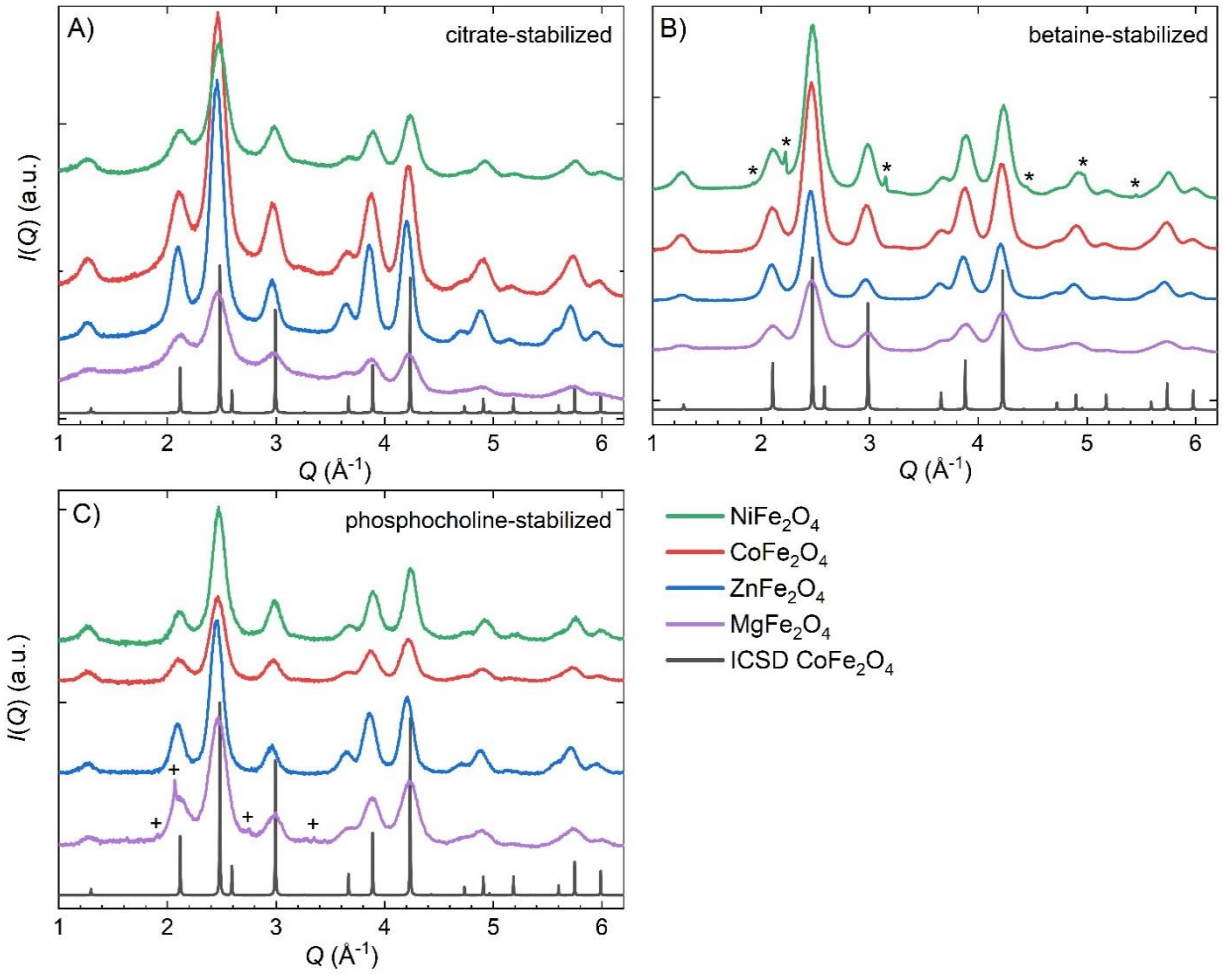

Figure 22: Background-corrected XRD patterns of dry powders of A) citrate, B) betaine and C) phosphocholine-stabilized ferrite nanoparticles (background = empty capillary; patterns stacked for clarity). *Data were collected with a STOE STADI P. All nanopowders are crystalline and can be indexed with the cubic spinel structure Fd-3m. Different heights and FWHM of Bragg reflections stem from different nanoparticle diameters. Here, for clarity, the theoretical XRD pattern of $CoFe_2O_4$ is shown exemplarily; the lattice parameters of the different spinels vary slightly. In pattern B) for $NiFe_2O_4$, few small sharp peaks (stars) at Q = 1.92, 2.23, 3.15, 4,45, 4.98 and 5.45 $Å^{-1}$ stem from betaine monohydrate. In pattern C) for $MgFe_2O_4$, few small sharp peaks (cross) at Q = 1.91, 2.07, 2.75 and 3.35 $Å^{-1}$ stem from phosphocholine. Both ligands were used in excess.*

The XRD patterns can be all indexed with the cubic spinel structure *Fd-3m*, with a small shift to lower *Q* values, indicating slightly larger unit cells in comparison to the bulk material. Despite the deviation of the zinc to iron ratio in the zinc ferrite nanoparticles, no side phases could be detected in its XRD patterns (all blue patterns in Figure 22). Side phases are only visible in betaine-stabilized $NiFe_2O_4$ and phosphocholine-stabilized $MgFe_2O_4$ nanoparticles (green in Figure 22 B and purple in Figure 22 C, respectively). They can be attributed to the respective stabilizer, betaine monohydrate and phosphocholine monohydrate.

PDF

The PDF raw data was collected on a STOE STADI P Mythen 4k, a dedicated PDF laboratory instrument. For instrumental parameters see Table A 2. Measurement time was 14 h for each sample. The Fourier transformation of the collected XRD data into real space was performed with PDFgui.[99] Q_{min} and Q_{max} were 0.4 and 20.4 $Å^{-1}$, respectively.

The PDF refinements of the spinel ferrite nanoparticles were carried out with DiffPy-CMI[98] in a fit range of 1.7 to 50 Å. They are based on the cubic spinel structure *Fd-3m* and describe the experimental data well (Figure 23 for betaine-stabilized and Figure A 6 and Figure A 7 for citrate and phosphocholine-stabilized spinel ferrite nanoparticles, respectively). The refined fit parameters are summarized in Table 15. The good quality of the refinements is also shown by the goodness-of-fit values R_W. Its calculation is described in Equation 4. R_W values are between 0.15 and 0.19 for betaine-stabilized ferrites – except for $NiFe_2O_4$ due to a betaine side phase (see Figure 26 D and Table 15), which is also visible in the XRD pattern (green in Figure 22 B). Refinements of the citrate stabilized particles result in R_W values of 0.11 to 0.22 – except for $MgFe_2O_4$ due to a citrate side phase (Table A 11) – and phosphocholine stabilized particles yield R_W values of 0.12 to 0.21 (Table A 12). For all three stabilizers, magnesium ferrites have the highest R_W values, i.e. lowest fit qualities, throughout.

Table 15: Refined parameters for PDF refinements of betaine-stabilized spinel ferrite nanoparticles including the parameter of octahedral occupancy Occ_{oct} (see Figure 29).

parameter	$CoFe_2O_4$	$ZnFe_2O_4$	$NiFe_2O_4$	$MgFe_2O_4$
***a* = *b* = *c* (Å) (start)**	8.394	8.442	8.347	8.397
***a* = *b* = *c* (Å)**	8.407	8.410	8.368	8.390
crystallite size (Å)	43	47	49	34
$U_{iso,\ Co/Zn/Ni/Mg}$ **(Å²)**	0.009	0.010	0.006	0.021
$U_{iso,Fe}$ **(Å²)**	0.009	0.010	0.009	0.007
$U_{iso,O}$ **(Å²)**	0.022	0.029	0.016	0.029
z(O)	- 0.631	- 0.632	- 0.631	- 0.631
Occ_{oct}	0.99	0.84	1.00	0.73
R_w	0.15	0.16	0.29	0.19

From the PDF refinements, a spherical crystallite size assumption can be extracted, where the peak heights in the experimental PDF decay to zero. The average crystallite size of each composition increases in the order $MgFe_2O_4$, $CoFe_2O_4$, $NiFe_2O_4$, $ZnFe_2O_4$ and, thus, follows the same trend as the TEM analysis (chapter 4.1).

This is another proof for the high crystallinity of the synthesized spinel ferrite nanoparticles. As $MgFe_2O_4$ are the smallest nanoparticles, along with the higher amount of defects and higher disorder the higher R_W can be explained.

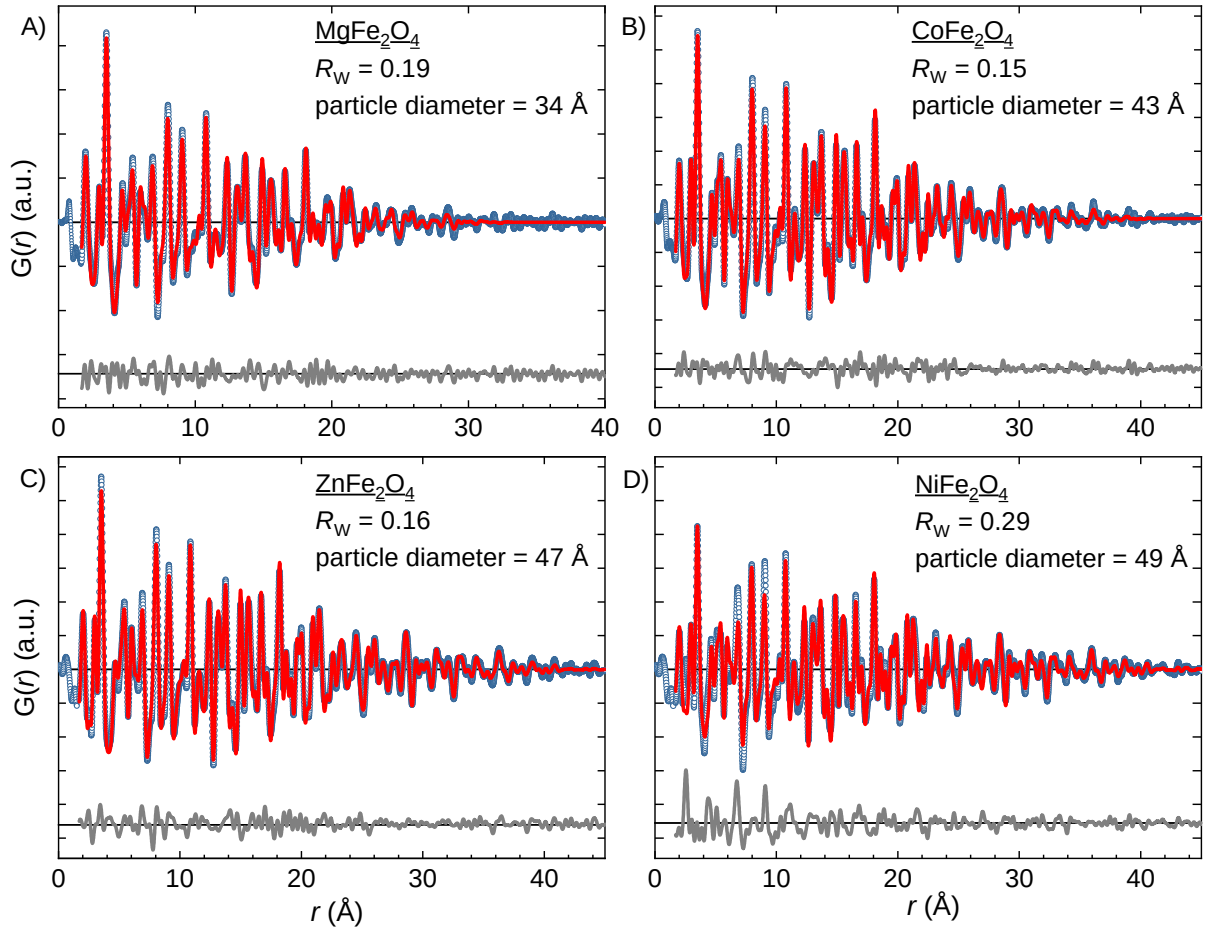

Figure 23: PDF refinements of betaine-stabilized A) magnesium, B) cobalt, C) zinc and D) nickel ferrite nanoparticles over r-ranges of 1.7 to 40 Å and 1.7 to 45 Å, respectively.
Blue open circles and red solid lines correspond to measured and simulated PDFs. Grey solid lines are the differences, in offset for clarity. All but the nickel ferrite refinements show good agreement with the experimental data (low R_w-values, no remaining structural signal in difference curve). In the nickel ferrite nanoparticle refinement, the structural residue can be ascribed to the betaine side phase. For values of fit parameters see Table 15.

As expected, the refined unit cell parameters *a* differ from the start values obtained from the cif-files, which were postulated on bulk materials. This deviation is not consistent for the four different compositions. While the unit cell parameters of nanostructured $CoFe_2O_4$ and $MgFe_2O_4$ are similar to the bulk values with a deviation of 0.007 and -0.008 Å, respectively, the unit cells for nanostructured $NiFe_2O_4$ and $ZnFe_2O_4$ are notably bigger (0.022 Å for $NiFe_2O_4$) or smaller (-0.024 Å for $ZnFe_2O_4$) than in the bulk.

The refinements reveal a deviation in the local structure up to 5 Å (Figure 24 A). Especially, the intensity of the peaks at $r \approx 3.0$ Å and $r \approx 3.5$ Å, which represent the distance between occupied octahedral sites and between occupied octahedral and tetrahedral sites, respectively, doesn't match the experimental data sufficiently. A similar phenomenon was discovered by Cooper et al. during the PDF refinement of iron oxide nanoparticles.[6] They introduced a parameter for the occupancy of the octahedral sites, which resulted in a better description of the experimental data by the refinements and made them able to calculate the ratio of maghemite to magnetite. As defects, such as unoccupied metal sites, can be expected in nanostructured materials, this approach is

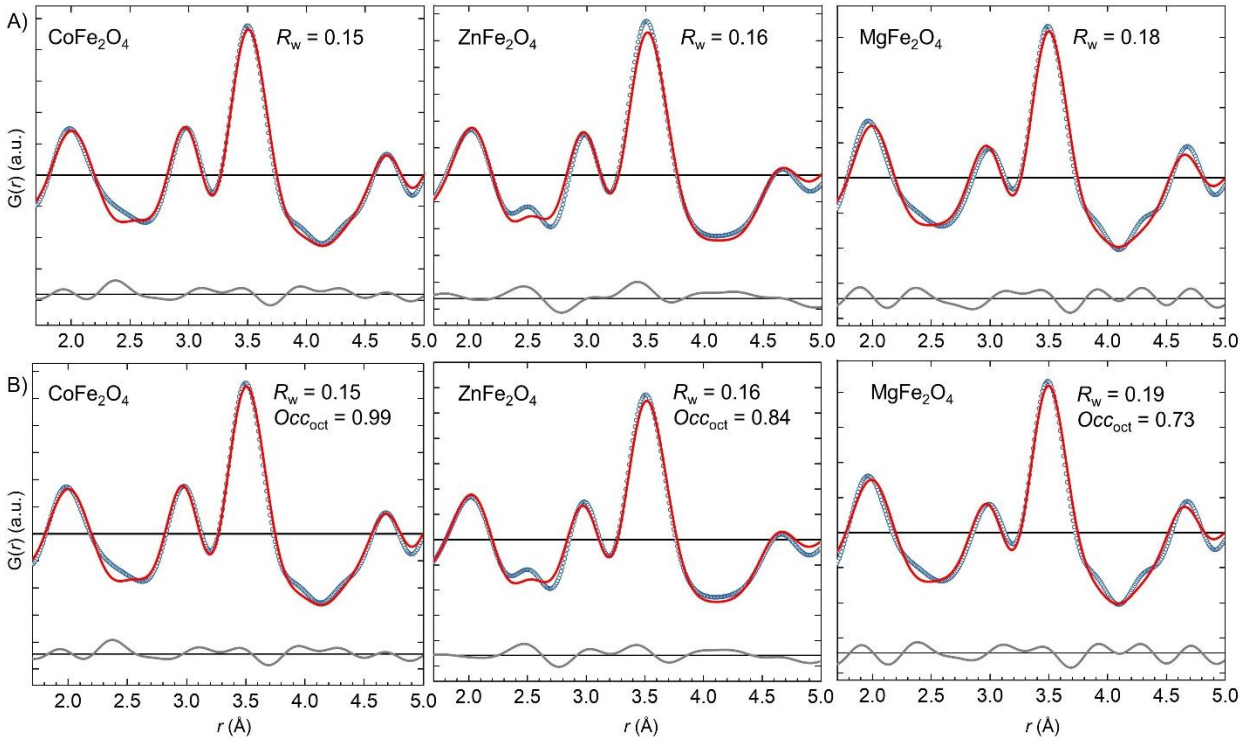

Figure 24: PDF refinements of betaine-stabilized cobalt, zinc and magnesium ferrite nanoparticles A) without and B) with the fit parameter Occ_{oct}. *The r-range from 1.7 to 5.0 Å is enlarged to enable a detailed view onto the refinement of the local structure up to 5 Å. Fit ranges are 1.7 - 45 Å for zinc and cobalt ferrites, and 1.7 - 40 Å for magnesium ferrites.*

transferred to the here described spinel ferrite nanoparticles. Thus, a parameter (Occ_{oct}), which accounts for possible vacancies on the octahedral cation positions, is introduced in the refinements. The influence of this parameter can be illustrated by the comparison of the short range order (r = 1.7 - 5.0 Å) of refinements with and without Occ_{oct} (Figure 24 A and B). Due to the side phase in nickel ferrite nanoparticles, this refinement is omitted here. For magnesium and zinc ferrite nanoparticles, the introduction of the Occ_{oct} parameter results in a better description of the experimental data. In the final fits, reduced octahedral occupancies of 0.73 and 0.84 for magnesium and zinc are uncovered, respectively. However, the R_W over the entire fit range is not improved. This shows that the vacancies are randomly distributed and thus, don't affect the average structure. For zinc ferrite nanoparticles, this observation is in accordance with ICP-OES results (Table 13), whereas for magnesium ferrite nanoparticles, the octahedral vacancies can be attributed to the overall lower degree of crystallinity. Furthermore, the initial overall fit quality without Occ_{oct} for magnesium (R_W = 0.18) and zinc ferrite (R_W = 0.16) nanoparticles was already very good for nanoparticle refinements. Residual features in the difference curve stem rather from the higher disorder or other structural effects, not described by the spherical attenuated model. However, for cobalt ferrite nanoparticles, Occ_{oct} isn't refined and sticks to 1, indicating fully occupied tetrahedral and octahedral sites. Structural changes due to oxidation published for iron oxide nanoparticles,[6] can be ruled out, as the bivalent metal ions $M^{2+} \neq Fe^{2+}$ are stable against oxidation in air.

Additional to the parameter Occ_{Oct}, the introduction of a parameter accounting for vacancies on tetrahedral sites was tested according to Cooper et al.[6] However, in none of the refinements it drops below the initial value of 1, indicating that vacancies exist predominantly on octahedral sites. Thus, the occupancy of the tetrahedral sites wasn't refined in the final fits.

Each nanoparticle synthesis was carried out three times to enable the surface modification with three different stabilizers. For each composition, all three synthesis show similar structural parameters like particle size, Occ_{Oct}, and the lattice parameter. This proofs that the nanoparticle structure is unaffected by post-synthetic stabilization and the high reproducibility of the polyol synthesis in DEG.

5.2 Structure of Iron Oxide Nanoparticles – Tetragonal or Cubic

In addition to the presented spinel ferrite nanoparticles, iron oxide nanoparticles (IONP) were synthesized via the same polyol synthesis route by Ms. Sabrina Thomä (University of Bayreuth), starting with Fe^{2+} and Fe^{3+} as precursors. As part of a cooperation, the PDF analysis of the IONPs is also part of this thesis. A representing TEM image of the phosphocholine-stabilized IONPs are shown in Figure A 9.

Magnetite and maghemite also belong to the class of spinel ferrites. In contrast to the presented spinel ferrite nanoparticles, where M^{2+} doesn't tend to oxidize, Fe^{2+} in magnetite readily undergoes oxidation to Fe^{3+} in air. By this oxidation, vacancies on octahedral sites are generated, leading to a stoichiometry of the synthesized IONP between magnetite (Fe_3O_4) and maghemite (γ-Fe_2O_3), which is a defect structure of magnetite. The resulting sum formula can be denoted as $[\mathrm{Fe}^{3+}]_{\mathrm{T}}[\mathrm{Fe}^{2+}_{1-3\delta}\mathrm{Fe}^{3+}_{1+2\delta}\square_{\delta}]_{\mathrm{O}}\mathrm{O}_4$, where the brackets marked with "T" and "O" represent tetrahedral and octahedral sites, respectively, δ is the total amount of vacancies in the spinel structure and the empty square (□) the visualization of those vacancies.[124] According to the LFSE theory, vacancies on tetrahedral sites are not favored, as Fe^{2+} in d^6 high-spin state prefers an octahedral coordination. However, this accounts mainly for ordered three dimensional crystals and less for more disordered nanocrystals.

According to Cooper et al.[6], the number of these octahedral vacancies (δ) can be quantified via PDF refinements by the intensity ratio of the 3.0 and 3.5 Å peaks. With this, the magnetite/maghemite phase ratio can be determined. Here, the δ parameter replaces the Occ_{oct}, introduced for the refinements of spinel ferrite nanoparticles. As initially pointed out in chapter 2.1.4, different space groups are proposed for maghemite and mixtures of maghemite and magnetite, such as tetragonal $P4_332$, $P4_32_12$ and $P4_12_12$ or a defect structure of cubic $Fd\text{-}3m$.[85] In the following, the PDF data of IONP are refined with models based on the cubic $Fd\text{-}3m$ and the tetragonal $P4_32_12$ model and the results are compared. Representative refinements on betaine-stabilized 5 nm IONP are shown in Figure 25 and the corresponding parameters are shown in Table 16. Refinements on phosphocholine and citrate-stabilized IONP (d = 3.5 nm) are shown in Figure A 8 and Figure A 10 and the

refined parameters are summarized in Table A 13. The size deviation is not stabilizer dependent but derives from slightly different particle size distributions of different syntheses.

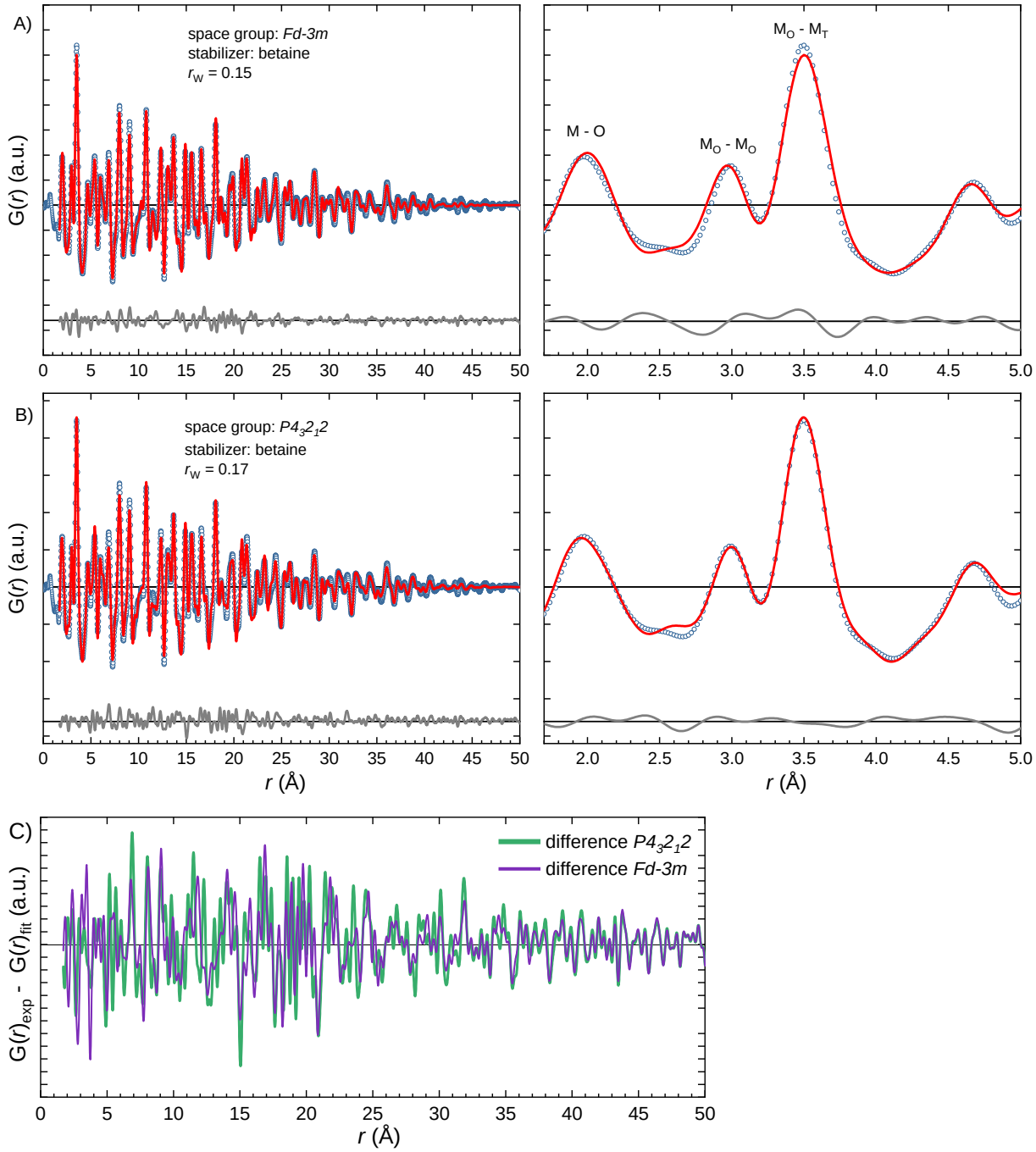

Figure 25: PDF refinements of betaine-stabilized IONP based on the space group Fd-3m (A) and $P4_32_12$ (B) over a r-range from 0 – 50 Å (left). The corresponding r-range from 1.7 – 5.0 Å is magnified on the right. The difference curves of both fits are compared in C).

Blue open circles and red solid lines correspond to measured and simulated PDFs. Grey solid lines are the differences, in offset for clarity. In the short range, the PDF peaks are assigned to the corresponding pair of atoms. For values of fit parameters see Table 16.

Table 16: Refined parameters for PDF fits of IONPs using the space group Fd-3m and $P4_32_12$. *Graphs are shown in Figure 25.*

sample	**IONP - betaine**	
model space group	*Fd-3m*	*$P4_32_12$*
a=b (Å) start	8.397	8.337
c (Å) start	8.397	8.322
a=b (Å)	8.390	8.364
c (Å)	8.390	8.435
crystallite size (Å)	50	52
$U_{iso,Fe}$ (Å²)	0.010	0.005
$U_{iso,O}$ (Å²)	0.025	0.007
O_z	- 0.629	
O1_x		0.617
O1_y		0.855
O1_z		- 0.005
O2_x		0.085
O2_y		0.365
O2_z		- 0.006
O3_x		0.122
O3_y		0.875
O3_z		- 0.015
O4_x		0.383
O4_y		0.636
O4_z		- 0.001
δ*	0.33	0.24
***magnetite phase ratio**[#]*	0 %	28 %
R_w	0.15	0.17

* for the *Fd-3m model,* δ derives from the occupation of the octahedral site Occ_{oct} (Wyckoff position: *16d*). For the $P4_32_12$ model, δ derives from the occupation of the Fe(4) site (Wyckoff position: *4a*). For calculation see equations A6 and A7.

[#] for detailed calculation see equation A8.

Comparison of the cubic *Fd-3m* based and the tetragonal $P4_32_12$ based refinements clearly reveals differences in the short range (r = 1.7 – 5.0 Å) and the middle range (r = 10.0 – 35.0 Å) order. Whereas in the short range, the fit with *Fd-3m* space group shows some deviations in the peak position (M – O, M_O – M_O) and the peak height (M_O – M_T), the fit with $P4_32_12$ space group describes the experimental data better. However, as Figure 25 C clearly reveals, the tetragonal fit significantly deviates in the range r = 10 – 25 Å more from the experimental data than the cubic fit. This leads to an improved quality of fit for the cubic model, which is reflected by the R_W values (cubic: 0.15, tetragonal: 0.17). In addition, the refined δ and thus the magnetite phase ratio differs in both cases. The cubic model yields in a magnetite content of 0 % and the tetragonal model in 28 %. Likely, these deviations derive from the fact that in the tetragonal refinement more parameters (6 to 18), especially the oxygen positions in the unit cell and the length of the c-axis, are refined independently. Consequently, the short-range atom distances are well described by the tetragonal refinement and δ only accounts for vacancies at the octahedral sites, given by the ratio of the PDF peaks at 3.0 and 3.5 Å. However, due to the higher symmetry in the cubic model, there are less parameters and stricter constraints for the refinement. For that reason, as already discussed above, the atom distances at 2.0, 3.0 and 3.5 Å are not described precisely by the PDF fit and thus δ doesn't represent the true ratio between the 3.0 and 3.5 Å PDF peak leading to a likely incorrect magnetite phase ratio. Similar observations are made for the smaller (d = 3.5 nm) IONP stabilized by citrate and phosphocholine. But, in contrast to the betaine-stabilized particles, the R_W value improves slightly for the tetragonal model (Table A 13), indicating that the existing crystal structure is likely dependent on the particle diameter and the magnetite phase ratio, which is 0 % for both refinements of both particles.

In comparison to Cooper et al.,[6] a clear determination of the underlying space group of the synthesized IONPs is not possible. Depending on the particle diameter, the quality of fit of the cubic and tetragonal refinement varies. Thus, the determination of the maghemite/magnetite ratio is rather a guess than a clear estimation. Due to disorder, especially in the short-range order caused by the small crystallite size, the possibility for over-interpretation of these observations is given. However, it is still very likely that the smaller 3.5 nm IONPs consist of pure maghemite, as oxygen can penetrate more easily

to the core of the smaller particles. Finally, as the cubic *Fd-3m* model has the higher symmetry constraints and results only for the phosphocholine-stabilized IONP in a noticeable worse R_W value, the cubic model should be considered as the more appropriate refinement approach. As cation distribution or vacancy ordering in IONP is proven to effect the catalytic behavior,[125] this insight is valuable for the development of new species of catalysts.

In comparison to the PDF refinements of the spinel ferrite nanoparticles in chapter 5.1, the refinements of the IONPs are based on the same model, a *Fd-3m* symmetry with a parameter accounting for the vacancies on the octahedral sites. Considering the bulk materials, a similarity but not an equality of the models was expected. This is another hint that spinel ferrite nanoparticles synthesized via the same method consist of a very similar structure, unaffected by the metal composition.

5.3 Total Scattering Analysis of Spinel Ferrite Nanoparticles obtained via different Synthesis Routes

As part of cooperation projects, the structure analysis of $MnFe_2O4$ and $Co_xFe_yO_4$ nanoparticles by means of PXRD and PDF was conducted. Their phase composition after calcination at different temperatures was tackled primarily. But also, as the synthesis route has a big influence onto the final structure of nanoparticles, their structure is compared with the spinel ferrite nanoparticles synthesized via the polyol route (chapter 4.1 and 5.1).

5.3.1 Temperature Induced Phase Transition of $MnFe_2O_4$ Nanoparticles

As part of a cooperation with the workgroup of Prof. Marschall (Bayreuth), $MnFe_2O_4$ nanoparticles were synthesized in a microwave-assisted non-aqueous sol-gel synthesis route, followed by thermal treatment at 400, 600 or 800 °C in air. The nanoparticles are analyzed by different methods like XRD, PDF, Mössbauer and Raman spectroscopy. Tracking the phase evolution caused by the thermal treatment of the $MnFe_2O_4$ nanoparticles by means of XRD and PDF and the comparison of the structure in comparison to spinel ferrite nanoparticles synthesized in DEG is part of this thesis. This study was partially published in C. Simon, A. Blösser, M. Eckardt, H. Kurz, B. Weber, M. Zobel, R. Marschall, *Z. Anorg. Allg. Chem.* **2021**, *647*, 2061-2072.

According to TEM analysis, the as-synthesized nanoparticles have an average diameter of 6.0 nm and 6.3 nm after treatment at 400 °C. All samples are crystalline, as lattice planes are visible in the TEM images. At 600 °C particle growth starts and leads to an increased crystallite diameter according to PDF of ca. 15.1 and 36.0 nm for samples treated at 600 and 800 °C, respectively. XRD analysis (Figure 26 A) reveals a cubic spinel structure for the as-synthesized and the 400 °C samples. The positions of the reflections for the as-synthesized nanoparticles are directly in between the ones of the calculated reference patterns for Fe_3O_4 and $MnFe_2O_4$. This could point towards domains of varying composition with Mn and Fe, a co-existence of phases or an elemental gradient within the nanoparticles. Compared to the as-synthesized sample, the XRD pattern of the 400 °C sample is shifted slightly to higher *Q*-values, accompanied by the presence of amorphous signal between 1.5 and 5.5 $Å^{-1}$ (Figure 26 B). Finally, the sample has transitioned at 600

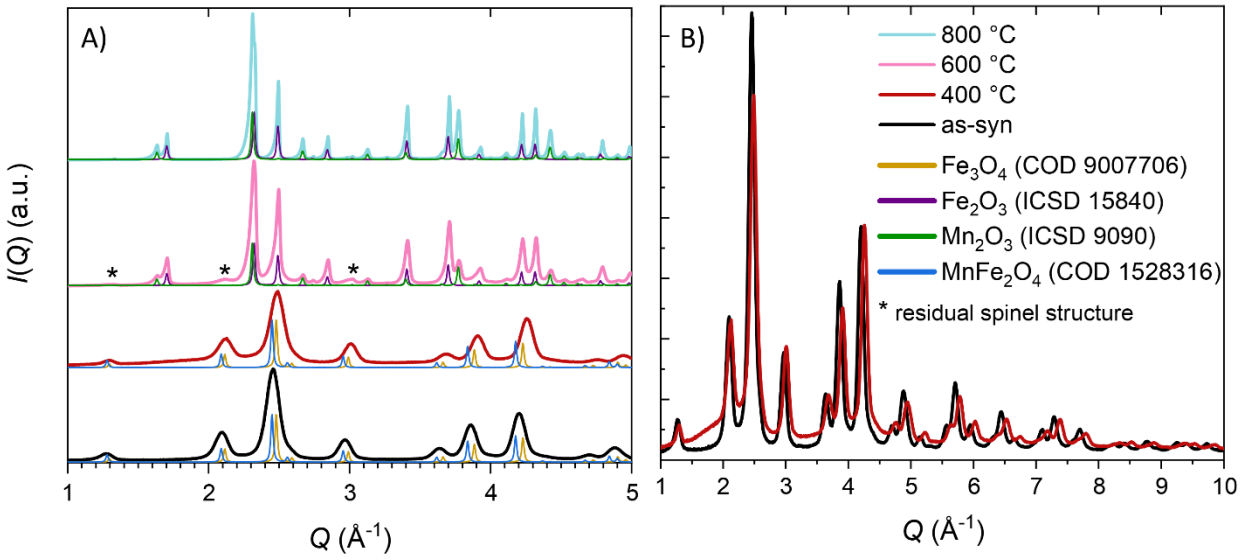

Figure 26: A) XRD patterns of samples directly after synthesis (black) and after calcination at 400 (red), 600 (pink) and 800 °C (light blue). *The patterns are stacked and scaled for clarity. Calculated reference patterns of Fe_3O_4, $MnFe_2O_4$, α-Fe_2O_3 and α-Mn_2O_3 are inserted individually at each temperature to highlight existing phases. Reflections of residual spinel structure in the 600 °C sample are marked with *. B) XRD patterns of as-synthesized and 400 °C samples to highlight the shift in reflex positions and the occurrence of the amorphous signal between 1.5 and 5.5 $Å^{-1}$.*

and 800 °C into co-existing α-Fe_2O_3 (hematite) and α-Mn_2O_3, with some residual spinel phase in the 600 °C sample. This strengthens the point that a phase separation already sets in at 400 °C into presumably an iron-rich spinel phase and nanoscaled amorphous domains of manganese oxide.

PDF refinements of the as-synthesized and the 400 °C sample (Figure 27 A, B) is largely consistent with XRD analysis. However, as Mn(II) and Fe(III) have isoelectronic configuration, whether by XRD nor by PDF a distinction between those two atoms can be made, which makes the analysis quite challenging. For the as-synthesized sample, a two-phase refinement of two cubic spinel structures results in the best fit. They were restricted to only differ in the lattice parameters and the scale. As the stoichiometric ratio of Mn/Fe in the nanoparticles was proven to be 1/2 according to elemental analysis, a compositional or structural gradient with varying lattice parameters between 8.440 Å to 8.503 Å, like it was already suggested by XRD analysis, could exist. This could be illustrated by a core-shell model, varying lattice parameters from particle surface to core or the co-existence of Fe-rich ($Mn_{1-y}Fe_{2+y}O_4$) and Fe-poor ($Mn_{1+y}Fe_{2-y}O_4$) domains, for instance. The refinement of the occupancy of the octahedral sites results in values close to 1. Due to this fact, a defect structure like maghemite (γ-Fe_2O_3) can be excluded.[6-7]

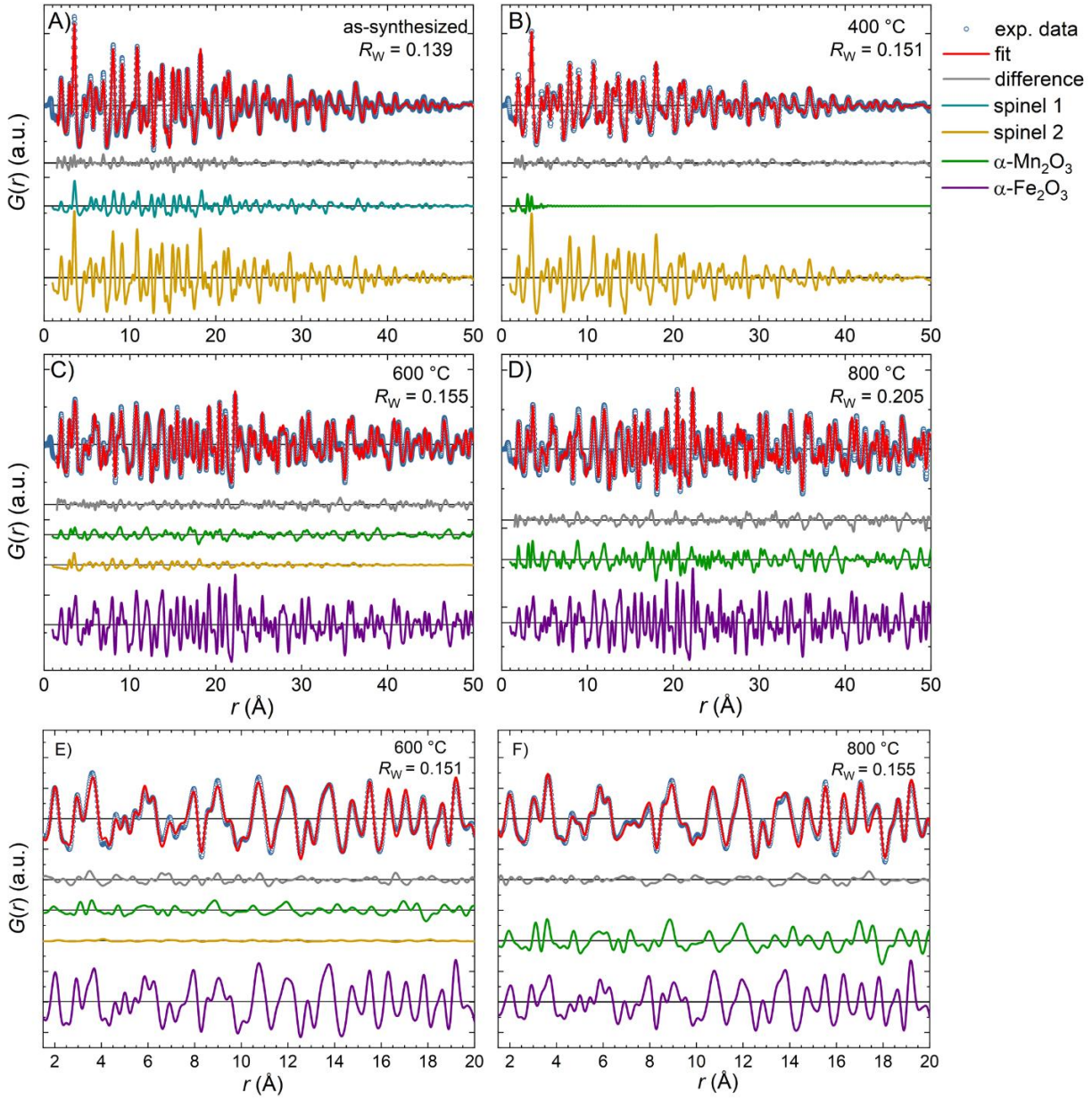

Figure 27: PDF refinements over 1.5 to 50 Å of the as-synthesized nanoparticles (A) and the ones after calcination at 400 (B), 600 (C) and 800 °C (D) as well as the short-range PDF refinements (1.5 to 20 Å) after calcination at 600 (E) and 800 °C (F). *Blue open circles and red solid lines correspond to measured and simulated PDFs. Grey solid lines are the differences. Blue and ochre solid lines represent the contribution of two different spinel phases to the refinements. Green and purple solid lines represent the fit contribution of α-Mn_2O_3 and α-Fe_2O_3, respectively. The R_W value of the short-range refinement of the 600 °C sample (E) is nearly equal to the 50 Å fit. For the 800 °C sample, the R_W is significantly lower for the short-range refinement (F). All contributions and differences are plotted in offset, for clarity.*

The PDF analysis of the 400 °C sample proofs the assumption made in the XRD analysis that a Mn_2O_3 phase exists. Its refinement results in a very small domain size of 0.62 nm. However, the refinement is made with a spherical shape assumption and the refined domain size of 0.62 nm is more the size of a cluster than a crystalline domain, which may

lead to a rather inaccurate estimation. Still, due to the α-Mn_2O_3 phase the refinement improves from a R_w of 0.18 to 0.15, indicating that at 400 °C a phase transition has started. Next to the formation of manganese oxide due to the oxidation of the Mn(II) ions, the lattice parameter of the spinel phase decreases in comparison with the as-synthesized sample (8.343 Å) which is even shorter than in bulk Fe_3O_4 (8.394 Å). From the resulting molar phase contents of α-Mn_2O_3 and the spinel phase in the PDF fits and the Mn/Fe ratio from EDXS (0.52) the average spinel sum formula was calculated to be $Mn_{0.43}Fe_{2.57}O_4$ (Equation A9). Thus, it is a Fe-rich manganese spinel structure.

Calcination at 600 °C results in a highly crystalline α-Fe_2O_3 phase and an increased phase fraction of α-Mn_2O_3 while the spinel phase decreased. The three-phase refinement results in a R_w of 0.16 (Figure 27 C). This was proven earlier in studies on the phase transitions of pure iron and manganese oxide nanoparticles as well as manganese ferrite nanoparticles. It was revealed that Mn_5O_8 transforms into α-Mn_2O_3 at 550 °C[126] and Fe_3O_4 transforms into α-Fe_2O_3 between 400 and 500 °C.[127] Also an example for the phase separation of $MnFe_2O_4$ nanoparticles into α-Fe_2O_3 and α-Mn_2O_3 by annealing at 550 °C exists.[128] If only the short range from 1 – 20 Å (Figure 27 E) refined, the fit is not improved (R_W = 0.15). This indicates that the short and medium-range order are similar. Further rise of the calcination temperature to 800 °C yields in a complete phase transition to α-Fe_2O_3 and α-Mn_2O_3. Surprisingly, the refinement of the larger and more crystalline 800 °C sample (Figure 27 D) results in a higher R_W = 0.21 than the refinement of the 600 °C sample. In the difference curve, the structural features can be localized. They occur mainly for r > 15 Å. Thus, for this sample, the short-range order fit (Figure 27 F) results in a reduced R_W of 0.16. This observation can probably arise from a polydispersity of the α-Fe_2O_3 and α-Mn_2O_3 domains or crystal defects.

To summarize, according to PDF and XRD analysis, the crystal structure of the 6 nm $MnFe_2O_4$ nanoparticles obtained by microwave-assisted synthesis deviates from the suggested spinel structure. Instead of a single-phase refinement, the best fit is achieved by a two-phase refinement of two spinel phases with two different lattice parameters. A model, which can illustrate this, may be the co-existence of Fe-rich and Fe-poor spinel phase or a gradient of the lattice parameter, e.g. from the core to the surface of the nanoparticles. With heat treatment at 400 °C the phase transition of the $MnFe_2O_4$ spinel

phase to α-Mn_2O_3 begins. At 600 °C, the quantity of the α-Mn_2O_3 phase increases simultaneously with the formation of α-Fe_2O_3. The content of both, α-Mn_2O_3 and α-Fe_2O_3, increases at 800 °C, where no residue of the original spinel phase can be detected.

To compare the structure of the microwave-assisted synthesized $MnFe_2O_4$ nanoparticles[129] with the spinel ferrite nanoparticles synthesized in DEG (see chapter 5.1) the as-synthesized $MnFe_2O_4$ and the citrate-stabilized $ZnFe_2O_4$ nanoparticles are contrasted in Figure 28. Both had no thermal treatment after the synthesis and are most similar in diameter. The peaks of the microwave-assisted synthesized $MnFe_2O_4$ nanoparticles are slightly broader and have less intensity in comparison to the $ZnFe_2O_4$ nanoparticles synthesized in DEG. Also, very close peaks, e.g. in the *r*-range of 19.5 to 20 Å, are not separated and appear as one. This is an indication that the structure of the $ZnFe_2O_4$ nanoparticles has a higher degree of crystallinity even though they are smaller. This likely results from the high achievable temperature in the polyol synthesis route.

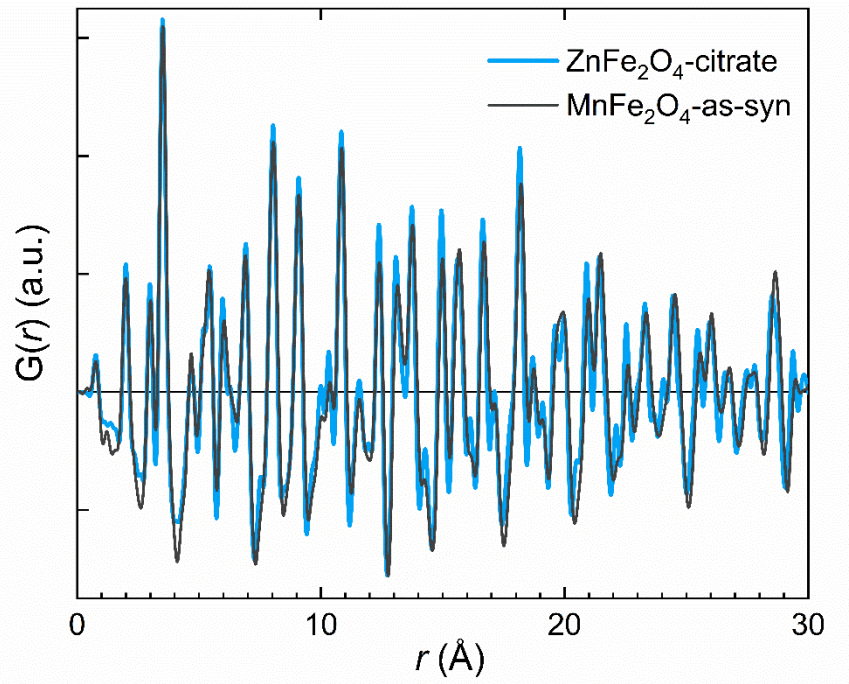

Figure 28: Experimental PDF data of microwave-assisted synthesized as-synthesized $MnFe_2O_4$ (black) and in DEG synthesized citrate-stabilized $ZnFe_2O_4$ nanoparticles (blue) in a r-range of 0 – 30 Å.

5.3.2 Miscibility Gap of Cobalt and Iron Containing Spinel Ferrites

In a cooperative study with the workgroup of Prof. Behrens (formerly at the University of Duisburg-Essen, now at the Christian-Albrechts-Universität zu Kiel), the structure of cobalt/iron layered double hydroxides with a molar ratio of Co/Fe = 2/1 after different calcination temperatures of 400, 800 and 900 °C was investigated by TEM images and TEM-EDX studies, Mössbauer spectroscopy, XRD and PDF. The PDF analysis of this material and the structural comparison to spinel ferrite nanoparticles synthesized in DEG is part of this thesis.

Phase-pure cobalt/iron layered double hydroxides (LDH) with a hydrotalcite structure were synthesized via co-precipitation in an automated lab reactor system. During calcination, a phase transition to different spinel ferrite phases with varying Co/Fe ratio takes place. Whereas XRD studies reveal that the 800 °C sample consists of an iron-rich $CoFe_2O_4$ and an non-iron-containing Co_3O_4 phase, the 900 °C sample consists of a single phase of Co_2FeO_4 (Figure A 11). Due to the distinct crystallinity of these two samples and thus the sharp Bragg peaks in the XRD pattern, the analysis is highly reliable. However, the low crystallinity of the 400 °C sample and the resulting Bragg peak broadening makes it really hard to distinguish between the different spinel phases in reciprocal space, as Rietveld refinements with only Co_2FeO_4 or with both, Co_3O_4 and $CoFe_2O_4$ yields the same goodness-of-fit value. In this case, PDF analysis is particularly useful, as the short and middle-range order in disordered or nanomaterials is accessible. All processed PDF refinements describe the experimental data well ($R_W \leq 0.20$) in a fit range of 1 – 50 Å for samples calcined at 400 and 800 °C and in a fit range of 1 – 100 Å for the sample calcined at 900 °C (Figure 29).The obtained Rietveld results for the 800 and 900 °C sample are confirmed by the PDF refinements. After calcination at 900 °C, the material consists of large single-phase Co_2FeO_4 crystallites with average sizes of 106 nm. However, the size determination by PDF refinements is calculated from the decrease of the envelope which is also dependent on the instrumental parameter q_{damp}. The finite instrumental resolution leads to an uncertainty of the calculated crystallite diameter for large crystallites with $d > 10$ nm. Whereas, after calcination at 800 °C two phases of $CoFe_2O_4$ and Co_3O_4 with crystallite diameters of 12.7 and 13.8 nm, respectively, coexist. The refined molar content of both phases is 1/1, which represents the initial stoichiometry of Co^{2+} and Fe^{3+} in the

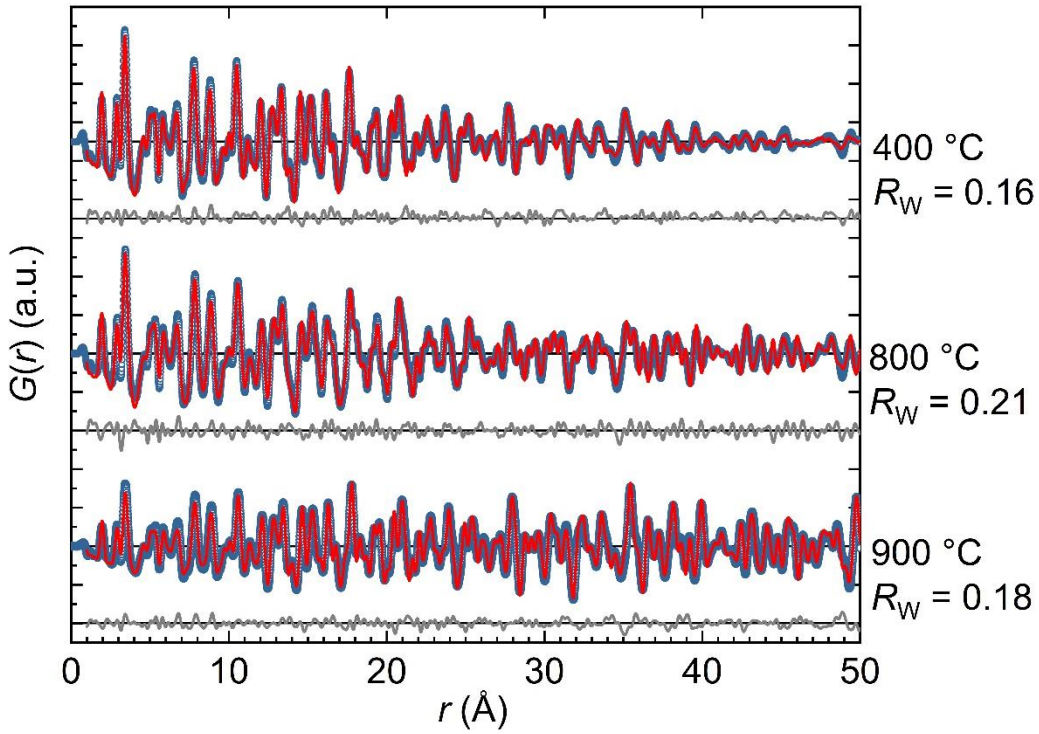

Figure 29: PDF refinements from 1.0 to 50 Å based on a two-phase model of Co_3O_4 and $CoFe_2O_4$ of samples calcined at 400 and 800 °C and from 1.0 to 100 Å based on a single-phase model of Co_2FeO_4 for the sample calcined at 900 °C. *Blue open circles and red solid lines correspond to measured and simulated PDFs, respectively. Grey solid lines directly beneath the experimental data and the fit are the differences. The patterns are stacked for clarity. For raw data of the PDF until 100 Å see Figure A 13.*

LDH precursor material. However, the resulting lattice parameters for the Co_3O_4 and the $CoFe_2O_4$ phase shift to slightly longer (8.187 Å) and shorter (8.318 Å) values, respectively. This could be caused by an inaccurate or changing stoichiometry of the cobalt and iron ions in the nanoparticles leading to mixed phases like $Co_{3-x}Fe_xO_4$ or $Co_{1+y}Fe_{2-y}O_4$.

The comparison of the single-phase and the two-phase PDF refinement of the sample treated at 400 °C shows that the two-phase fit of $CoFe_2O_4$ and Co_3O_4 describes the experimental data better than a single-phase fit of Co_2FeO_4 (confer to Figure 29 top and Figure A 12 as well as Table A 14). The most obvious difference between the two refinements is the various length of the lattice parameter *a* of the spinel unit cell. Whereas one lattice parameter of 8.178 Å results in an already good description of the experimental data (R_W = 0.20), two different lattice parameters (8.209 and 8.156 Å) lead to an increase of the fit quality (R_W = 0.16). This indicates that not only two distinct unit cells consisting

of pure Co_3O_4 and $CoFe_2O_4$ exist, but probably a compositional or structural mixture with varying lattice parameters within the material.

In combination with the results from Mössbauer and Raman spectroscopy, the PDF analysis sheds light onto the structural composition of cobalt and iron containing spinel ferrites synthesized by calcination of cobalt and iron containing LDHs. Starting from the hydrotalcite structure, two different phases, Co_3O_4 and $CoFe_2O_4$, or at least phases which are similar to those two, are formed after calcination at 400 °C. Until 800 °C the crystallinity of these two phases increases and clearly two phases exist, which are combined to a single-phase of Co_2FeO_4 after phase transition at 900 °C. This structural miscibility gap is highly interesting for applications of cobalt and iron containing spinel ferrites in e.g. the CO oxidation, oxygen evolution reaction or oxygen electrocatalysis at increased temperature.[130-132] The insight in the crystal structure of other $CoFe_2O_4$ related materials is helpful for the analysis and interpretation of the structure of and hydration shells around spinel ferrite and especially around $CoFe_2O_4$ nanoparticles synthesized in DEG, what is targeted in this thesis.

6 Analysis of the Surface Chemistry

Applications of spinel ferrite or iron oxide nanoparticles in e.g. hyperthermia or ferrofluids require a very high stability of these nanoparticles in the dispersed state. They must be inert against Ostwald ripening and coalescence as both would lead to the loss of the colloidal stability and to the precipitation of the nanoparticles. This can cause toxic incorporations in the human body or dysfunction of the ferrofluid in case of the given examples. The synthesis and characterization of the spinel ferrite nanoparticles was highlighted in chapter 4 and 5. However, an experimental deep insight in the interaction of solvent molecules with the nanoparticle surface and the stabilizing molecules, is challenging. The small signal resulting from the solvation shell in comparison with the surrounding bulk solvent and the mostly crystalline nanoparticles is hard to extract. Since the 1970's, theoretical approaches of the presence of solvent restructuring around nanoparticles exist.[24-25, 29, 133] Additionally, nanoparticle-solvent interactions are affected by various modulations of the nanoparticle chemistry like crystal structure, crystal plane at the surface or surface chemistry.[24, 29]

By means of PDF, this very small signal could be extracted with synchrotron radiation on colloidally stable dispersions of ZnO nanoparticles in water and primary alcohols.[26-27] However, a study about the impact of composition, structure and shape on the solvation shell is still missing. This chapter will try to access signals from the d-PDF data and possibly correlate them with MD studies on hydration shells.

6.1 Surface Coverage of Spinel Ferrite Nanoparticles

At first, to draw conclusions about the solvation shell of the spinel ferrite nanoparticles the knowledge of the surface composition of the spinel ferrite nanoparticles is evident. The revelation of the amount of stabilizer and solvent molecules at the nanoparticle surface, their binding modes and the grafting density is crucial for the interpretation of the hydration shell signals. Thus, a zeta potential, FT-IR, TGA and CHN analysis were carried out on all synthesized spinel ferrite nanoparticles. The approach to combine TGA and CHN results to determine quantitatively the organic molecules at the nanoparticle surface goes also back to Ms. Sabrina Thomä and is published in M. Eckardt, S. L. J. Thomä, M. Dulle, G. Hörner, B. Weber, S. Förster, M. Zobel, *ChemistryOpen* **2020**, *9*, 1214-1220.

Zeta Potential

The zeta potential analysis gives the electrical potential at the end of the diffuse layer, the slipping plane, around a colloidal particle.[134] From this value, the electrostatic repulsion between such particles in a dispersion can be derived. A nanoparticle dispersion with a zeta potential $|\zeta| > 25$ mV is considered to form colloidally stable, electrostatic stabilized dispersions.[135] However, zeta potential measurements should not be considered to give an absolute proof but rather an indication of the stability of colloidal dispersions.[136] Table 17 shows that all synthesized spinel ferrite nanoparticles meet this requirement. Due to free carboxylate groups, citrate-stabilized nanoparticles have negative zeta potential.[137] Betaine- and phosphocholine-stabilized nanoparticles have positive zeta potential due to the negatively charged phosphate and carboxyl groups coordinating to the surface and the quaternary ammonium groups defining the electrostatic properties. It is noticeable that the absolute zeta potential of nanoparticles stabilized with the same stabilizer varies for the different nanoparticle compositions. However, no trend considering TOC (chapter 6.1), size (chapter 4.1) or structure (chapter 5.1) is discernible.

Table 17: ζ-potentials of spherical spinel ferrite nanoparticles.

Nominal composition	stabilizer	ζ – potential (mV)
$CoFe_2O_4$	citrate	- 49.1 ± 0.9
	betaine	46.7 ± 0.6
	phos	46.5 ± 1.1
$ZnFe_2O_4$	citrate	- 45.9 ± 1.4
	betaine	38.4 ± 2.3
	phos	43.9 ± 1.8
$MgFe_2O_4$	citrate	- 40.6 ± 1.9
	betaine	43.4 ± 1.2
	phos	27.6 ± 0.5
$NiFe_2O_4$	citrate	- 34.5 ± 1.0
	betaine	34.4 ± 1.2
	phos	45.9 ± 1.0

FT-IR

By qualitative FT-IR analysis, the molecules present at the nanoparticle surface can be identified and their binding mode can be elucidated. The important regions of the FT-IR spectra of the dry powders of the synthesized spinel ferrite nanoparticles are shown in Figure 30. All spectra confirm the presence of the respective stabilizer molecule, as the peaks from the pure substance are visible in the spectra of the nanoparticles. For citrate- and betaine- stabilized spinel ferrite nanoparticle, the spectral region from 1700 $cm^{-1} > \nu >$ 1000 cm^{-1} is shown, due to the characteristic absorption of the carboxyl groups appearing there. In the citrate reference spectrum, which is sodium citrate powder, the asymmetric carboxylate mode ($\nu_{asym,COO}$) appears at 1580 cm^{-1}. For all nanoparticle spectra, it shifts to 1566 cm^{-1} and the corresponding peak becomes broader. In contrast, the peak for the symmetric mode ($\nu_{sym,COO}$) remains almost equal in position and also shape. Only at $\nu \approx$ 1400 cm^{-1} some features are missing. Korpany et al. summarized different carboxylate coordination geometry in in dependence of the separation $\Delta\nu$, which is the difference in wavenumber between the FT-IR bands of the asymmetric and symmetric carboxylate

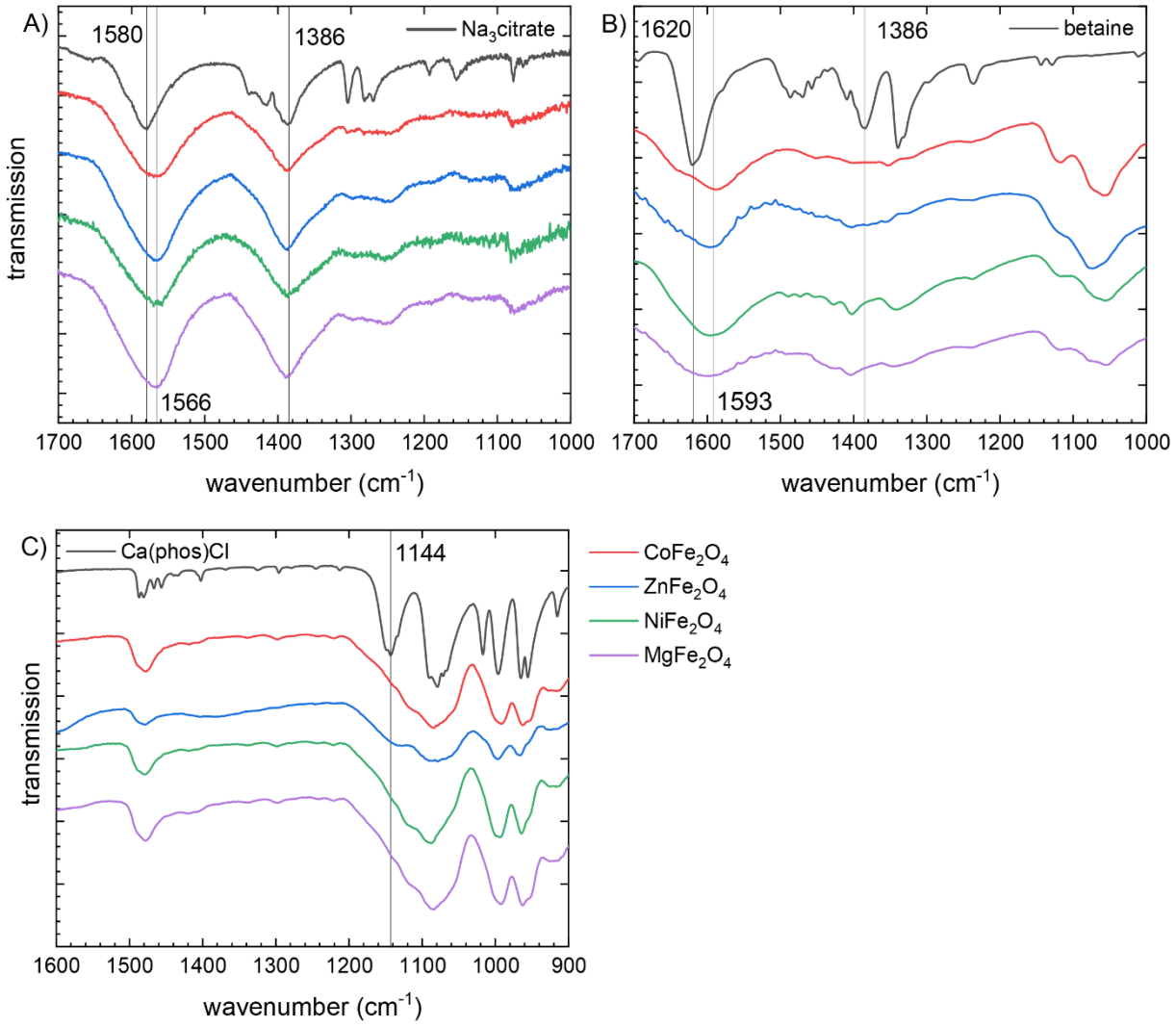

Figure 30: FT-IR spectra of A) citrate, B) betaine and C) phosphocholine stabilized spinel ferrite nanoparticles supplemented by the corresponding FT-IR spectra of the pure stabilizer salt. *Vertical lines highlight peak positions of interest. All spectra are stacked for clarity.*

mode ($\nu_{asym,COO}$ - $\nu_{sym,COO}$).[138] Calculated from maximum to maximum of the bands, $\Delta\nu$ is 180 cm^{-1} for all citrate-stabilized spinel ferrite nanoparticles. Referring to the study of Korpany et al. and Noerpel et al., the carboxylate groups of the citrate molecule are mainly coordinated to the spinel ferrite surface in a binuclear bidentate configuration.[138-139] However, as the width of both FT-IR peaks for the asymmetric and symmetric carboxylate mode increased when coordinated to the nanoparticle surface, it is very likely that different coordination geometries like monodentate, bidentate or salicylate, co-exist.[140]

For the betaine-stabilized spinel ferrite nanoparticles, the peak for $\nu_{asym,COO}$ is at a higher wavenumer ($\nu_{asym,COO}$ = 1593 cm^{-1}) in comparison to the citrate-stabilized nanoparticles. In the FT-IR spectra of the pure stabilizer salts the shift of $\nu_{asym,COO}$ to higher wavenumbers – 1580 cm^{-1} for sodium citrate and 1620 cm^{-1} for betaine – is attributed to the presence of the sodium ions. Thus, the carboxyl group coordinates to the sodium ions. However, the shift from 1620 cm^{-1} of $\nu_{asym,COO}$ of pure betaine to 1593 cm^{-1} of the betaine-stabilized nanoparticles confirms the coordination of betaine to the surface of the spinel ferrite nanoparticles. As $\nu_{sym,COO}$ is only barely visible in the FT-IR spectra of the betaine-stabilized nanoparticles, $\Delta\nu$ can't be calculated in a reliable way. Thus, an assumption of the coordination geometry of the carboxyl group of betaine at the nanoparticle surface can only be made on basis of the $\nu_{asym,COO}$ mode. According to Noerpel et al. the bidentate geometry is prevalent for $\nu_{asym,COO} \approx$ 1590 cm^{-1}.[139] Additionally, two peaks at ν = 1050 cm^{-1} and ν = 1125 cm^{-1} are visible in the FT-IR spectra of the betaine-stabilized nanoparticles, which are not present in the pure betaine. They can be attributed to the asymmetric and symmetric C-O stretching vibrations of DEG, respectively. Similar as for the carboxyl groups of betaine and citrate, the absorption of the C-O stretching modes shift in the FT-IR spectra, if the oxygen of the hydroxyl group coordinates to the surface of spinel ferrite nanoparticles.[62] If compared with the citrate-stabilized nanoparticles, the potential of betaine to replace the DEG solvent molecules from the spinel ferrite surface is lower, as the C-O stretching modes of DEG don't appear in the FT-IR spectra of the citrate-stabilized spinel ferrite nanoparticles. Thus, DEG and betaine coexist at the nanoparticle surface.

In contrast to citrate and betaine, phosphocholine coordinates by the PO_4^{2-} moiety to the nanoparticle surface. Its most characteristic mode in FT-IR spectroscopy is the asymmetric stretching vibration of PO_2^- ($\nu_{asym,PO2}$), which is visible at 1144 cm^{-1} in Figure 30 C.[141] Its peak shape shifts, when coordinating to the spinel ferrite nanoparticle surface. This change results in a very broad feature from 1030 – 1200 cm^{-1}, overlapping with other FT-IR active modes in this area. However, until now no thoroughly studies about the coordination geometry of PO_4^{2-} moieties and its influence on the FT-IR active modes exist. But it needs to be assumed that, similar to the carboxyl groups in citrate or betaine, many different binding modes may coexist. Additionally, as shown for the betaine-stabilized

spinel ferrite nanoparticles, the C-O stretching modes of DEG appear in the discussed spectral region, which may contribute to this broad peak.

In general, FT-IR studies on the citrate-, betaine- and phosphocholine-stabilized nanoparticles prove coordination of all stabilizers to the nanoparticle surface via the carboxyl or phosphoryl moieties. The determination of the nature of the prevalent coordination chemistry is challenging, as many different coordination states likely coexist. Further, FT-IR studies prove the incomplete exchange of DEG by the stabilizer molecules. This makes a quantification of the different organic molecules coordinating to the nanoparticles surface necessary.

TGA

In ample literature a thoroughly characterization of the surface chemistry at nanoparticles is missing. Often, the organics at the surface are ignored or directly mathematically converted into the surface coverage.[20, 47, 142] Even if the surface chemistry is characterized, TGA is often performed without any qualitative or quantitative analysis of the gaseous products.[143] Here, the approach to combine TGA and CHN to quantify the species coordinated to the nanoparticle surface, which was developed together with Ms. Sabrina Thomä (University of Bayreuth), is presented. For this purpose, the presence of heteroatoms, here N, in betaine and phosphocholine is useful for the distinction between remaining DEG and stabilizer in CHN analysis (Figure 11). In Figure 31, the TGA plots of zinc ferrite nanoparticles stabilized by citrate, betaine and phosphocholine are shown. They are exemplarily for all types of synthesized spinel ferrites. For citrate- and phosphocholine-stabilized spinel ferrite nanoparticles the total organic content (TOC) is given before and after dialysis. Dialysis for those two stabilizer species was necessary due to the high TOC of up to 45 wt%, which can neither be described by a monolayer nor other models like a multiple layered stabilizer shell (for calculation see equation A10).[144] Thus, a high amount of stabilizer cannot be bound or coordinated to the inorganic nanoparticle surface and will not contribute to the stabilizing effect. Likely, the high amount of these free organic molecules will also interfere with the investigation of the hydration shells around spinel ferrite nanoparticles (discussed in chapter 6.3). For the segregation of the free organic stabilizer from the spinel ferrite nanoparticles and the coordinated

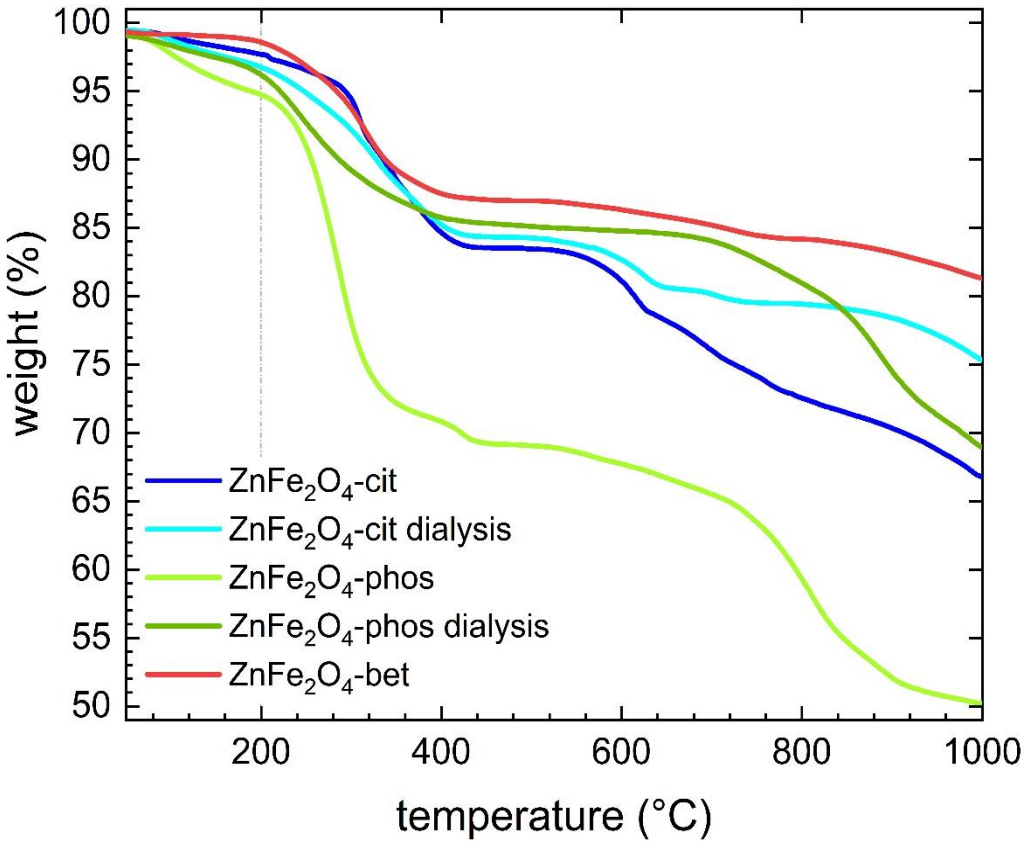

Figure 31: TGA plots of $ZnFe_2O_4$ nanoparticles stabilized with citrate (blue), betaine (red), and phosphocholine (green). *For dialyzed samples, TGA plots before and after dialysis are shown. The mass loss until the dotted line at 200 °C is assigned to residual moisture.*

stabilizer species, dialysis shows the best results among other methods like centrifugation. Dialysis of betaine-stabilized spinel ferrite nanoparticles wasn't necessary, as, except for $MgFe_2O_4$, the maximum amount of organic content is 27 wt%. The decrease of stabilizer amount due to dialysis of betaine-stabilized nanoparticles causes the loss of the colloidal stability and thus, precipitation of the nanoparticles during dialysis.

Assuming that next to moisture only the stabilizing agent is coordinated to the nanoparticle surface and solely contributes to the calculated TOC in the TGA experiments (Table 18), the grafting density, which is the number of stabilizer molecules per nm^2 of nanoparticle surface (ρ^{graft}), can be determined following Equation 6.[145-146] The mass loss up to 200 °C is attributed to the loss of residual moisture. The results are summarized in Table 18.

$$\frac{m_{single\ NP} * N_{stabilizer\ molecules}}{m_{NP\ sample} * S_{single\ NP}} = \rho^{graft} \qquad \text{Eq. 6}$$

with:

$\rho_{graft} = density\ of\ the\ stabilizer\ molecules\ per\ nm^2\ nanoparticle\ surface,$

$m_{single\ NP} \cong V_{single\ NP} * \rho,$

with: $\rho = specific\ mass,$

$$N_{stabilizer\ molecules} = \frac{m_{organic}^{TGA} * N_A}{M_{stabilizer\ molecule}},$$

with: $N_A = Avogadro\ constant,$

$m_{organic}^{TGA} = organic\ mass\ from\ TGA$ (Table 18),

$m_{NP}^{TGA} = m_{total}^{TGA} - m_{H2O}^{TGA} - m_{organic}^{TGA} = inorganic\ mass\ of\ TGA\ sample,$

with: $m_{total}^{TGA} = total\ mass\ of\ TGA\ sample,$

$m_{H2O}^{TGA} = mass\ of\ H_2O$ (Table A 16).

Before dialysis, ρ^{graft} varies for citrate stabilized spinel ferrite nanoparticles between 4.6 and 9.7 nm^{-2} and for phosphocholine stabilized nanoparticles between 9.8 and 15.8 nm^{-2}. As pointed out above, such high amount cannot coordinate to the nanoparticles surface regardless of whether the number of surface iron sites (3.5 – 5.9 nm^{-2})[147] or the spatial requirement of the anchor groups is crucial. The latter results in a maximum grafting density of 4.3 nm^{-2} for carboxyl groups (kinetic diameter: 23 Å^2)[148] and, considering the larger size of the phosphate group, even less for phosphocholine. Through dialysis, ρ^{graft} decreases for citrate stabilized nanoparticles to 3.1 – 5.5 nm^{-2}. This correlates very well to both constraints and leads to the assumption, that citrate forms a monolayer on the spinel ferrite nanoparticles. However, if it is taken into account, that some citrate molecules coordinate to two surface iron sites through the bidentate bridging mode, which was evaluated in FT analysis, the grafting density for nickel ferrite nanoparticles with 5.5 nm^{-2} is out of this range. Phosphocholine instead, can only coordinate to one surface iron site and forms a monolayer for cobalt, magnesium and nickel ferrite nanoparticles. Only for the zinc ferrite nanoparticles, ρ^{graft} is too high to form a monolayer. For betaine stabilized spinel ferrite nanoparticles, ρ^{graft} varies from 3.4 to 5.4 nm^{-2} without dialysis.

Table 18: TOC of spinel ferrite nanoparticles without ($TOC_{as\text{-}syn}$) and with dialysis (TOC_{dia}) obtained by TGA and the calculation of the grafting density ρ_{graft}. *Dialysis of betaine-stabilized nanoparticles wasn't successful and results in precipitated nanoparticles.*

sample	stabilizer	$TOC_{as\text{-}syn}$ (wt%)	TOC_{dia} (wt%)	$\rho^{graft}_{as\text{-}syn}$ (nm^{-2})	ρ^{graft}_{dia} (nm^{-2})
$CoFe_2O_4$	citrate	27.4	20.6	4.6	3.1
	betaine	26.9	-	3.8	
	phos	43.5	16.1	11.5	3.2
$ZnFe_2O_4$	citrate	30.9	21.9	8.2	3.9
	betaine	17.3	-	3.4	
	phos	44.6	27.4	15.8	6.9
$MgFe_2O_4$	citrate	49.2	28.7	9.6	3.7
	betaine	33.6	-	3.8	
	phos	43.2	16.5	9.8	2.1
$NiFe_2O_4$	citrate	22.6	33.7	9.7	5.5
	betaine	26.2	-	5.4	
	phos	44.5	20.5	15.3	4.4

This implies that the washing procedure with acetone and ethanol in the standard synthesis works well to remove remaining, non-coordinating betaine molecules from the nanoparticles and a stabilizing monolayer of betaine remains. However, considering the assumptions and errors of the calculation on which the analysis is based on, a more precise investigation based on these results would barely be reliable.

CHN

The knowledge of ρ^{graft} obtained by TGA analysis in combination with the FT-IR results gives already a good estimation of the surface chemistry on the spinel ferrite nanoparticles. However, as it is indicated by the FT-IR analysis and also published in literature, not only stabilizer molecules coordinate to the nanoparticle surface but also remaining DEG from the nanoparticle synthesis.[62, 69] Also humidity may lead to H_2O molecules on the nanoparticle surface. Thus, the stabilizer species present on the nanoparticle surface is quantified by means of CHN analysis. As this approach is based on the presence of a different atom than C, O or H on the stabilizer molecule, it is realized

on all four phosphocholine-stabilized nanoparticles and on betaine-stabilized nickel and cobalt ferrite nanoparticles. Due to the N in betaine and phosphocholine it is possible to calculate the molar ratio of the organic species at the nanoparticle surfaces via the stoichiometry. First, all detected N is ascribed to stem from the stabilizer molecule. The stoichiometric correlating amount of C and H is then subtracted from the detected amount of C and H. All residual C is then ascribed to stem from residual DEG and the stoichiometric correlating amount of H is then again subtracted from the overall amount of H. Last, all residual H is ascribed to stem from H_2O, which is coordinated to the nanoparticle surface and also to the organic molecules present there. The results are summarized in Table 19. The raw data is shown in Table A 17.

At first sight, it is astonishing that betaine-stabilized nickel and cobalt ferrite nanoparticles contain only 0.9 and 1.8 wt% of stabilizer and 13.2 and 13.0 wt% of DEG, respectively. This indicates that the stabilizer exchange of DEG with betaine is not as successful as the overall colloidal stability let it seems to be. It is not, as supposed by FT-IR analysis, a mixture of betaine and DEG coordinating to the nanoparticle surface but a 7 to 15-fold excess of DEG. However, despite the low calculated amount of betaine, it still contributes

Table 19: Quantification of stabilizer species at the nanoparticle surface derived from calculations based on CHN analysis. *The result is given relative to the initial mass of the sample in wt% and absolte in mol. All phosphocholine-stabilized samples were dialyzed before the analysis. Citrate-stabilized samples are omitted as citrate doesn't contain heteroatoms.*

sample	stabilizer	content of stabilizer		content of DEG		content of H_2O		TOC^{CHN}
		(wt%)	(µmol)	(wt%)	(µmol)	(wt%)	(µmol)	(wt%)
$CoFe_2O_4$	betaine	0.9	0.3	13.2	4.5	1.2	2.4	15.3
	phos	6.1	0.7	8.4	1.6	4.7	5.4	19.2
$ZnFe_2O_4$	phos	12.8	1.3	4.2	0.8	7.1	7.4	24.1
$MgFe_2O_4$	phos	6.2	0.7	7.9	1.5	11.1	12.8	25.2
$NiFe_2O_4$	betaine	1.8	0.3	13.0	2.2	0.5	0.5	15.3
	phos	14.1	1.7	4.5	0.9	7.8	9.4	26.4

to the overall very good colloidal stability, also proved by a positive zeta-potential of the betaine stabilized ferrite nanoparticles. It has to be remarked here, that the obtained TOC values for betaine stabilized cobalt and nickel ferrite nanoparticles obtained from the CHN analysis (TOC^{CHN}) is ca. 11 wt% lower than in the TGA analysis. Also, the water contents derived by the two different methods deviate. The latter especially, can be attributed to uncertainties by the determination of the water content in TGA analysis, as the evaporation of water and organics is not strictly divided by a certain temperature but overlaps. The differences in the TOC may stem from the different atmosphere during the measurements. Whereas in TGA an argon atmosphere is used to prevent the spinel ferrite nanoparticles from further oxidation and thus from increasing mass, CHN analysis is performed in oxygen-rich atmosphere to get an optimal combustion of the organics in the sample. Additionally, another source for uncertainties is that the values shown in Table 19 are mainly based on the nitrogen-content in the sample. As this is the lowest of all achieved values from CHN analysis (< 1 wt%), its determination has the most uncertainties, which continues to all other calculated contents. Nevertheless, the presented combination of TGA with CHN analysis is an innovative approach to quantify the ratio of remaining polyol and stabilizer molecules at spinel ferrite nanoparticles. It can be enhanced to work for all colloidal nanostructures with organic stabilizers, in general.

The amount of phosphocholine at the nanoparticle surface varies between 6.1 and 6.2 wt% for cobalt and magnesium ferrite nanoparticles and 12.8 and 14.1 wt% for zinc and nickel ferrite nanoparticles, respectively. The amount of DEG exceeds the amount of stabilizer for cobalt (8.4 wt% DEG) and magnesium (7.9 wt% DEG) ferrites. For zinc (4.2 wt% DEG) and nickel (4.5 wt% DEG) the amount of DEG is lower. In comparison to the betaine-stabilized spinel ferrite nanoparticles, in all phosphocholine-stabilized nanoparticles ratios of 5.4 – 12.8 wt% H_2O is determined. This may be impacted by the higher amount of stabilizer, which is hygroscopic due to the presence of functional groups like phosphate. The TOC^{CHN} is for all four samples between 19.2 and 26.4 wt% and thus, in the same range than the TOC^{TGA}. Those results confirm the observations made by FT-IR that the stabilizer exchange from DEG to betaine is not as successful as it is with phosphocholine. However, all synthesized nanoparticles show enhanced colloidal stability.

6.2 Colloidal Stability of Aqueous Spinel Ferrite Nanoparticle Dispersions

The analysis of the interactions at the nanoparticle surface in dispersion, which are mainly nanoparticle-solvent, nanoparticle-stabilizer and stabilizer-solvent, requires a high colloidal stability of the nanoparticle dispersions over extended time periods. All necessary investigations need to be conducted in the same colloidal state. Complementary SAXS and DLS studies of aqueous dispersions of the spinel ferrite nanoparticles synthesized in chapter 4.1 proof their outstanding colloidal stability up to 10 months. The results of the DLS study is shown in Table A 15. The nanoparticle dispersions (c = 5 g L^{-1}) were aged at RT for the respective time given in the last column. With the exception of the citrate-stabilized $MgFe_2O_4$ nanoparticles, no type of the spinel ferrite nanoparticles shows an increase in diameter in consideration of the PDI in the studied time period of 2 to 10 months. Additionally, this stability over time is confirmed by SAXS on citrate-stabilized $ZnFe_2O_4$ nanoparticles exemplarily. SAXS measurement of the same nanoparticle dispersion (c = 5 g L^{-1}) were performed 2 days after synthesis and after ageing of that dispersion for 3 months at RT. The SAXS raw data and the fits are shown in Figure 32 A.

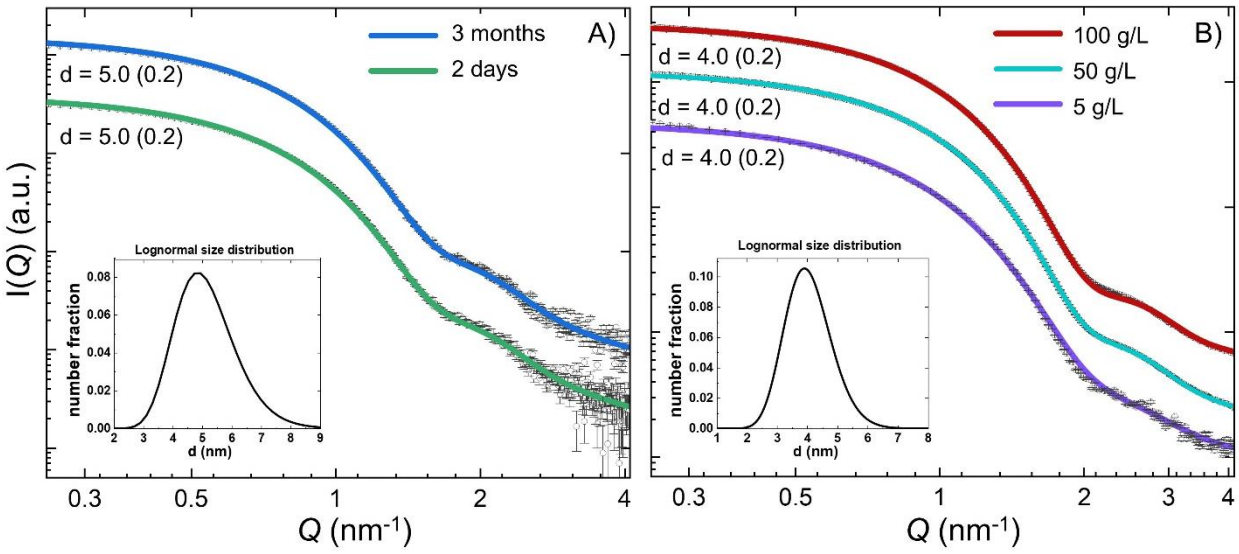

Figure 32: Experimental SAXS data and the corresponding fits of A) aqueous dispersion of citrate-stabilized zinc ferrite nanoparticles (c = 5 g L^{-1}) 2 days after synthesis (green) and the same dispersion aged at RT for 3 months (blue) and of B) aqueous dispersions of phosphocholine-stabilized cobalt ferrite nanoparticles at concentrations of 5 (purple), 50 (light blue) and 100 g L^{-1} (red) aged at RT for 3.5 months. *Curves are scaled for clarity. The insets show the lognormal size distribution, which is equal for all SAXS pattern shown in one graph and thus not graphically visible.*

There is no difference between the two raw data or the fits visible. Even the size distribution resulting from the SAXS fitting is similar, which is shown in the inset in Figure 32 A. Furthermore, SAXS is likely the only analysis method to give directly access to the size distribution of very high concentrated nanoparticle dispersion without any necessary manipulation of the dispersion like, e.g. dilution, before the measurement. Thus, SAXS analysis were performed on 4.0 nm phosphocholine-stabilized cobalt ferrite particles with a PDI of 0.2 for concentrations of 5, 50 and 100 g L^{-1}, aged at RT for 3.5 months. Due to the high density of the particles even the highest concentrations investigated have volume fractions of < 5%. For the fits no structure factor contributions were necessary. Multiple scattering for spherical particle dispersions shows itself by raising the apparent polydispersity with concentration. This was not observed and thus it can be concluded that no significant amount of multiple scattering occurs. The SAXS raw data and the fits are summarized in Figure 32 B. Even at these concentrations, all SAXS fits result in a similar size distribution of the phosphocholine-stabilized $CoFe_2O_4$ nanoparticles. Though, at high *Q*-values the SAXS data and fit of the 5 g L^{-1} sample deviates slightly from the data and fit of the higher concentrations. However, the influence on the size distribution calculation may be rather negligible. This result highlights the remarkable colloidal stability of the stabilized spinel ferrite nanoparticles in aqueous dispersion synthesized by the polyol route in DEG and proofs their suitability for the following studies of the surface interactions in nanoparticle dispersions.

6.3 Hydration Shells around Spinel Ferrite Nanoparticles

The existence of a surface-coordinated shell of water molecules is already suggested by the size determination via DLS (Table 10). The obtained diameters for the different spinel ferrite nanoparticles are on average 1.4 nm larger than diameters from SAXS analysis. This deviation is based on the different characterization principle of the two methods. In DLS analysis, the diameter is determined with a 660 nm laser via the scattering difference over time and thus, via the motion of the nanoparticles. The shell of solvent molecules moves with the nanoparticle in this Brownian motion. This characterization results in the hydrodynamic diameter, including the size of the hydration shell.[134] Whereas SAXS is based on the electron density difference between the solvent and the inorganic nanoparticle, yielding the inorganic diameter (Figure 33).[149-150] The size of the hydration shells based on differences between DLS and SAXS diameters are summarized in Table 20.

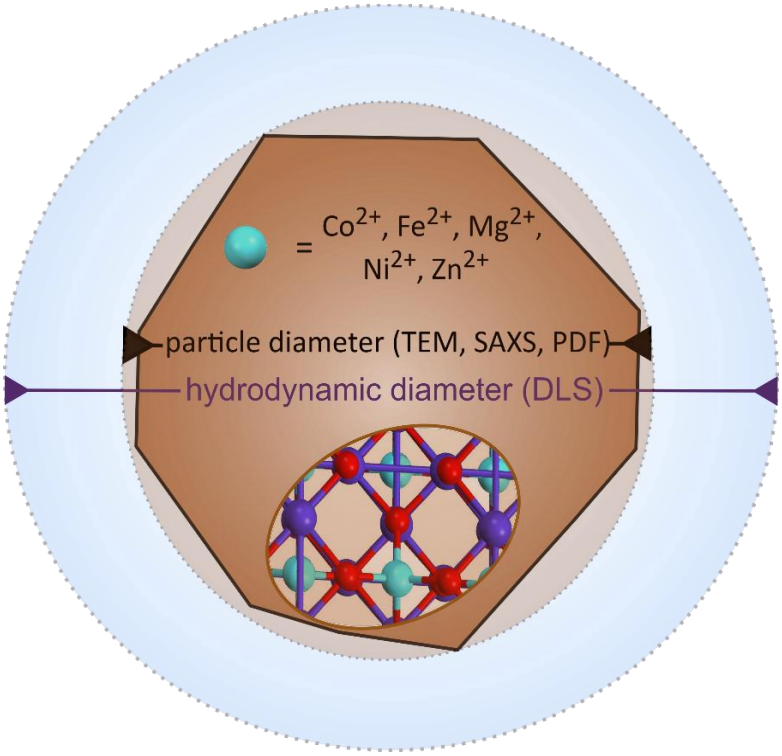

Figure 33: Schematic figure of a dispersed nanoparticle with the obtained particle diameter by different characterization methods. *The light brown circle around the facetted nanoparticle clarifies the assumption of a spherical shape by the used analysis and the light blue circle shows the surrounding solvation shell, which is included in the hydrodynamic diameter obtained by DLS.*[7]

Table 20: Size of the solvation shell around different spinel ferrite nanoparticles based on the difference between the diameters obtained from DLS and SAXS (Table 10). *It is calculated by ($d_{DLS} - d_{SAXS}$)/2. The average size of the hydration shell per nanoparticle composition and stabilizer is calculated to investigate trends. The average size of the nanoparticles is given to see size-dependency.*

	$\bar{d}$ (NP)$_{SAXS}$	citrate	betaine	phos	average
$CoFe_2O_4$	3.7 nm	0.5 nm	0.3 nm	0.3 nm	0.4 nm
$MgFe_2O_4$	3.0 nm	1.0 nm	1.2 nm	1.1 nm	1.1 nm
$NiFe_2O_4$	3.4 nm	1.0 nm	1.0 nm	0.7 nm	0.9 nm
$ZnFe_2O_4$	4.5 nm	0.4 nm	0.8 nm	0.4 nm	0.5 nm
average		0.7 nm	0.8 nm	0.6 nm	

The size of hydration shells fluctuates from 0.3 nm for betaine and phosphocholine-stabilized $CoFe_2O_4$ nanoparticles to 1.2 nm for $NiFe_2O_4$ betaine-stabilized nanoparticles. It seems like different stabilizer don't affect the size of the solvation shell, as it is 0.7 nm ± 0.1 nm in average. But for the different composition of the spinel ferrite nanoparticles the size changes. $MgFe_2O_4$ nanoparticles, which are the smallest among the nanoparticles investigated in this study, show the thickest solvation shell (d_{shell} = 1.1 nm). The solvation shell size decreases in the row $NiFe_2O_4$, $ZnFe_2O_4$ and $CoFe_2O_4$. No clear dependency on the nanoparticle diameter can be revealed. However, as the two largest nanoparticles show the smallest solvation shell size and the smallest nanoparticles show the largest solvation shell size, a dependency on the nanoparticle diameter can be assumed. It is known that the attraction of water molecules varies with the nature of the crystal facets at the nanoparticle-water interface.[4] Eventually, the ratio of the different crystal facets is different depending on the nanoparticle diameter and the nature of the M^{2+} ion.

It has to be remarked that due to the lognormal particle size distribution and uncertainties in the determination of the particle diameter, resp. hydrodynamic particle diameter, a certain inaccuracy for the size of the solvation shell exists. Consequently, XRD and PDF experiments were performed. However, only synchrotron radiation provides enough brilliance (Equation A11) to extract the small signal of the hydration shell, which is overlapped by the scattering signal of the solvent and the nanoparticles.

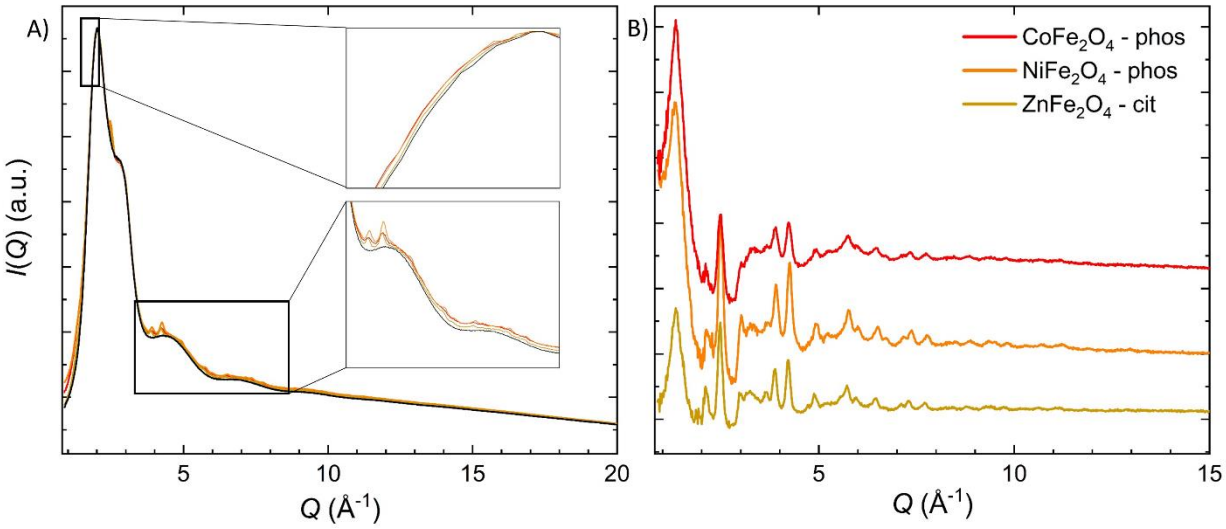

Figure 34: A) Normalized XRD patterns of water (black) and aqueous dispersions of phosphocholine-stabilized $CoFe_2O_4$ (red) and $NiFe_2O_4$ (orange) as well as citrate-stabilized $ZnFe_2O_4$ nanoparticles. *The insets highlight the small shift in the FSDP originating from the hydration shell and the XRD reflections of the dispersed crystalline nanoparticles.* ***B) Difference-I(Q) plots calculated by subtraction of the water background****. The concentration of the pure inorganic nanomaterial ranges from 4 – 5 wt%.*

The XRD pattern of the nanoparticle dispersions and pure water, collected at ID31, ESRF, are presented in Figure 34 A. The reflections of the crystalline nanoparticles are still visible on top of the pattern of the water background. Small shifts to the left flank of the first sharp diffraction peak (FSDP) of water may originate from the restructured H_2O molecules at the nanoparticle surface. After subtraction of the water signal, the d-$I(Q)$ (difference-$I(Q)$, Figure 34 B) highlights the signal from the nanoparticles and the hydration shell. Due to the shift of the FSDP, the information about the hydration shells is contained in the maximum at $Q \approx 1.5$ Å^{-1} in the d-$I(Q)$. In the XRD, the intensity of the hydration shell is higher for the two phosphocholine-stabilized nanoparticles than for the citrate stabilized nanoparticles. This could probably indicate a stabilizer dependency of the restructuring effect. The scattering signal of the stabilizer molecules can be neglected, as not coordinated and possibly crystalline residuals of stabilizers are removed by dialysis and thus, the intensity is very small. By Fourier-Transformation of the scattering data into the PDF data, the structure of the hydration shells around the spinel ferrite nanoparticles can be further investigated.

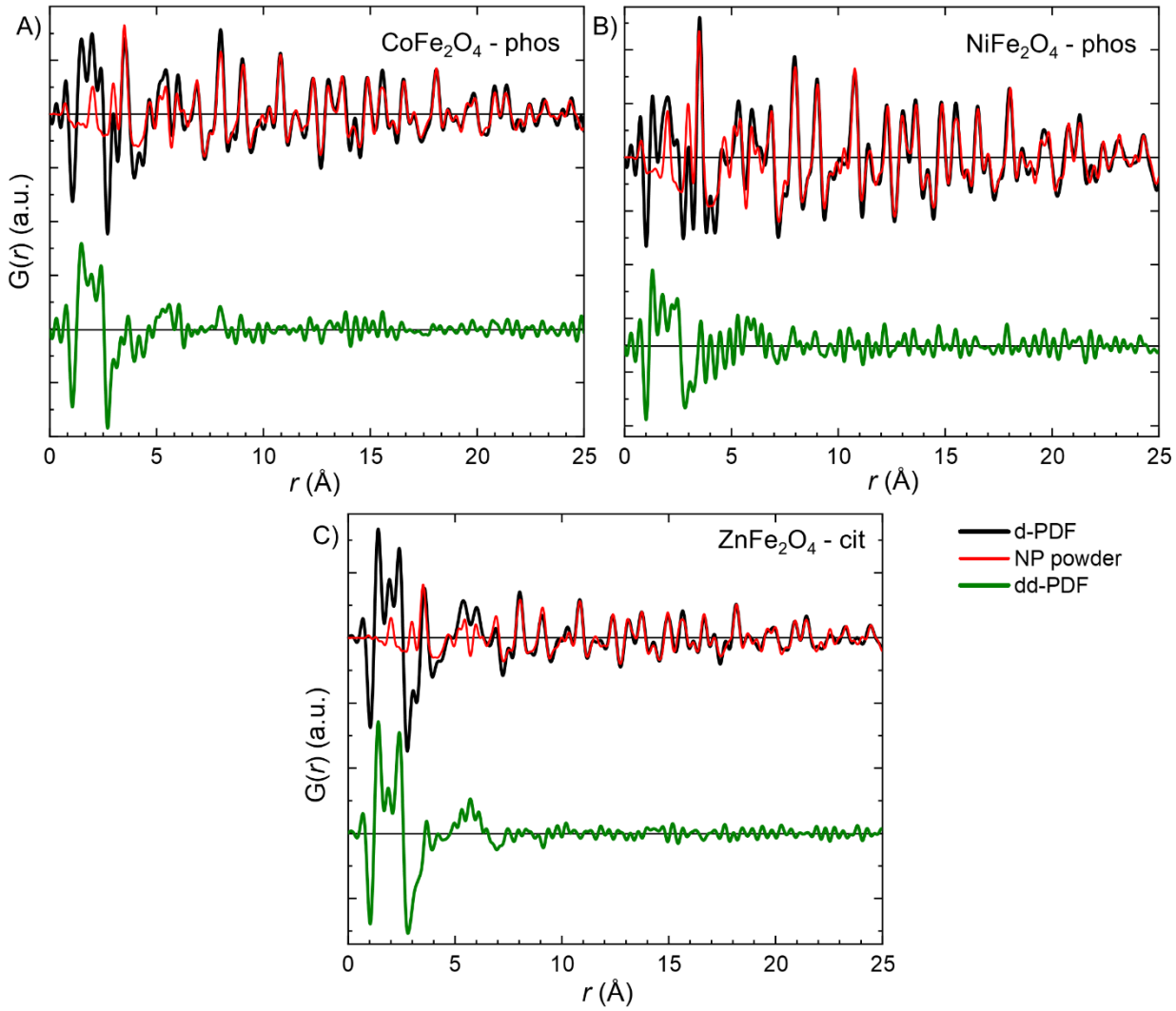

Figure 35: Graphs of the d-PDF (black), the scaled PDF of the nanoparticle powders (red) and the corresponding dd-PDF (green) for A) phosphocholine-stabilized $CoFe_2O_4$, B) phosphocholine-stabilized $NiFe_2O_4$ and C) citrate-stabilized $ZnFe_2O_4$ nanoparticle dispersions. *The dd-PDFs are plotted in offset for clarity. The blue circle highlights the PDF peaks at r ≈ 18 Å, which was used as scaling benchmark.*

Besides the water background and the nanoparticle dispersions, the pure nanoparticle powder was also measured with the same parameters at the same beamline. First, the d-PDF (difference-PDF) is calculated by subtracting the pure solvent from the dispersion intensity. The experimental PDF of the nanopowder is then scaled to the d-PDF. The peak at $r \approx 18$ Å was chosen as a scaling benchmark, because at this distance, no signal of the hydration shell is expected to occur and only the nanoparticle signal contributes to the PDF signal. The scaled PDF of the nanoparticles is then subtracted from the d-PDF resulting in the dd-PDF (double-difference-PDF), which contains all the information about the restructured water molecules. Figure 35 illustrates the above mentioned

implementation. The resulting green plot for the dd-PDF contains the structural information of the hydration shell. Between r = 1.0 to 3.0 the distance from the nanoparticle surface to adsorbed water species is visible. According to Kerisit et al., two of the observed peaks can be attributed to specific water species. These are dissociatively bound OH^- ($r \approx 1.47$ Å) and molecular adsorbed H_2O interacting with the surface iron sites ($r \approx 2.32$ Å).[4] The maxima of the three distances extracted from the dd-PDF are summarized in Table 21.

Table 21: Summary of the position of the maxima of the adsorbed water species at the surface of the three investigated spinel ferrite nanoparticles.

sample	1. peak (Å)	2. peak (Å)	3. peak (Å)
$CoFe_2O_4$ - phos	1.47	1.90	2.41
$NiFe_2O_4$ – phos	1.30	1.78	2.30*
$ZnFe_2O_4$ - cit	1.42	1.91	2.40

* directly next to this peak exists a ripple originating from the Fourier transformation, which probably impacts the position of the maximum.

While the positions of the first three peaks in the dd-PDF of $CoFe_2O_4$ and $ZnFe_2O_4$ nanoparticles are very similar to the literature, the distances for the $NiFe_2O_4$ nanoparticles deviates clearly. In average, all distances are 0.12 Å shorter for the nickel ferrite nanoparticles than for the other two nanoparticles. This effect could probably be induced by the substitution of the Fe^{2+} by Ni^{2+} cations. For $NiFe_2O_4$ a lower energy barrier for the dissociative adsorption of OH^- in comparison to Fe_3O_4 surfaces is reported.[50] In contrast to the study on ZnO nanoparticles by Zobel et al.[27], a defined oscillation in the dd-PDF signal is only implied and most pronounced in the $ZnFe_2O_4$ sample. However, the presence of EtOH in the nanoparticle dispersions similar to Thomä et al. was not excluded and must be made up to verify the interpretation of the dd-PDF signals.[28] All above presented spinel ferrite nanoparticles are smaller in diameter and their crystallinity is less evolved, shown with XRD analysis. This leads to inconsistent surface termination of the crystal structure and to diverse or even weaker coordination of the water molecules to the surface metal atoms. Furthermore, the presence of the stabilizers with a grafting density ρ^{graft} of 3.2 and 4.4 nm^{-2} for phosphocholine stabilized cobalt and nickel ferrite nanoparticles, respectively, and 3.9 nm^{-2} for citrate stabilized zinc ferrite nanoparticles

(see Table 18) may hinder the restructuring of the water molecules at the nanoparticle surface. As mentioned in chapter 6.1, a ρ^{graft} of 4.3 nm^{-2} corresponds to a monolayer of stabilizer molecules with carboxyl anchor groups. In this case, citrate seems to support the formation of the solvation shell more than phosphocholine, as the dd-PDF of the citrate stabilized zinc ferrite nanoparticles in water contains the indication of an oscillation with the first maximum at ca. 5.8 Å. For further studies, the influence of ethanol molecules onto the dd-PDF analysis must be excluded and measurements of at least the complete series of synthesized spinel ferrite nanoparticles are needed to obtain a sophisticated study on the restructuring behavior of water molecules at spinel ferrite nanoparticles.

References

[1] J. van Embden, A. S. R. Chesman, J. J. Jasieniak, *Chem. Mater.* **2015**, *27*, 2246-2285.

[2] M. Niederberger, G. Garnweitner, *Chem. Eur. J.* **2006**, *12*, 7282-7302.

[3] V. K. LaMer, R. H. Dinegar, *JACS* **1950**, *72*, 4847-4854.

[4] S. Kerisit, D. J. Cooke, D. Spagnoli, S. C. Parker, *J. Mater. Chem.* **2005**, *15*.

[5] D. Caruntu, Y. Remond, N. H. Chou, M.-J. Jin, G. Caruntu, J. He, G. Goloverda, C. O'Connor, V. Kolesnichenko, *Inorg. Chem.* **2002**, *41*, 6137-6146.

[6] S. R. Cooper, R. O. Candler, A. G. Cosby, D. W. Johnson, K. M. O. Jensen, J. E. Hutchison, *ACS Nano* **2020**, *14*, 5480-5490.

[7] M. Eckardt, S. L. J. Thomä, M. Dulle, G. Hörner, B. Weber, S. Förster, M. Zobel, *ChemistryOpen* **2020**, *9*, 1214-1220.

[8] K. Zarschler, L. Rocks, N. Licciardello, L. Boselli, E. Polo, K. P. Garcia, L. De Cola, H. Stephan, K. A. Dawson, *Nanomedicine* **2016**, *12*, 1663-1701.

[9] N. Lee, D. Yoo, D. Ling, M. H. Cho, T. Hyeon, J. Cheon, *Chem. Rev.* **2015**, *115*, 10637-10689.

[10] E. Amstad, T. Gillich, I. Bilecka, M. Textor, E. Reimhult, *Nano Lett.* **2009**, *9*, 4042-4048.

[11] S. Kamali, M. Pouryazdan, M. Ghafari, M. Itou, M. Rahman, P. Stroeve, H. Hahn, Y. Sakurai, *J. Magn. Magn. Mater.* **2016**, *404*, 143-147.

[12] S. W. Charles, J. Popplewell in *Handbook of Ferromagnetic Materials, Vol. 2* (Ed.: E. P. Wohlfarth), Elsevier, North Holland, **1980**, pp. 509-559.

[13] E. Casbeer, V. K. Sharma, X.-Z. Li, *Sep. Purif. Technol.* **2012**, *87*, 1-14.

[14] K. Kirchberg, A. Becker, A. Bloesser, T. Weller, J. Timm, C. Suchomski, R. Marschall, *J. Phys. Chem. C* **2017**, *121*, 27126-27138.

[15] S. Chandrasekaran, C. Bowen, P. Zhang, Z. Li, Q. Yuan, X. Ren, L. Deng, *Journal of Materials Chemistry A* **2018**, *6*, 11078-11104.

[16] S. Anke, T. Falk, G. Bendt, I. Sinev, M. Hävecker, H. Antoni, I. Zegkinoglou, H. Jeon, A. Knop-Gericke, R. Schlögl, et al., *J. Catal.* **2020**, *382*, 57-68.

[17] A. El Arrassi, Z. Liu, M. V. Evers, N. Blanc, G. Bendt, S. Saddeler, D. Tetzlaff, D. Pohl, C. Damm, S. Schulz, et al., *J. Am. Chem. Soc.* **2019**, *141*, 9197-9201.

[18] H. Hajiyani, R. Pentcheva, *ACS Catalysis* **2018**, *8*, 11773-11782.

[19] A. H. Lu, E. L. Salabas, F. Schuth, *Angew. Chem. Int. Ed. Engl.* **2007**, *46*, 1222-1244.

[20] A. L. Tiano, G. C. Papaefthymiou, C. S. Lewis, J. Han, C. Zhang, Q. Li, C. Shi, A. M. M. Abeykoon, S. J. L. Billinge, E. Stach, et al., *Chem. Mater.* **2015**, *27*, 3572-3592.

[21] C. Nordhei, A. L. Ramstad, D. G. Nicholson, *Phys. Chem. Chem. Phys.* **2008**, *10*, 1053-1066.

[22] S. R. Cooper, L. K. Plummer, A. G. Cosby, P. Lenox, A. Jander, P. Dhagat, J. E. Hutchison, *Chem. Mater.* **2018**, *30*, 6053-6062.

[23] C. Pereira, A. M. Pereira, C. Fernandes, M. Rocha, R. Mendes, M. P. Fernández-García, A. Guedes, P. B. Tavares, J.-M. Grenèche, J. P. Araújo, et al., *Chem. Mater.* **2012**, *24*, 1496-1504.

[24] D. Spagnoli, B. Gilbert, G. A. Waychunas, J. F. Banfield, *Geochim. Cosmochim. Acta* **2009**, *73*, 4023-4033.

[25] H. Liu, P. Siani, E. Bianchetti, J. Zhao, C. Di Valentin, *Nanoscale* **2021**.

[26] R. B. N. M. Zobel, S.A.J. Kimber, *Science* **2015**, *347*, 292-294.

[27] M. Zobel, *Acta Crystallogr A Found Adv* **2016**, *72*, 621-631.

[28] S. L. J. Thoma, M. Zobel, *J. Chem. Phys.* **2023**, *158*.

[29] D. Spagnoli, J. P. Allen, S. C. Parker, *Langmuir* **2011**, *27*, 1821-1829.

[30] T. Shahjuee, S. M. Masoudpanah, S. M. Mirkazemi, *Journal of Superconductivity and Novel Magnetism* **2018**, *32*, 1347-1352.

[31] P. Dolcet, K. Kirchberg, A. Antonello, C. Suchomski, R. Marschall, S. Diodati, R. Muñoz-Espí, K. Landfester, S. Gross, *Inorganic Chemistry Frontiers* **2019**, *6*, 1527-1534.

[32] S. Chkoundali, S. Ammar, N. Jouini, F. Fiévet, P. Molinié, M. Danot, F. Villain, J. M. Grenèche, *J. Phys.: Condens. Matter* **2004**, *16*, 4357-4372.

[33] A. Mary Jacintha, V. Umapathy, P. Neeraja, S. Rex Jeya Rajkumar, *Journal of Nanostructure in Chemistry* **2017**, *7*, 375-387.

[34] J. Calvo-de la Rosa, M. Segarra, *ACS Omega* **2019**, *4*, 18289-18298.

[35] A. Debnath, A. Bera, K. K. Chattopadhyay, B. Saha, **2016**.

[36] Q. Song, Z. J. Zhang, *JACS* **2004**, 6164-6168.

[37] L. Néel, *Journal de Physique et le Radium* **1950**, *11*, 49-61.

[38] K. E. Sickafus, J. M. Wills, N. W. Grimes, *J. Am. Ceram. Soc.* **1999**, *82*, 3279-3292.

[39] T. N. Pham, T. Q. Huy, A.-T. Le, *RSC Advances* **2020**, *10*, 31622-31661.

[40] M. Qin, Q. Shuai, G. Wu, B. Zheng, Z. Wang, H. Wu, *Materials Science and Engineering: B* **2017**, *224*, 125-138.

[41] A. Shan, X. Wu, J. Lu, C. Chen, R. Wang, *CrystEngComm* **2015**, *17*, 1603-1608.

[42] P. D. Thang, G. Rijnders, D. H. A. Blank, *J. Magn. Magn. Mater.* **2005**, *295*, 251-256.

[43] M. E. Fleet, *Acta Cryst.* **1981**, *B37*, 917-920.

[44] I. Bergmann, V. Sepelak, K. Becker, *Solid State Ionics* **2006**, *177*, 1865-1868.

[45] H. L. Andersen, M. Saura-Muzquiz, C. Granados-Miralles, E. Canevet, N. Lock, M. Christensen, *Nanoscale* **2018**, *10*, 14902-14914.

[46] R. H. Kodama, A. E. Berkowitz, E. J. McNiff, S. Foner, *J. Appl. Phys.* **1997**, *81*, 5552-5557.

[47] H. Qu, D. Caruntu, H. Liu, C. J. O'Connor, *Langmuir* **2011**, *27*, 2271-2278.

[48] S. Ammar, A. Helfen, N. Jouini, F. Fiévet, I. Rosenman, F. Villain, P. Molinié, M. Danot, *J. Mater. Chem.* **2001**, *11*, 186-192.

[49] Q. Li, C. W. Kartikowati, S. Horie, T. Ogi, T. Iwaki, K. Okuyama, *Sci Rep* **2017**, *7*, 9894.

[50] P. V. Kumar, M. P. Short, S. Yip, B. Yildiz, J. C. Grossman, *J. Phys. Chem. C* **2013**, *117*, 5678-5683.

[51] F. Fiévet, R. Brayner in *Nanomaterials: A Danger or a Promise?* (Ed.: F. F. R. Brayner, T. Coradin), Springer, London, **2013**, pp. 1-25.

[52] P.-Y. Silvert, K. Tekaia-Elhsissen, *Solid State Ion.* **1995**, *82*, 53-60.

[53] F. F.-V. Fiévet, F.; Lagier, J.-P.; Dumont, B.; Figlarz, M., *J. Mater. Chem.* **1993**, *3*, 627-632.

[54] C. U. Ducamp-Sanguesa, R.H.; Figlarz, M., *J. Solid State Chem.* **1992**, *100*, 272-280.

[55] Y. Sun, Y. Xia, *Science* **2002**, *298*, 2176-2179.

[56] Y. Sun, Y. Yin, B. T. Mayers, T. Herricks, Y. Xia, *Chem. Mater.* **2002**, *14*, 4736-4745.

[57] C. Feldmann, *Adv. Funct. Mater.* **2003**, *13*, 101-107.

[58] M. Shaikh, M. Sahu, K. K. Atyam, K. V. S. Ranganath, *RSC Advances* **2016**, *6*, 76795-76801.

[59] E. Amstad, M. Textor, E. Reimhult, *Nanoscale* **2011**, *3*, 2819-2843.

[60] R. P. Singh, K. Sharma, K. Mausam, *Materials Today: Proceedings* **2020**, *26*, 2021-2025.

[61] A. Heuer-Jungemann, N. Feliu, I. Bakaimi, M. Hamaly, A. Alkilany, I. Chakraborty, A. Masood, M. F. Casula, A. Kostopoulou, E. Oh, et al., *Chem. Rev.* **2019**, *119*, 4819-4880.

[62] M. Vasilakaki, N. Ntallis, N. Yaacoub, G. Muscas, D. Peddis, K. N. Trohidou, *Nanoscale* **2018**, *10*, 21244-21253.

[63] D. Cabrera, J. Camarero, D. Ortega, F. J. Teran, *J. Nanopart. Res.* **2015**, *17*, 121.

[64] D. Caruntu, G. Caruntu, Y. Chen, C. J. O'Connor, G. Goloverda, V. L. Kolesnichenko, *Chem. Mater.* **2004**, *16*, 5527-5534.

[65] G. Baldi, D. Bonacchi, M. C. Franchini, D. Gentili, G. Lorenzi, A. Ricci, C. Ravagli, *Langmuir* **2007**, *23*, 4026-4028.

[66] J. Fan, J. Lu, R. Xu, R. Jiang, Y. Gao, *J. Colloid Interface Sci.* **2003**, *266*, 215-218.

[67] A. Hajdú, E. Illés, E. Tombácz, I. Borbáth, *Colloids Surf., A* **2009**, *347*, 104-108.

[68] A. M. Smith, K. A. Johnston, S. E. Crawford, L. E. Marbella, J. E. Millstone, *Analyst* **2016**, *142*, 11-29.

[69] M. Günay, H. Erdemi, A. Baykal, H. Sözeri, M. S. Toprak, *Mater. Res. Bull.* **2013**, *48*, 1057-1064.

[70] D. Lisjak, A. Mertelj, *Prog. Mater Sci.* **2018**, *95*, 286-328.

[71] R. G. D. Andrade, S. R. S. Veloso, E. M. S. Castanheira, *Int J Mol Sci* **2020**, *21*.

[72] K.-K. Kang, B. Lee, C.-S. Lee, *Journal of the Taiwan Institute of Chemical Engineers* **2019**, *98*, 2-19.

[73] A. K. Pearce, T. R. Wilks, M. C. Arno, R. K. O'Reilly, *Nature Reviews Chemistry* **2020**, *5*, 21-45.

[74] P. M. R. H. Zeng, S.X. Wang, S. Sun, *J. Am. Chem. Soc.* **2004**, *126*, 11458-11459.

[75] Q. Song, Z. J. Zhang, *J. Am. Chem. Soc.* **2004**, *126*, 6164-6168.

[76] S. Lalwani, R. B. Marichi, M. Mishra, G. Gupta, G. Singh, R. K. Sharma, *Electrochim. Acta* **2018**, *283*, 708-717.

[77] G. B. Ji, S. L. Tang, S. K. Ren, F. M. Zhang, B. X. Gu, Y. W. Du, *J. Cryst. Growth* **2004**, *270*, 156-161.

[78] Q. A. Pankhurst, J. Connolly, S. K. Jones, J. Dobson, *J. Phys. D: Appl. Phys.* **2003**, *36*, R167-R181.

[79] J. H. Lee, Y. M. Huh, Y. W. Jun, J. W. Seo, J. T. Jang, H. T. Song, S. Kim, E. J. Cho, H. G. Yoon, J. S. Suh, et al., *Nat Med* **2007**, *13*, 95-99.

[80] C. A. Quinto, P. Mohindra, S. Tong, G. Bao, *Nanoscale* **2015**, *7*, 12728-12736.

[81] C. B. de Boer, M. J. Dekkers, *Geophysical Research Letters* **1996**, *23*, 2815-2818.

[82] A. N. Shmakov, G. N. Kryukova, S. V. Tsybulya, A. L. Chuvilin, L. P. Solovyeva, *J. Appl. Crystallogr.* **1995**, *28*, 141-145.

[83] C. Greaves, *J. Solid State Chem.* **1983**, *49*, 325-333.

[84] J.-E. Jørgensen, L. Mosegaard, L. E. Thomsen, T. R. Jensen, J. C. Hanson, *J. Solid State Chem.* **2007**, *180*, 180-185.

[85] H. L. Andersen, B. A. Frandsen, H. P. Gunnlaugsson, M. R. V. Jørgensen, S. J. L. Billinge, K. M. Ø. Jensen, M. Christensen, *IUCrJ* **2021**, *8*, 33-45.

[86] V. Petkov, *Mater. Today* **2008**, *11*, 28-38.

[87] R. B. Neder, V. I. Korsunskiy, *J. Phys.: Condens. Matter* **2005**, *17*, S125-S134.

[88] S. J. Billinge, M. G. Kanatzidis, *Chem. Commun.* **2004**, 749-760.

[89] B. H. Toby, T. Egami, *Acta Coest* **1992**, *A48*, 336-346.

[90] T. Egami, S. J. L. Billinge, *Underneath the Bragg Peaks, Vol. 16*, 2nd ed., Elsevier, London, **2012**.

[91] A. K. Soper, E. R. Barney, *J. Appl. Crystallogr.* **2012**, *45*, 1314-1317.

[92] S. J. L. B. T. Proffen, T. Egami, D. Louca, *Z. Kristallogr.* **2003**, *218*, 132-143.

[93] M. Polyanskiy, *Refractive index database* **2020**, *www.refractiveindex.info/*.

[94] http://www.sasview.org/, **09.02.2023**.

[95] R. Biehl, *PLoS One* **2019**, *14*, e0218789.

[96] S. L. J. Thomae, N. Prinz, T. Hartmann, M. Teck, S. Correll, M. Zobel, *Rev. Sci. Instrum.* **2019**, *90*, 043905.

[97] X. Yang, C. L. Farrow, P. Juhas, S. J. L. Billinge, *J. Appl. Crystallogr.* **2014**, arXiv:1402.3163.

[98] P. Juhas, C. L. Farrow, X. Yang, K. R. Knox, S. J. Billinge, *Acta Crystallogr A Found Adv* **2015**, *71*, 562-568.

[99] C. L. Farrow, P. Juhas, J. W. Liu, D. Bryndin, E. S. Bozin, J. Bloch, T. Proffen, S. J. Billinge, *J. Phys.: Condens. Matter* **2007**, *19*, 335219.

[100] P. Cheah, T. Cowan, R. Zhang, A. Fatemi-Ardekani, Y. Liu, J. Zheng, F. Han, Y. Li, D. Cao, Y. Zhao, *Nanoscale* **2020**, *12*, 9272-9283.

[101] N. T. Thanh, N. Maclean, S. Mahiddine, *Chem. Rev.* **2014**, *114*, 7610-7630.

[102] A. Kmita, D. Lachowicz, J. Zukrowski, M. Gajewska, W. Szczerba, J. Kuciakowski, S. Zapotoczny, M. Sikora, *Materials* **2019**, *12*.

[103] J. H. C. M. Doucet, G. Alina, J. Bakker, W. Bouman, P. Butler, K. Campell, T. Cooper-Benun, C. Durniak, L. Forster, et al., **2019**.

[104] S. Sun, H. Zeng, D. B. Robinson, S. Raoux, P. M. Rice, S. X. Wang, G. Li, *J. Am. Chem. Soc.* **2004**, *126*, 273-279.

[105] S. Ammar, N. Jouini, F. Fiévet, O. Stephan, C. Marhic, M. Richard, F. Villain, C. Cartier dit Moulin, S. Brice, P. Sainctavit, *J. Non-Cryst. Solids* **2004**, *345-346*, 658-662.

[106] S. Ammar, N. Jouini, F. Fiévet, Z. Beji, L. Smiri, P. Moliné, M. Danot, J.-M. Grenèche, *J. Phys.: Condens. Matter* **2006**, *18*, 9055-9069.

[107] T. D. Nguyen, *Nanoscale* **2013**, *5*, 9455-9482.

[108] A. K. Singh, O. N. Srivastava, K. Singh, *Nanoscale Res Lett* **2017**, *12*, 298.

[109] A. G. Roca, L. Gutierrez, H. Gavilan, M. E. Fortes Brollo, S. Veintemillas-Verdaguer, M. D. P. Morales, *Adv Drug Deliv Rev* **2019**, *138*, 68-104.

[110] N. Bao, L. Shen, Y. H. Wang, J. Ma, D. Mazumdar, A. Gupta, *J. Am. Chem. Soc.* **2009**, *131*, 12900-12901.

[111] M. Danaei, M. Dehghankhold, S. Ataei, F. Hasanzadeh Davarani, R. Javanmard, A. Dokhani, S. Khorasani, M. R. Mozafari, *Pharmaceutics* **2018**, *10*.

[112] R. M. Z. Lui, M. Osada, K. Takada, T. Sasaki, *J. Am. Chem. Soc.* **2005**, *127*, 13869-13874.

[113] A. V. Radha, S. Weiss, I. Sanjuan, M. Ertl, C. Andronescu, J. Breu, *Chemistry* **2021**.

[114] T. M. Usher, D. Olds, J. Liu, K. Page, *Acta Crystallogr A Found Adv* **2018**, *74*, 322-331.

[115] T. Kodama, Y. Tamaura, *J. Am. Ceram. Soc.* **1995**, *78*, 1335-1342.

[116] N. Pathak, S. K. Gupta, K. Sanyal, M. Kumar, R. M. Kadam, V. Natarajan, *Dalton Trans* **2014**, *43*, 9313-9323.

[117] X. Liang, Y. Zhong, S. Zhu, H. He, P. Yuan, J. Zhu, Z. Jiang, *Solid State Sciences* **2013**, *15*, 115-122.

[118] R. M. Cornell, U. Schwertmann, *The Iron Oxides: Structure, Properties, Reactions, Occurrences and Uses*, Wiley-VCH Verlag GmbH, Weinheim, **2003**.

[119] S. Rosenfeldt, S. Förster, T. Friedrich, I. Rehberg, B. Weber in *Novel Magnetic Nanostructures* (Eds.: N. Domracheva, M. Caporali, E. Rentschler), Elsevier, Amsterdam, **2018**, pp. 165-189.

[120] K. Zhang, T. Holloway, A. K. Pradhan, *J. Magn. Magn. Mater.* **2011**, *323*, 1616-1622.

[121] S. Zawar, S. Atiq, S. Riaz, S. Naseem, *Superlattices Microstruct.* **2016**, *93*, 50-56.

[122] V. Šepelák, I. Bergmann, D. Menzel, A. Feldhoff, P. Heitjans, F. J. Litterst, K. D. Becker, *J. Magn. Magn. Mater.* **2007**, *316*, e764-e767.

[123] L. S. N. Bao, Y. Wang, P. Padhan, A. Gupta, *J. Am. Chem. Soc.* **2007**, *129*, 12374–12375.

[124] H. Annersten, S. S. Hafner, *Zeitschrift für Kristallographie* **1973**, *137*, 321-340.

[125] C. de Alwis, T. R. Leftwich, P. Mukherjee, A. Denofre, K. A. Perrine, *Nanoscale Advances* **2019**, *1*, 4729-4744.

[126] M. Augustin, D. Fenske, I. Bardenhagen, A. Westphal, M. Knipper, T. Plaggenborg, J. Kolny-Olesiak, J. Parisi, *Beilstein J Nanotechnol* **2015**, *6*, 47-59.

[127] U. Topal, M. A. Aksan, *J. Magn. Magn. Mater.* **2016**, *406*, 123-128.

[128] F. Al-Mokdad, R. S. Hassan, R. Awad, *Current Nanomaterials* **2019**, *4*, 125-136.

[129] C. Simon, A. Blösser, M. Eckardt, H. Kurz, B. Weber, M. Zobel, R. Marschall, *Z. Anorg. Allg. Chem.* **2021**, *647*, 2061-2072.

[130] K. Chakrapani, G. Bendt, H. Hajiyani, T. Lunkenbein, M. T. Greiner, L. Masliuk, S. Salamon, J. Landers, R. Schlögl, H. Wende, et al., *ACS Catalysis* **2018**, *8*, 1259-1267.

[131] K. Chakrapani, G. Bendt, H. Hajiyani, I. Schwarzrock, T. Lunkenbein, S. Salamon, J. Landers, H. Wende, R. Schlögl, R. Pentcheva, et al., *ChemCatChem* **2017**, *9*, 2988-2995.

[132] Y. Xu, F. Özcan, P. Zielke, S. Becker, M. Heimann, J. Heese, K. Chakrapani, M. Behrens, S. Bredmose Simonsen, P. Norby, et al., *Z. Anorg. Allg. Chem.* **2018**, *644*, 1727-1733.

[133] H. G. Hertz, *Angew. Chem. Int. Ed.* **1970**, *9*, 124-138.

[134] C. Bellmann, A. Caspari, C. Moitzi, F. Babick, M. Stintz, M. Schäffler, T. Luxbacher, C. Fradler, *Dynamische und Elektrophoretische Lichtstreuung: Leitfaden Zur Partikelgrößenanalyse und Zetapotenzialbestimmung*, Anton Paar, Graz, **2018**.

[135] A. J. Shnoudeh, I. Hamad, R. W. Abdo, L. Qadumii, A. Y. Jaber, H. S. Surchi, S. Z. Alkelany in *Biomaterials and Bionanotechnology* (Ed.: R. K. Tekade), Academic Press, **2019**, pp. 527-612.

[136] S. Samimi, N. Maghsoudnia, R. B. Eftekhari, F. Dorkoosh in *Characterization and Biology of Nanomaterials for Drug Delivery* (Ed.: S. R. Shyam S. Mohapatra, Nandita Dasgupta, Raghvendra Kumar Mishra, Sabu Thomas), Elsevier, **2019**, pp. 47-76.

[137] T. Milek, D. Zahn, *Z. Anorg. Allg. Chem.* **2016**, *642*, 902-905.

[138] K. V. Korpany, D. D. Majewski, C. T. Chiu, S. N. Cross, A. S. Blum, *Langmuir* **2017**, *33*, 3000-3013.

[139] M. R. Noerpel, J. J. Lenhart, *J. Colloid Interface Sci.* **2015**, *460*, 36-46.

[140] R. M. Cornell, P. W. Schindler, *Colloid & Polymer Sci.* **1980**, *258*, 1171-1175.

[141] D. R. G. W. Pohle, H. Fritzsche, B. Rattay, C. Selle, H. Binder, H. Böhlig, *J. Mol. Struct.* **2001**, *563-564*, 463-467.

[142] J. T. Jang, H. Nah, J. H. Lee, S. H. Moon, M. G. Kim, J. Cheon, *Angew. Chem. Int. Ed. Engl.* **2009**, *48*, 1234-1238.

[143] S. Mohapatra, P. Pramanik, *Colloids Surf., A* **2009**, *339*, 35-42.

[144] J. W. Park, J. S. Shumaker-Parry, *J. Am. Chem. Soc.* **2014**, *136*, 1907-1921.

[145] O. Bixner, A. Lassenberger, D. Baurecht, E. Reimhult, *Langmuir* **2015**, *31*, 9198-9204.

[146] D. N. Benoit, H. Zhu, M. H. Lilierose, R. A. Verm, N. Ali, A. N. Morrison, J. D. Fortner, C. Avendano, V. L. Colvin, *Anal. Chem.* **2012**, *84*, 9238-9245.

[147] D. Santos-Carballal, A. Roldan, R. Grau-Crespo, N. H. de Leeuw, *Phys. Chem. Chem. Phys.* **2014**, *16*, 21082-21097.

[148] J. Jae, G. A. Tompsett, A. J. Foster, K. D. Hammond, S. M. Auerbach, R. F. Lobo, G. W. Huber, *J. Catal.* **2011**, *279*, 257-268.

[149] E. V. M. Kachala, D. Svergun in *Intrinsically Disordered Proteins Studied by NMR Spectroscopy. Advances in Experimental Medicine and Biology, Vol. 870* (Ed.: R. P. I. Felli), Springer, Cham, **2015**.

[150] T. Li, A. J. Senesi, B. Lee, *Chem. Rev.* **2016**, *116*, 11128-11180.

List of Figures

List of Tables

Abbreviations

0D, 1D, 2D, 3D	zero, one, two, three-dimensional
CHN	elemental analysis
cit	citrate
coth	hyperbolic cotangent
d-, dd-PDF	difference-, double-difference-PDF
DEG	diethylene glycol
DLS	dynamic light scattering
e.g.	example given
esp.	especially
ESRF	European synchrotron radiation facility
EtAc	ethyl acetate
FT-IR	Fourier-transform infrared spectroscopy
FWHM	full width at half maximum
ICP-OES	inductively coupled plasma atomic emission spectroscopy
IONP	iron oxide nanoparticle
kcounts	kilo-counts
LDH	layered double hydroxide
LFSE	ligand field stabilization energy
M	molar ; moles per liter
MD	molecular dynamics
mpr	magnetite phase ratio
NMDEA	N-methyldiethanolamine
NP	nanoparticle
Occ_{oct}	occupancy of octahedral sites
PDF	pair distribution function
PDI	polydispersity index
PEG	polyethylene glykol
PETRA	Positron-Elektron-Tandem-Ring-Anlage
phos	phosphocholine

RT	room temperature
SAXS	small angle X-ray scattering
SQUID	superconducting quantum interference device
TEM	transmission electron microscopy
TGA	thermogravimetric analysis
TOC	total organic content
wt%	weight percent
XRD	X-ray diffraction

Symbols

symbol	unit	meaning
c	mol L^{-1}, M, mM	concentration
δ	-	number of vacancies at the octahedral site in the *Fd-3m* crystal structure
E	eV, keV	energy
Fd-3m	-	cubic space group symbol
F(Q)	a.u.	reduced structure function
G(r)	a.u.	
H	Oe	magnetizing field
k_B		Boltzmann constant
λ	nm, Å	wavelength
m	g, mg	mass
M		magnetization
M_S	emu g^{-1}	saturation magnetization
n	mol, mmol	amount of substance
O_{occ}, O_{tet}	-	occupancy of the octahedral and tetrahedral sites
$P4_32_12$	-	tetragonal space group symbol
Q	$Å^{-1}$	wave vector transfer
Q_{max}	$Å^{-1}$	maximum value of wave vector transfer for Fourier Transformation of F(Q)
Q_{min}	$Å^{-1}$	minimum value of wave vector transfer for Fourier Transformation of F(Q)
ρ^{graft}	nm^{-2}	grafting density of stabilizer molecules at a nanoparticle surface
r	Å	radius
R_W	-	R-value; goodness of fit parameter
θ	°	scattering angle
t	s, min, h	time

T	°C, K	temperature
u_{iso}	-	anisotropic atomic displacement factor
μ_{part}	-	(formal) magnetic moment of a single NP
ν	cm^{-1}	wavenumber
V	l, cm^3	volume
ζ	mV	zeta potential
χ^2	-	chi square (goodness-of-fit-factor of PDF refinements)
$z(O)$	-	oxygen position in *Fd-3m* symmetry

Appendix

A.1 Calibration Parameters at two different Beamtimes and the Laboratory PDF Instrument

Table A 1: Calibration parameters of two different beamtimes at PETRA III and ESRF: detector paramters.

beamtime	**λ (Å)**	**sample-detector distance (mm)**	**y-coordinate of the beam center (mm)**	**x-coordinate of the beam center (mm)**	**detector tilt y-axis (°)**	**detector tilt x-axis (°)**	**detector rotation angle (°)**
ID21.1 (PETRA III; Jun 20)	0.1220	387.83	272.80	4.898	0.0002	0.0087	$6*10^{-7}$
ID31 (ESRF; Sep 20)	0.1907	240.51	211.82	242.21	-0.0055	-0.0052	$-3 * 10^{-6}$

Table A 2: Calibration parameters of the laboratory PDF instrument: instrumental resolution.

device	**λ (Å)**	**calibrant**	**q_{damp}**	**q_{broad}**
STOE STADI P Mythen2 4K	0.5594	LaB_6	0.011	0.010

A.2 Nanoparticle Purification

Washing of the spinel ferrite nanoparticles was depending on the behavior of the nanoparticles during washing. For less magnetic samples, e.g. $MgFe_2O_4$, decanting didn't work properly as the nanoparticles sedimented only very slowly. In such cases, the nanoparticles/solvent mixture was centrifuged using 500 mL buckets for 10 min at 3800 rpm. Only if the supernatant was clear, washing was stopped after 3 washing cycles with the same organic solvent. As most of the phosphocholine stabilized samples are dispersible in EtOH, a mixture of EtAc and EtOH (2:1) was used instead of pure EtOH.

Table A 3: Aqueous dispersion media of different stabilized spinel ferrite nanoparticles.

nanoparticle composition	stabilizer	dispersion medium
$CoFe_2O_4$	citrate	H_2O
	betaine	50 mM HCl
	phosphocholine	H_2O
$MgFe_2O_4$	citrate	H_2O
	betaine	50 mM HCl
	phosphocholine	H_2O
$NiFe_2O_4$	citrate	H_2O
	betaine	50 mM HCl
	phosphocholine	H_2O
$ZnFe_2O_4$	citrate	H_2O
	betaine	50 mM HCl
	phosphocholine	H_2O
Fe_3O_4	citrate	H_2O
	betaine	H_2O
	phosphocholine	H_2O

A.3 PDF Analysis of Sample W4

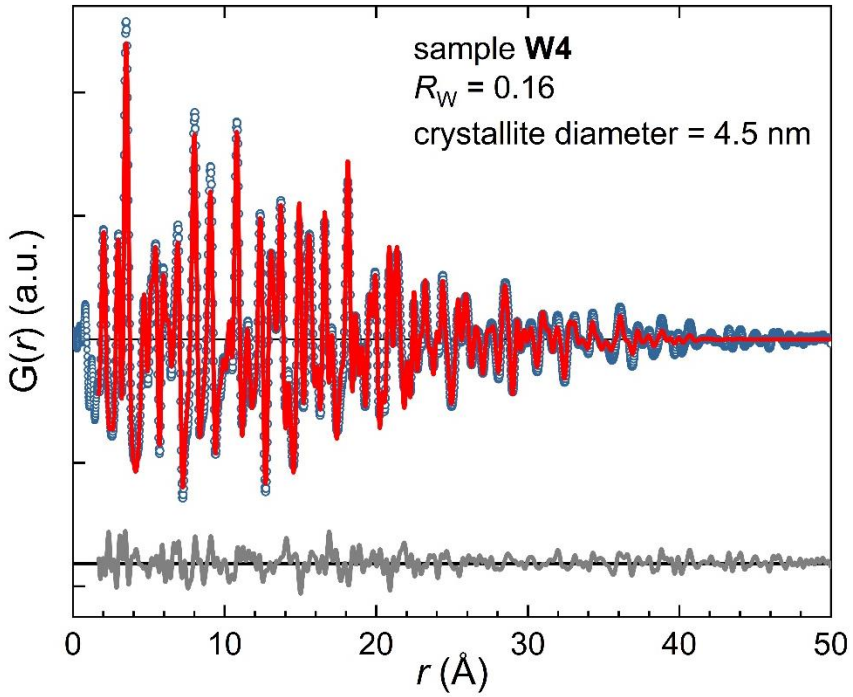

Figure A 1: PDF refinement based on the space group Fd-3m of citrate-stabilized $CoFe_2O_4$ nanoparticles with d_{DLS} = 8.9 nm (sample W4) over a r-range from 0 – 50 Å.
Blue open circles and red solid lines correspond to measured and simulated PDFs, respectively. Grey solid lines are the differences, in offset for clarity. For values of fit parameters Table A 4.

Table A 4: Refined parameters of the PDF analysis of sample W4 based on the space group Fd-3m. *The corresponding refinement is shown in Figure A 1.*

parameter	**W4**
***a* = *b* = *c* (Å) (start)**	8.394
***a* = *b* = *c* (Å)**	8.402
crystallite size (Å)	45
$U_{iso,\ Co/Zn/Ni/Mg}$ **(Å²)**	0.009
$U_{iso,Fe}$ **(Å²)**	0.008
$U_{iso,O}$ **/ (Å²)**	0.020
z(O)	- 0.630
Occ_{oct}	0.98
R_w	0.16

A.4 TEM Analysis of Spinel Ferrite Nanoparticles

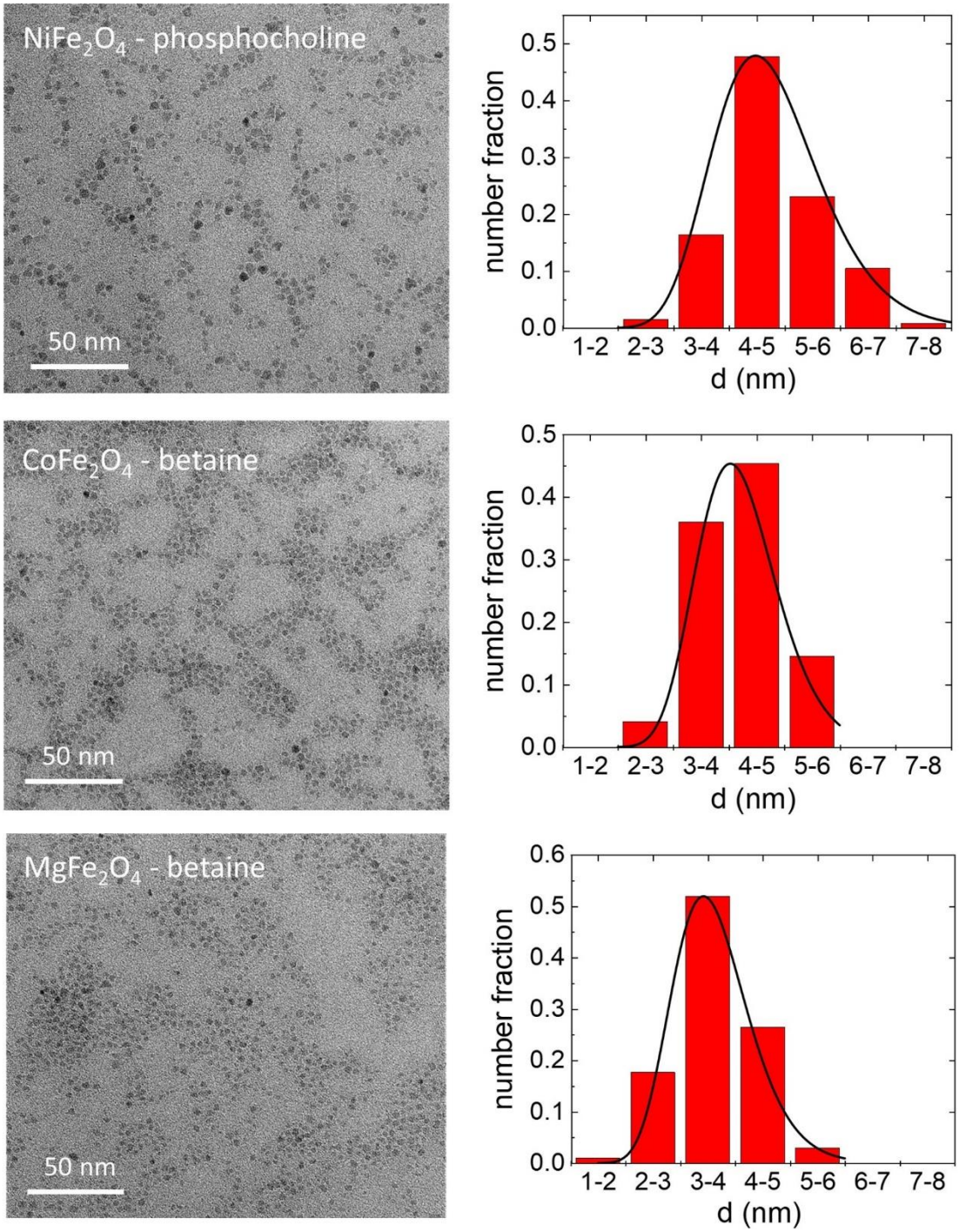

Figure A 2: Representative TEM images of nickel, cobalt and magnesium ferrite nanoparticles stabilized by different organic molecules and the diameter histogram with a lognormal fit of the size distribution of at least 100 particles on the right.

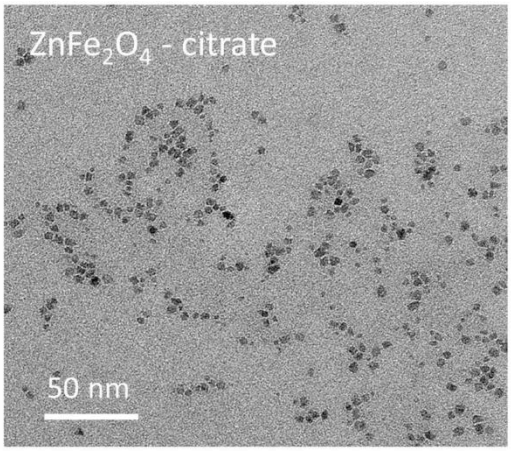

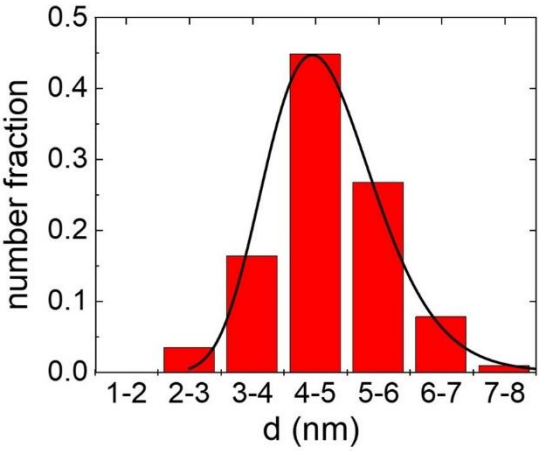

Figure A 3: Representative TEM image of zinc ferrite nanoparticles stabilized with citrate and the diameter histogram with a lognormal fit of the size distribution of at least 100 particles on the right.

Calculation of the size distribution and the PDI from SAXS data:[94]

Table A 5: Equations and variables for the calculation of the size distributions according to SASview 4.2.2.

Distribution Model	Equation		PDI	
Gaussian	$f(x) = \frac{1}{Norm}\exp\left(-\frac{(x-x_{mean})^2}{2\sigma^2}\right)$ with: $Norm = normalization\ factor,$ $\sigma = standard\ deviation,$ $x_{mean} = mean\ of\ distribution.$	***Eq. A1***	$PDI = \frac{\sigma}{x_{mean}}$	***Eq. A2***
Lognorm	$f(x) = \frac{1}{Norm}\frac{1}{xp}\exp\left(-\frac{(ln(x)-\mu)^2}{2p^2}\right)$ with: $Norm = normalization\ factor,$ $\sigma = standard\ deviation,$ $\mu = \ln(x_{med})$ $x_{med} = median\ of\ distribution.$	***Eq. A3***	$PDI = p = \frac{\sigma}{x_{mean}}$	***Eq. A4***

Calculation of the goodness-of-fit factor χ_R^2 of fits of SAXS data:[94]

$$\chi_R^2 = \sum \left[\frac{(Y_i - theory_i)^2}{weight_i^2} \right] / \left[N_{pts} - N_{par} \right] \qquad \textit{Eq. A5}$$

with:

$\chi_R^2 = goodness - of - fit\ factor$,

$Y_i = observed\ data$,

$theory_i = expected\ data$,

$weight_i = supplied\ error\ in\ I$,

$N_{pts} = number\ of\ data\ points$,

$N_{par} = number\ of\ fitted\ parameters$.

Table A 6: χ^2 values for SAXS fits of spherical spinel ferrite nanoparticles.

sample	stabilizer	χ^2
$CoFe_2O_4$	citrate	1.0
	betaine	94.7
	phos	14.0
$ZnFe_2O_4$	citrate	1.4
	betaine	33.9
	phos	51.3
$MgFe_2O_4$	citrate	5.0
	betaine	16.0
	phos	1.7
$NiFe_2O_4$	citrate	1.3
	betaine	20.5
	phos	3.7

A.5 Synthesis of Anisotropic Spinel Ferrite Nanoparticles

Table A 7: χ^2 values for SAXS fits of $CoFe_2O_4$ nanorods.

sample	stabilizer	χ^2
r2	citrate	9.6
r3	phos	6.1

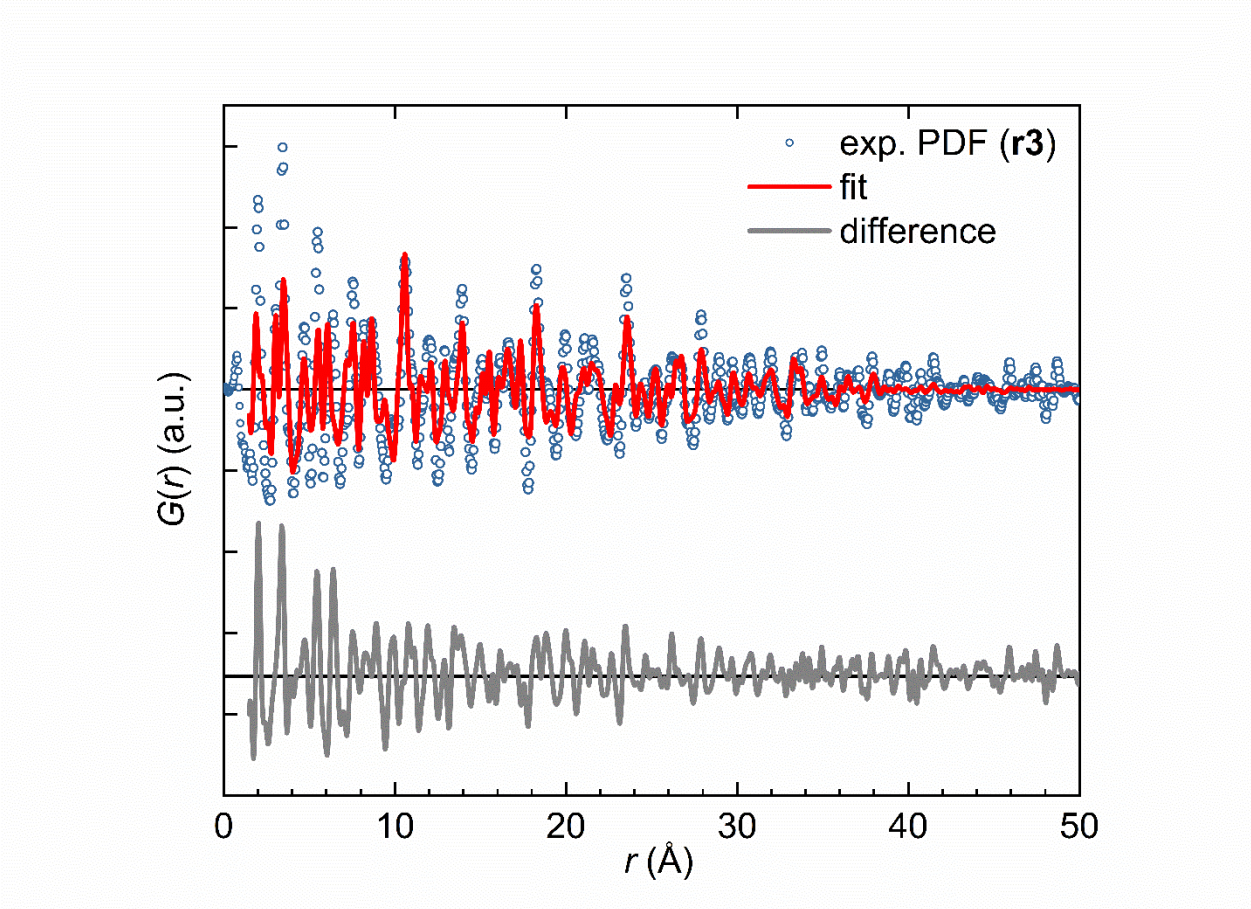

Figure A 4: PDF refinement of the phosphocholine stabilized nanorods (r3) in the r-range from 1.5 to 50 Å. *Blue open circles and the red solid line correspond to measured and simulated PDFs. The grey solid line is the difference.*

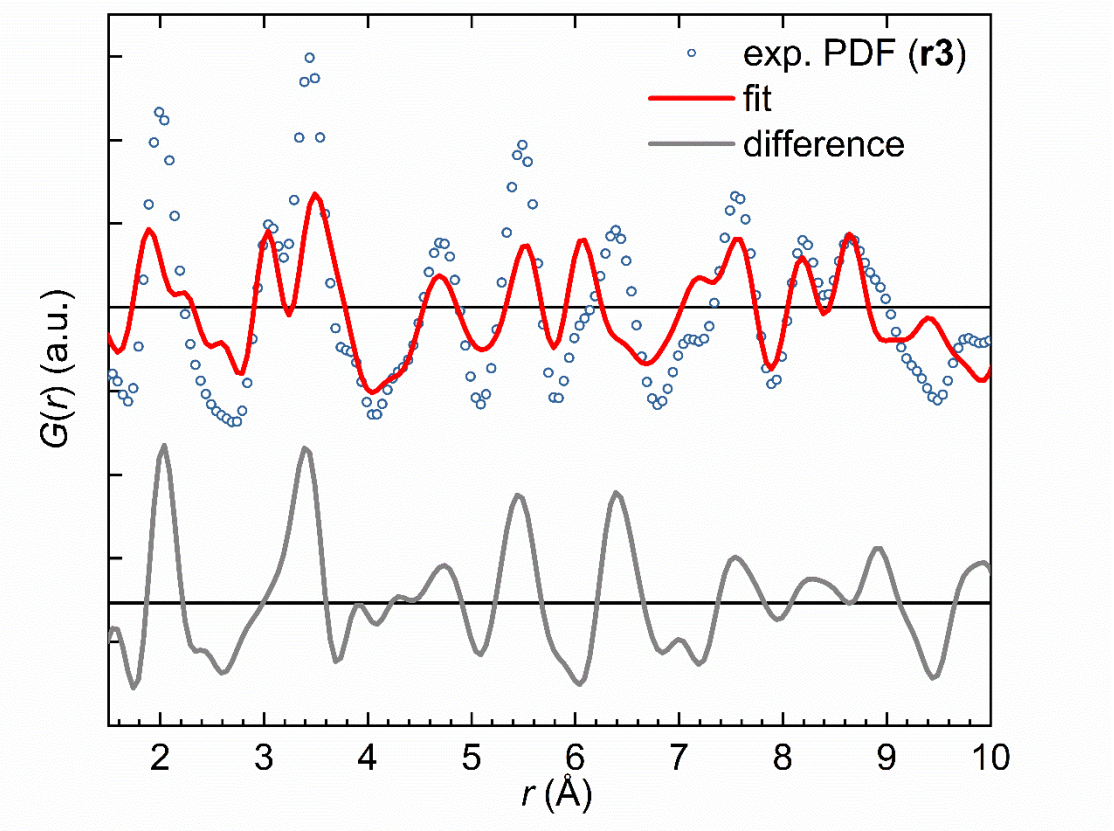

Figure A 5: Zoom into the PDF refinement of the phosphocholine stabilized nanorods (r3) in the r-range from 1.5 to 10 Å. *Blue open circles and the red solid line correspond to measured and simulated PDFs. The grey solid line is the difference.*

Table A 8: Refined parameters for the single phase PDF refinement of phosphocholine stabilized nanorods (sample r3; see Figure A 4).

parameter	
***a* = *b* (Å) (start)**	10.44
***a* = *b* (Å)**	10.511
***c* (Å) (start)**	3.01
***c* (Å)**	3.032
crystallite size (Å)	53
$U_{iso\ xy,\ Fe}$ **(Å²)**	0.016
$U_{iso\ z,\ Fe}$ **(Å²)**	0.001
$U_{iso\ xy,\ O1}$ **(Å²)**	0.013
$U_{iso\ z,\ O1}$ **(Å²)**	0.036
$U_{iso\ xy,\ O2}$ **(Å²)**	0.035
$U_{iso\ z,\ O2}$ **(Å²)**	0.004
$U_{iso\ xy,\ H}$ **(Å²)**	0.004
$U_{iso\ z,\ H}$ **(Å²)**	0.065
R_w	0.62

Table A 9: Refined parameters for the two phase PDF refinement of phosphocholine stabilized nanorods (sample r3; see Figure 20).

parameter	β-FeO(OH)	$CoFe_2O_4$
***a* = *b* (Å) (start)**	10.44	8.394
***a* = *b* (Å)**	10.533	8.172
***c* (Å) (start)**	3.01	8.394
***c* (Å)**	3.034	8.172
crystallite size (Å)	64	5
$U_{iso\ xy,\ Fe/Co}$ **(Å²)**	0.013	0.005
$U_{iso\ z,\ Fe/Co}$ **(Å²)**	0.001	0.005
$U_{iso\ xy,\ Fe2/Co2}$ **(Å²)**		0.003
$U_{iso\ z,\ Fe2/Co2}$ **(Å²)**		0.003
$U_{iso\ xy,\ O1}$ **(Å²)**	0.189	0.003
$U_{iso\ z,\ O1}$ **(Å²)**	0.014	0.003
$U_{iso\ xy,\ O2}$ **(Å²)**	0.044	
$U_{iso\ z,\ O2}$ **(Å²)**	0.001	
$U_{iso\ xy,\ H}$ **(Å²)**	0.004	
$U_{iso\ z,\ H}$ **(Å²)**	0.065	
R_w	0.52	

A.6 Structure Analysis of Spinel Ferrite Nanoparticles

Table A 10: Full-width-at-half-maximum (FWHM) obtained from XRD pattern shown in Figure 22. *A Gauss distribution was fitted to the 440 peak at 4.2 $Å^{-1}$ for the calculation.*

sample	stabilizer	$FWHM^{440}$ ($Å^{-1}$)
$CoFe_2O_4$	citrate	0.153
	betaine	0.149
	phos	0.150
$ZnFe_2O_4$	citrate	0.123
	betaine	0.136
	phos	0.131
$MgFe_2O_4$	citrate	0.200
	betaine	0.178
	phos	0.177
$NiFe_2O_4$	citrate	0.151
	betaine	0.137
	phos	0.124

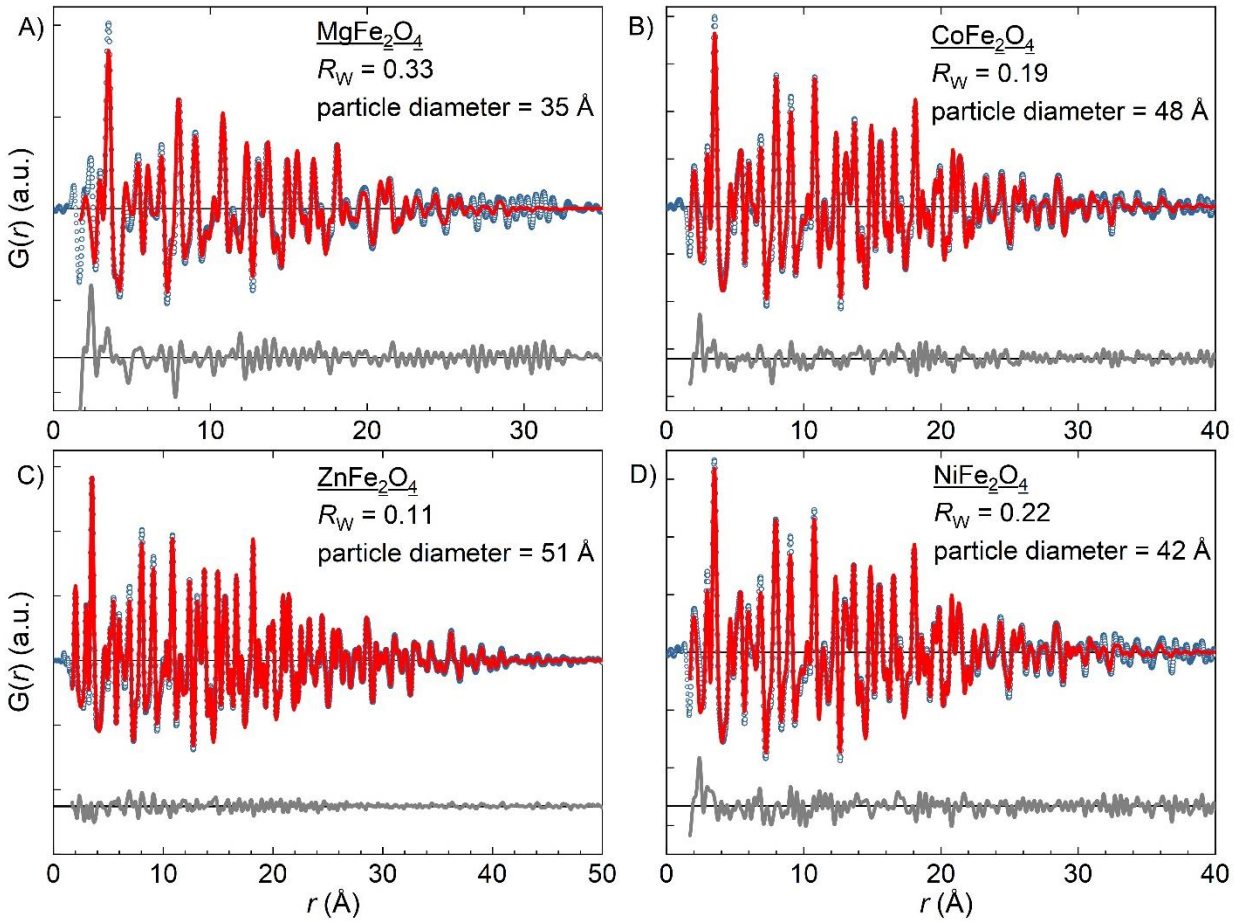

Figure A 6: PDF refinements of citrate-stabilized A) magnesium, B) cobalt, C) zinc and D) nickel ferrite nanoparticles over r-ranges of 1.7 to 35 - 50 Å.

Blue open circles and red solid lines correspond to measured and simulated PDFs. Grey solid lines are the differences, in offset for clarity. All but the magnesium ferrite refinements show good agreement with the experimental data (low R_w-values, no remaining structural signal in difference curve). In the magnesium ferrite nanoparticle refinement, the structural residue can be ascribed to the citrate side phase. For values of fit parameters see Table A 11.

Table A 11: Refined parameters for PDF refinements of citrate-stabilized spinel ferrites including the parameter of octahedral occupancy Occ_{oct} (see Figure A 6).

parameter	$CoFe_2O_4$	$ZnFe_2O_4$	$NiFe_2O_4$	$MgFe_2O_4$
***a* = *b* = *c* (Å) (start)**	8.394	8.442	8.347	8.397
***a* = *b* = *c* (Å)**	8.407	8.425	8.374	8.392
crystallite size (Å)	43	51	42	35
$U_{iso,\ Co/Zn/Ni/Mg}$ **(Å²)**	0.009	0.007	0.011	0.015
$U_{iso,Fe}$ **(Å²)**	0.008	0.008	0.006	0.006
$U_{iso,O}$ **(Å²)**	0.022	0.023	0.019	0.032
z(O)	- 0.630	- 0.633	- 0.629	- 0.619
Occ_{oct}	0.98	0.89	1.00	0.78
R_w	0.19	0.11	0.22	0.33

Table A 12: Refined parameters for PDF refinements of phosphocholine-stabilized spinel ferrites including the parameter of octahedral occupancy Occ_{oct} (see Figure A 7).

parameter	$CoFe_2O_4$	$ZnFe_2O_4$	$NiFe_2O_4$	$MgFe_2O_4$
***a* = *b* = *c* (Å) (start)**	8.394	8.442	8.347	8.397
***a* = *b* = *c* (Å)**	8.389	8.420	8.368	8.384
crystallite size (Å)	41	55	45	36
$U_{iso,\ Co/Zn/Ni/Mg}$ **(Å²)**	0.007	0.007	0.007	0.008
$U_{iso,Fe}$ **(Å²)**	0.008	0.008	0.008	0.010
$U_{iso,O}$ **(Å²)**	0.019	0.023	0.016	0.033
z(O)	- 0.631	- 0.633	- 0.630	- 0.631
Occ_{oct}	0.98	0.87	1.00	0.74
R_w	0.12	0.11	0.13	0.21

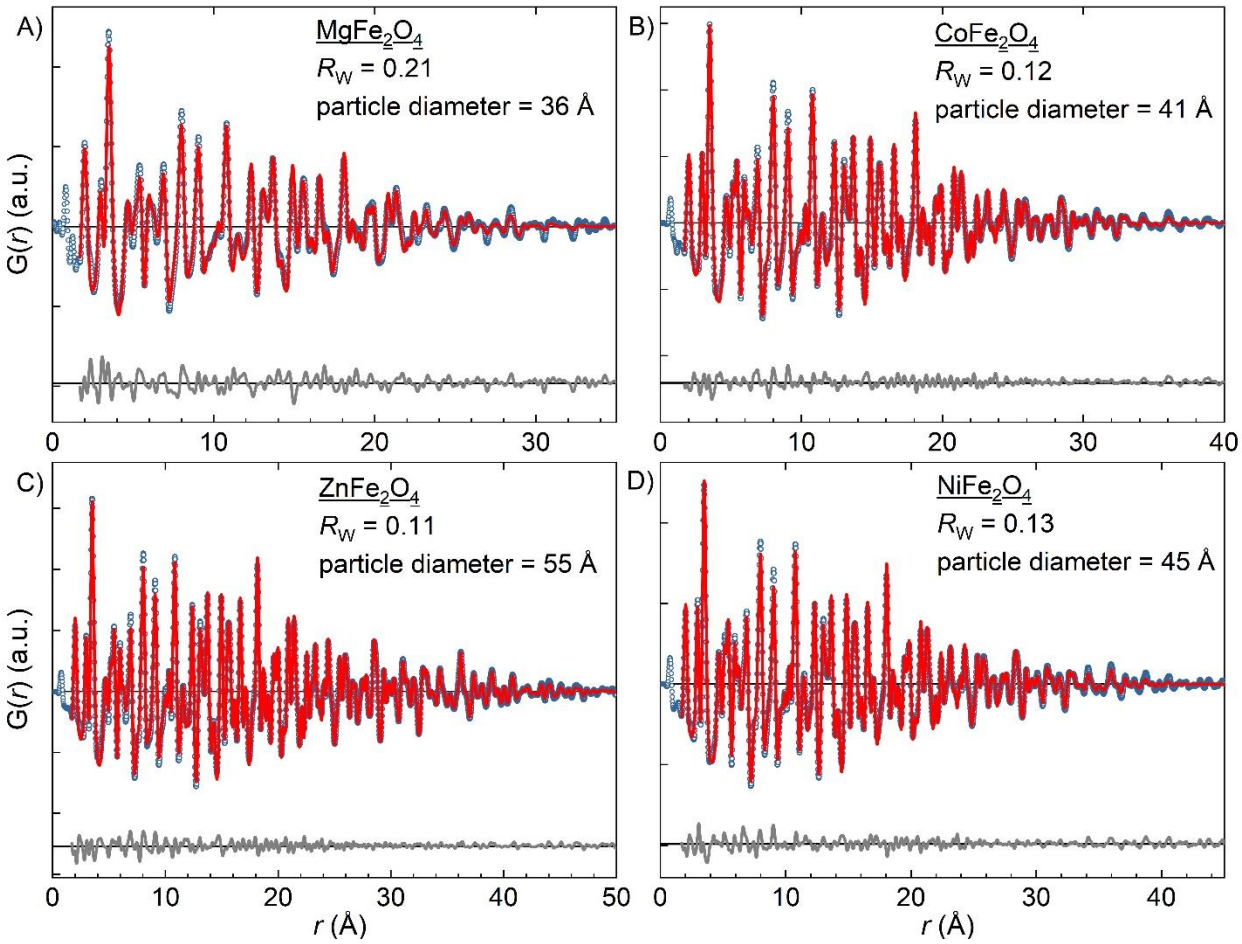

Figure A 7: PDF refinements of phosphocholine-stabilized A) magnesium, B) cobalt, C) zinc and D) nickel ferrite nanoparticles over r-ranges of 1.7 to 35 - 50 Å.

Blue open circles and red solid lines correspond to measured and simulated PDFs. Grey solid lines are the differences, in offset for clarity. All but the magnesium ferrite refinements show good agreement with the experimental data (low R_w-values, no remaining structural signal in difference curve). In the magnesium ferrite nanoparticle refinement, the structural residue can be ascribed to the citrate side phase. For values of fit parameters see Table A 12.

A.7 PDF Refinement of IONP

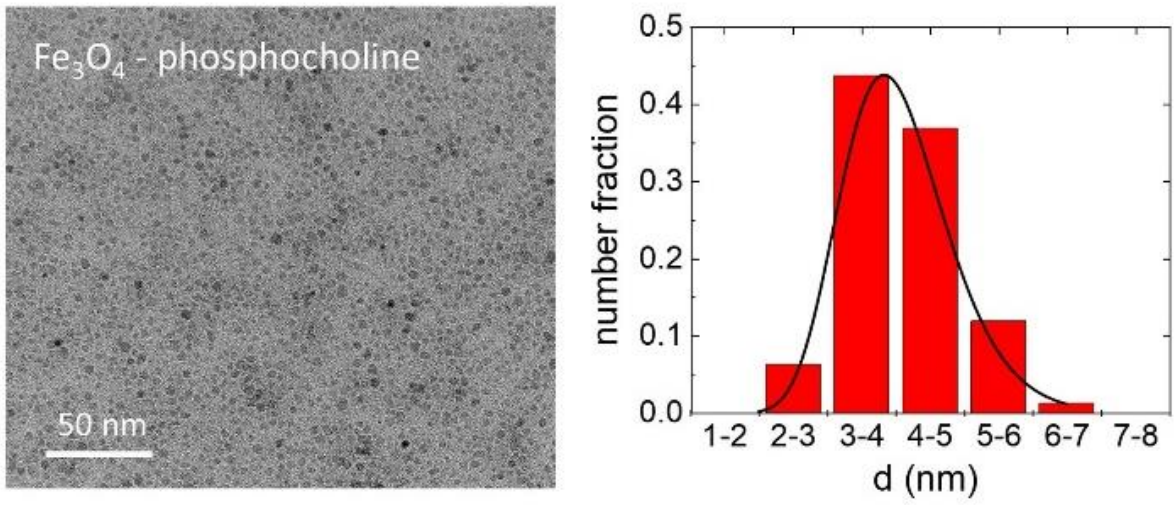

Figure A 9: Representative TEM image of phosphocholine-stabilized IONP nanoparticles and the histogram and the lognormal fit of the size distribution of at least 100 particles to the right.

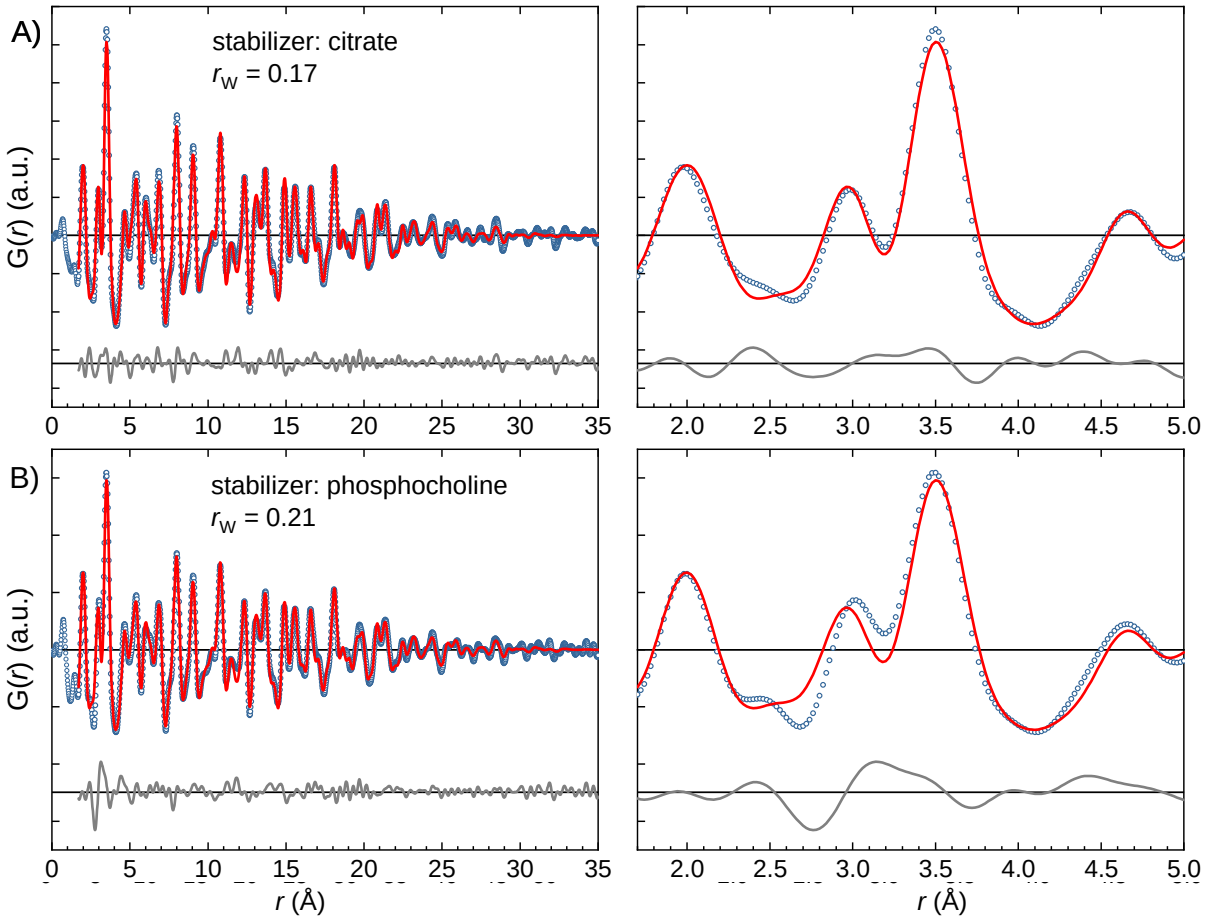

Figure A 8: PDF refinements based on the space group Fd-3m of A) citrate and B) phosphocholine-stabilized IONP over a r-range from 0 – 35 Å. The corresponding r-range from 1.7 – 5.0 Å is magnified on the right.
Blue open circles and red solid lines correspond to measured and simulated PDFs. Grey solid lines are the differences, in offset for clarity. For values of fit parameters see Table A 13.

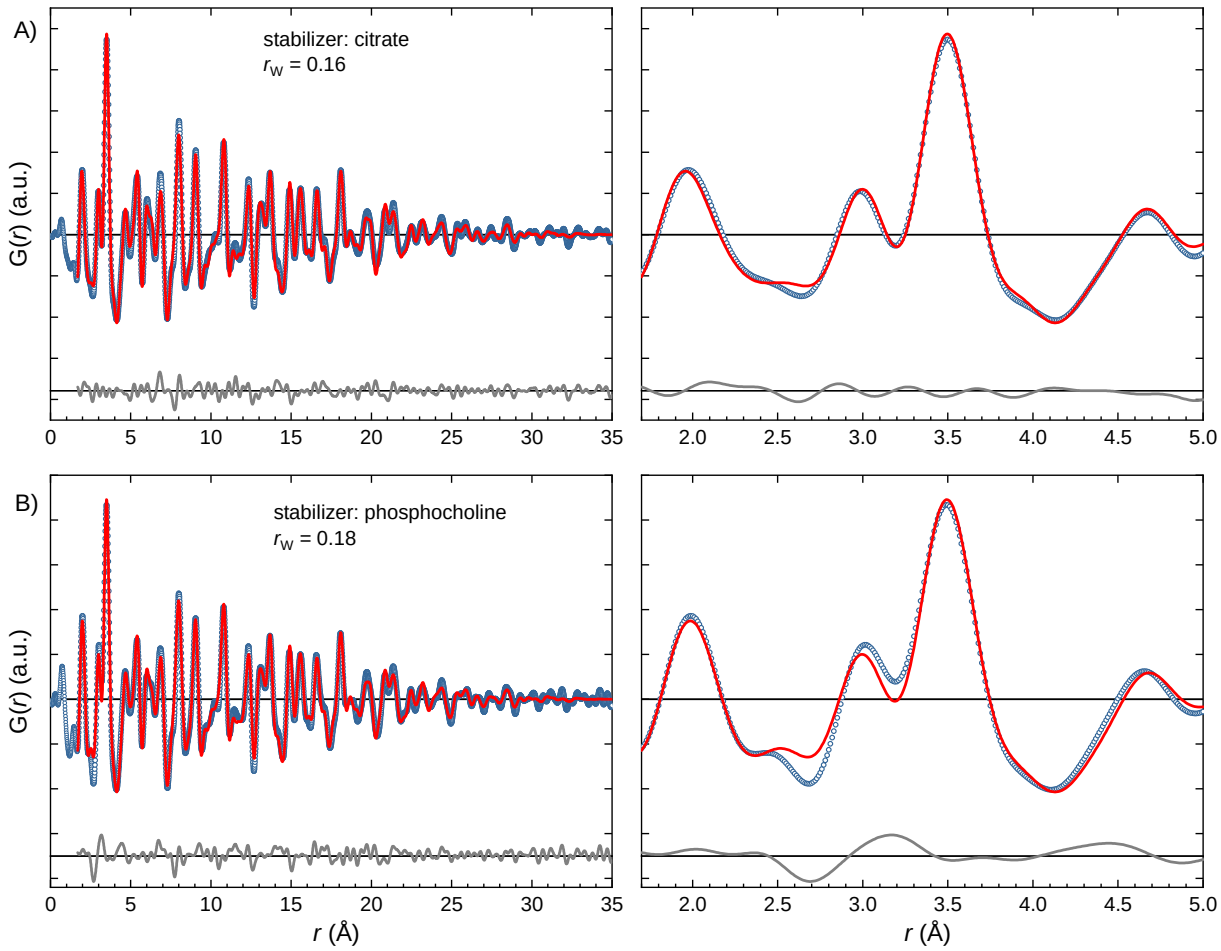

Figure A 10: PDF refinements based on the space group $P4_32_12$ of A) citrate and B) phosphocholine-stabilized IONP over a r-range from 0 – 35 Å. The corresponding r-range from 1.7 – 5.0 Å is magnified on the right.
Blue open circles and red solid lines correspond to measured and simulated PDFs. Grey solid lines are the differences, in offset for clarity. For values of fit parameters see Table A 13.

Calculation of δ for the *Fd-3m* crystal structure*:* $\delta = 2 - 2Occ_{Oct}$ ***Eq. A6***

Calculation of δ for the $P4_32_12$ crystal structure*:* $\delta = 0.5 - 0.5B_{Fe(4)}$ ***Eq. A7***

Calculation of the magnetite phase ratio (mpr) from δ: $mpr = 1 - 3\delta$ ***Eq. A8***

Table A 13: Comparison of the refined parameters of citrate and phosphocholine-stabilized IONP based on a cubic (Fd-3m) and a tetragonal ($P4_32_12$) symmetry.

Sample	**Fe_3O_4 - citrate**	**Fe_3O_4 - citrate**	**Fe_3O_4 - phos**	**Fe_3O_4 - phos**
Space group	*Fd-3m*	*$P4_32_12$*	*Fd-3m*	*$P4_32_12$*
***a=b* (Å) (start)**	8.397	8.337	8.397	8.337
***c* (Å) (start)**	8.397	8.322	8.397	8.322
***a=b* (Å)**	8.394	8.417	8.391	8.404
***c* (Å)**	8.394	8.333	8.391	8.348
crystallite size (Å)	35	36	35	36
$U_{iso,Fe}$ (Å²)	0.011	0.007	0.013	0.008
$U_{iso,O}$ (Å²)	0.026	0.007	0.027	0.011
O_z	- 0.630		-0.630	
O1_x		0.602		0.618
O1_y		0.866		0.873
O1_z		- 0.003		- 0.021
O2_x		0.134		0.144
O2_y		0.379		0.381
O2_z		- 0.002		0.002
O3_x		0.131		0.135
O3_y		0.875		0.883
O3_z		0.014		0.026
O4_x		0.418		0.384
O4_y		0.624		0.629
O4_z		- 0.031		- 0.010
δ	0.33	0.33	0.33	0.33
magnetite phase ratio	0 %	0 %	0 %	0 %
R_w	0.17	0.16	0.21	0.18

A.8 Total Scattering Analysis of Spinel Ferrite Nanoparticles obtained via different Synthesis Routes

Calculation of the sum formula of the spinel phase in the $MnFe_2O_4$ nanoparticles treated at 400 °C:

Mn/Fe – ratio according to SEM-EDX:		0.52
Refined molar phase contents according to PDF:	Mn_2O_3:	0.312
	spinel:	0.668
Sum formula for a Fe-rich spinel structure:	$Mn_{1-y}Fe_{2+y}O_4$	

➔ $\frac{n(Mn)}{n(Fe)} = 0.52 = \frac{0.312*2+0.688*(1-y)}{0.688*(2+y)}$; ***Eq. A9***

➔ $0.358 * (2 + y) = 0.624 + 0.668 * (1 - y)$;

➔ $0.716 + 0.358 * y = 0.624 + 0.668 * -0.688 * y$;

➔ $y = 0.57$

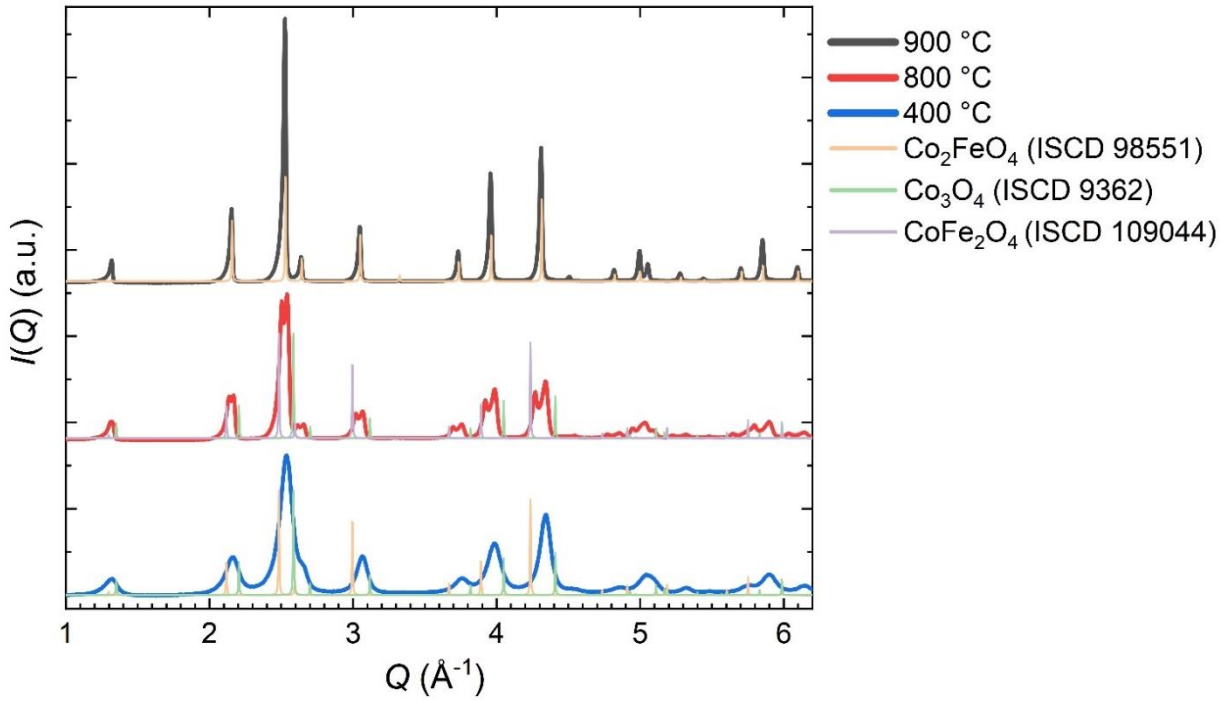

Figure A 11: XRD pattern of Co/Fe LDH calcined at 400 (blue), 800 (red) and 900 °C (black). *The patterns are stacked and scaled for clarity. Calculated reference patterns of Co_2FeO_4 (orange), Co_3O_4 (green) and $CoFe_2O_4$ (purple) are inserted individually at each temperature to highlight existing phases.*

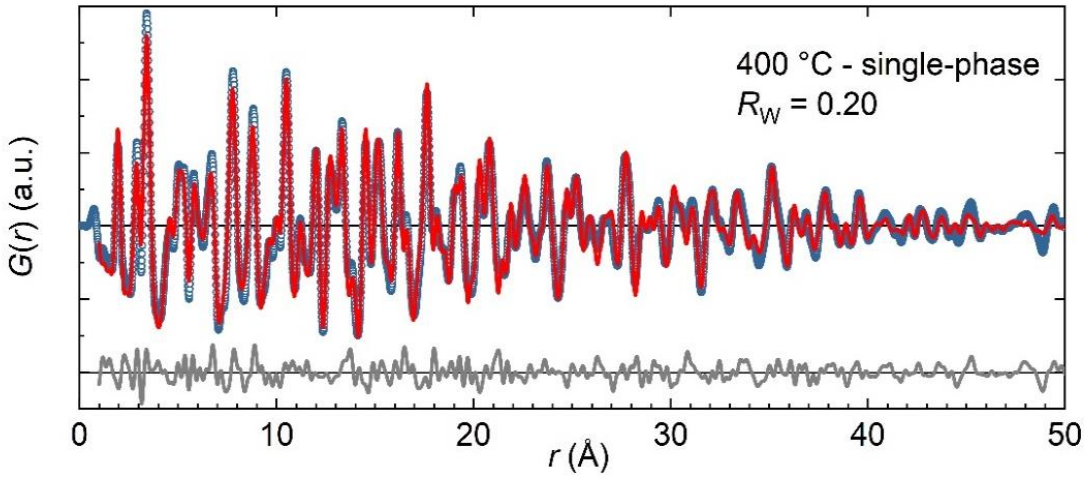

Figure A 12: Single-phase PDF refinements based on Co_2FeO_4 from 1.0 to 50 Å of a Co/Fe sample calcined at 400 °C. *Blue open circles and red solid lines correspond to measured and simulated PDFs, respectively. Grey solid lines directly beneath the experimental data and the fit are the differences. The patterns are stacked for clarity. For the two-phase fit based on Co_3O_4 and $CoFe_2O_4$ see Figure 27, top graph.*

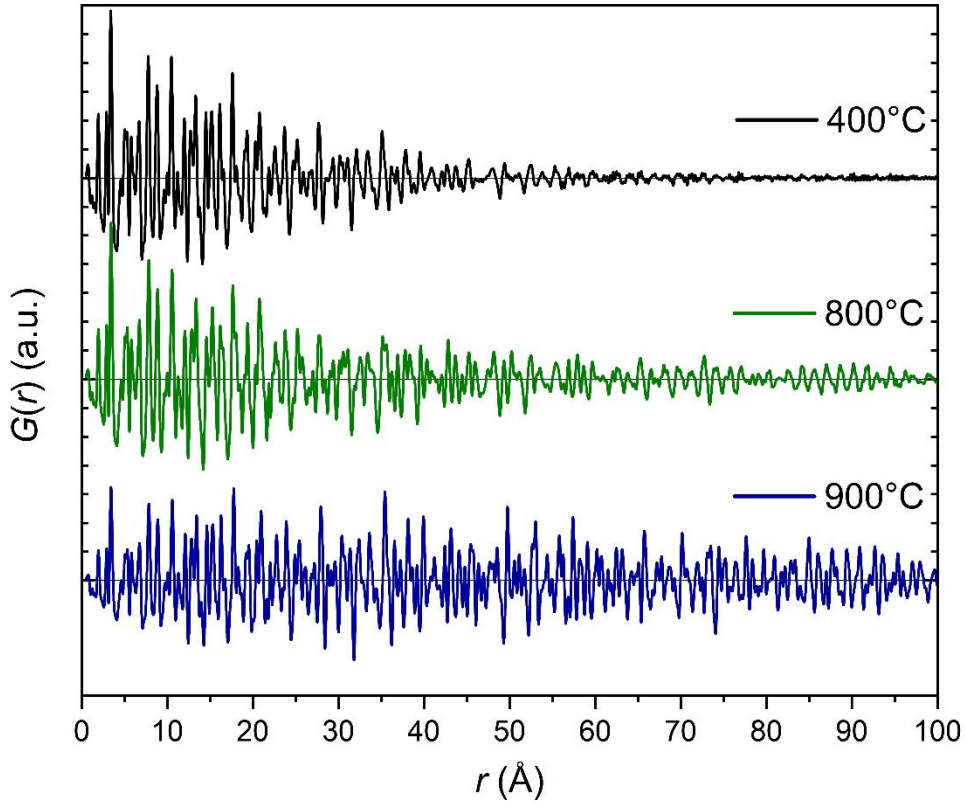

Figure A 13: Experimental PDF data of Co/Fe LDH calcined at 400, 800 and 900 °C until r = 100 Å. *For the corresponding refinements see Figure 29.*

Table A 14: Comparison of the refined parameters of cobalt and iron containing spinel ferrites synthesized from cobalt and iron containing LDH based on a cubic (Fd-3m) model. *For fits see Figure 29 and Figure A 12.*

Sample	**400 °C**	**400 °C**		**800 °C**		**900 °C**
applied phases	Co_2FeO_4	Co_3O_4	$CoFe_2O_4$	Co_3O_4	$CoFe_2O_4$	Co_2FeO_4
ISCD number	98551	9362	109044	9362	109044	98551
a (Å) (start)	8.242	8.065	8.394	8.065	8.394	8.242
a (Å)	8.178	8.156	8.209	8.186	8.318	8.404
crystallite size (Å)	60	69	65	138	127	334
$U_{iso,TL}$ **(Å²)**	0.013	0.010	0.013	0.009	0.014	0.011
$U_{iso,TL2}$ **(Å²)**	-	0.010	-	0.011	-	-
$U_{iso,OL}$ **(Å²)**	0.010	0.007	0.014	0.010	0.027	0.009
$U_{iso,O}$ **(Å²)**	0.026	0.015	0.033	0.027	0.045	0.032
phase ratio	-	41 %	59 %	50 %	50 %	-
R_w	0.20	0.16		0.21		0.18

A.9 Colloidal Stability of Spinel Ferrite Nanoparticles

Table A 15: Particle diameter of spinel ferrite nanoparticles according to DLS after storage as aqueous dispersion at RT (c = 5 g L^{-1}).

nanoparticle composition	stabilizer	particle diameter (nm) (PDI)	ageing time (months)
$CoFe_2O_4$	citrate	5.4 (0.3)	10
		4.8 (0.2)	2
	betaine	5.0 (0.3)	2
		4.9 (0.3)	8.5
$MgFe_2O_4$	citrate	87.1 (0.2)	2
	betaine	4.6 (0.3)	7
	phosphocholine	5.0 (0.3)	7
$NiFe_2O_4$	citrate	5.2 (0.2)	10
		4.5 (0.2)	2
	betaine	5.1 (0.2)	8
	phosphocholine	6.5 (0.2)	8.5
		5.4 (0.2)	2
$ZnFe_2O_4$	citrate	6.0 (0.2)	10
		5.5 (0.2)	2
	betaine	5.4 (0.3)	8
		7.6 (0.3)	2
	phosphocholine	6.3 (0.2)	8.5
		6.4 (0.2)	2

A.10 Surface Coverage of Spinel Ferrite Nanoparticles

Generic calculation of the number (#) of layers of stabilizer molecules per nanoparticle:

$$\frac{\boldsymbol{V(NP) * \rho(NP) * (total\ organic\ content)}}{\boldsymbol{N\left(\frac{molecule}{layer}\right) * m\ (molecule) * (total\ inorganic\ content)}} = \boldsymbol{\#\ layers\ of\ stabilizer\ per\ NP} \qquad \textit{Eq. A10}$$

with:

$\boldsymbol{m(betaine) = 1.9 * 10 - 22\ g}$,

$\boldsymbol{m(citrate) = 3.1 * 10 - 22\ g}$

$\boldsymbol{m(phosphocholine) = 3.1 * 10 - 22\ g}$,

$\boldsymbol{V_{NP} = \frac{4}{3}\pi r^3}$,

$\boldsymbol{total\ organic\ content = ratio\ of\ organics\ or\ TOC}$,

$\boldsymbol{total\ inorganic\ content = ratio\ of\ inorganics\ determined\ by\ TGA}$,

$\boldsymbol{N\left(\frac{molecule}{layer}\right) = S_{NP} * (3.5\ to\ 5.9)\frac{1}{nm^2}}$

with: $\boldsymbol{S_{NP} = 4\pi r^2}$.

Table A 16: Complementary data of the TGA analysis presented in chapter 6.1. *The inorganic mass (m_{NP}^{TGA}) and mass of water at the nanoparticle surface (m_{H2O}^{TGA}) before and after dialysis is shown.*

sample	stabilizer	$m_{NP,as-syn}^{TGA}$ (wt%)	$m_{H2O,as-syn}^{TGA}$ (wt%)	$m_{NP,dia}^{TGA}$ (wt%)	$m_{H2O,dia}^{TGA}$ (wt%)
$CoFe_2O_4$	citrate	69.1	3.2	75.0	4.8
	betaine	69.7	3.4	-	-
	phos	59.9	6.0	79.2	3.7
$ZnFe_2O_4$	citrate	66.8	2.0	75.2	2.8
	betaine	81.3	1.4	-	-
	phos	50.2	4.8	68.8	3.1
$MgFe_2O_4$	citrate	43.3	6.6	65.0	5.7
	betaine	59.9	6.5	-	-
	phos	47.1	3.9	75.8	7.7
$NiFe_2O_4$	citrate	62.6	3.5	74.5	5.7
	betaine	71.5	2.3	-	-
	phos	48.1	6.6	75.5	3.3

Table A 17: Raw data of CHN analysis. *The amount of each specific atom is given in wt% in relation to the total mass of the initial sample.*

sample	stabilizer	sample mass (mg)	content of N (wt%)	content of C (wt%)	content of H (wt%)
$CoFe_2O_4$	betaine	3.63	0.11	6.46	1.47
	phos	2.07	0.46	5.77	1.74
$ZnFe_2O_4$	phos	1.90	0.97	6.04	2.08
$MgFe_2O_4$	phos	2.07	0.47	5.57	2.41
$NiFe_2O_4$	betaine	1.79	0.21	6.78	1.45
	phos	2.17	1.07	6.60	2.28

Publikationen

Teile dieser Arbeit wurden veröffentlicht in:

- M. Eckardt, S. L. J. Thomä, M. Dulle, G. Hörner, B. Weber, S. Förster, M. Zobel, *ChemistryOpen* **2020**, *9*, 1214-1220.
- C. Simon, A. Blösser, M. Eckardt, H. Kurz, B. Weber, M. Zobel, R. Marschall, *Z. Anorg. Allg. Chem.* **2021**, *647*, 2061-2072.

Weitere Publikationen:

- S. Thomä, S. W. Krauß, M. Eckardt, P. Chater, M. Zobel, *Nat. Commun.* **2019**, *10*, 995. (retracted: DOI 10.1038/s41467-024-50636-y)
- R. Schlem, A. Banik, M. Eckardt, M. Zobel, W. Zeier, *Appl. Energy Mater.* **2020**, *3*, 10164.
- S. W. Krauss, M. Eckardt, J. Will, E. Spieker, R. Siegel, M. Dulle, R. Schweins, B. Pauw, J. Senker, M. Zobel, *Nanoscale* **2023**, *15,* 16413*.*

Danksagung

An dieser Stelle möchte ich mich bei all meinen Wegbegleiterinnen und Wegbegleitern bedanken.

Als erstes gilt mein Dank natürlich meiner Doktormutter Prof. Dr. Mirijam Zobel. Ich möchte mich für die Möglichkeit bedanken, die Promotion in ihrer damals noch sehr jungen Arbeitsgruppe durchzuführen. Sie gab mir wertvolle Unterstützung, war für Fragen stets erreichbar und gab mir die Möglichkeit mich auch abseits der fachlichen Kompetenzen zu entwickeln.

Selbstverständlich bedanke ich mich auch bei allen Kooperationspartner, die an Publikationen in dieser Arbeit mitgewirkt haben und dementsprechend auch einen maßgeblichen Anteil zu dieser Arbeit geleistet haben. Auch bei allen studentischen Mitarbeiter*innen, insbesondere Fr. Denise Schweser, möchte ich für ihre Unterstützung danken.

Auch bei den Kollegen aus der Anorganischen Chemie 1 möchte ich mich für die tatkräftige Unterstützung danken. Sei es durch Messungen, Organisation, Ideen oder einfach guten Unterhaltungen, ihr habt mir die Durchführung sehr erleichtert.

Ein besonderer Dank gilt an dieser Stelle meinen beiden Arbeitsgruppenkolleg*innen Sabrina und Nils. Besonders Nils hat sich durch unzählige fachliche, philosophische, football- oder brettspiellastige Diskussionen seine Erwähnung an dieser Stelle verdient.

Auch bei Sonja und Christoph, meinen beiden treuen Begleitern während und auch abseits des Studiums, möchte ich mich für die stets brillante Zusammenarbeit bedanken.

Der größte Dank geht jedoch an meine Familie, die mir mein Studium sowie die anschließende Promotion ermöglichten, und meiner Frau Theresa, die bei allen Höhen und Tiefen immer hinter mir stand, mich stets unterstütze und immer an mich glaubte, sowie meinem Sohn Otto, aus dessen bloßer Anwesenheit ich Antriebskraft ziehen kann. Vielen Dank!

Selbstständigkeitserklärung

Hiermit versichere ich, Mirco Eckardt, eidesstattlich, dass ich die vorliegende Arbeit selbstständig verfasst und keine anderen als die von mir angegebenen Quellen und Hilfsmittel benutzt habe.

Hiermit erkläre ich, dass ich die Dissertation nicht bereits zur Erlangung eines akademischen Grades eingereicht habe und dass ich nicht bereits diese oder eine gleichartige Doktorprüfung endgültig nicht bestanden habe.

Hiermit erkläre ich, dass ich die Hilfe gewerblichen Promotionsberatern bzw. –vermittlern oder ähnlichen Dienstleistern weder bisher in Anspruch genommen habe noch künftig in Anspruch nehmen werde.

Hiermit erkläre ich mein Einverständnis, dass die elektronische Fassung meiner Dissertation unter Wahrung meiner Urheberrechte und des Datenschutzes einer gesonderten Überprüfung unterzogen werden kann.

Hiermit erkläre ich mein Einverständnis, dass bei Verdacht wissenschaftlichen Fehlverhaltens Ermittlungen durch universitätsinterne Organe der wissenschaftlichen Selbstkontrolle stattfinden können.

Bayreuth, den _____ _____

Ort, Datum Unterschrift